

## **General Disclaimer**

### **One or more of the Following Statements may affect this Document**

- This document has been reproduced from the best copy furnished by the organizational source. It is being released in the interest of making available as much information as possible.
- This document may contain data, which exceeds the sheet parameters. It was furnished in this condition by the organizational source and is the best copy available.
- This document may contain tone-on-tone or color graphs, charts and/or pictures, which have been reproduced in black and white.
- This document is paginated as submitted by the original source.
- Portions of this document are not fully legible due to the historical nature of some of the material. However, it is the best reproduction available from the original submission.



# DEPARTMENT OF MECHANICAL ENGINEERING

FINAL TECHNICAL REPORT

THE INFLUENCE OF GYROSCOPIC FORCES ON  
THE DYNAMIC BEHAVIOR AND FLUTTER OF  
ROTATING BLADES

By

F. Sisto and A.T. Chang

December 1983

Prepared for

Lewis Research Center

National Aeronautics &  
Space Administration

Cleveland, Ohio 44315

NASA Grant NAG3-47

Report No. ME-RT-82006



STEVENS INSTITUTE  
OF TECHNOLOGY

CASTLE POINT STATION  
HOBOKEN, NEW JERSEY 07030

(NASA-CR-175444) THE INFLUENCE OF  
GYROSCOPIC FORCES ON THE DYNAMIC BEHAVIOR  
AND FLUTTER OF ROTATING BLADES Final  
Technical Report, 1 Jun. 1980 - 31 Aug. 1983  
(Stevens Inst. of Tech.) 118 p

N84-20524

Unclas  
G3/07 18869

FINAL TECHNICAL REPORT

under

NASA Grant NAG3-47

THE INFLUENCE OF GYROSCOPIC FORCES ON THE  
DYNAMIC BEHAVIOR AND FLUTTER OF ROTATING BLADES

F. Sisto and A.T. Chang

Department of Mechanical Engineering  
Stevens Institute of Technology  
Hoboken, N.J. 07030

December 1983

Prepared for  
Lewis Research Center  
National Aeronautics and Space Administration  
Cleveland, Ohio 44315

Period of the Report: 1 June 1980 to 31 August 1983

Approved for Public Release; Distribution Unlimited

## TABLE OF CONTENTS

CHAPTER	PAGE
1. Summary	1
2. Introduction	2
3. Blade Idealized as a Cantilever Beam Under Rotor Spin and Space Fixed Precession	4
3.1 Introduction	4
3.2 Kinetic and Potential Energies	4
3.3 Uniform Blades	9
3.4 Blades with Different Geometry	36
3.5 Time-Varying Precession	40
3.6 The Effect of Damping	44
4. Arbitrary Blades Under Combined Rotor Spin and Spaced-Fixed Precession	57
4.1 Introduction	57
4.2 Stiffness Matrix	58
4.3 Kinetic Energy and Mass Matrix	72
4.4 Stability Analysis	80
5. Forced Vibration and Flutter	83
5.1 Introduction	83
5.2 Forced Vibration	84
5.3 Flutter	85
6. Conclusions	91
7. Acknowledgement	93
8. References	94
Appendix A	A-1
B	B-1
C	C-1
D	D-1
E	E-1

## 1. Summary

This report summarizes the results of a three year investigation into the structural dynamics of a cantilever turbomachine blade mounted on a spinning and precessing rotor.

A cumulated list of publications issued during the course of the research appear as references 1,2,3 and 5 of this final technical report. In addition to these references which are conference proceedings and journal publications, reference 17 is an interim report covering the first eighteen months of research under the Grant. The present final technical report incorporates that interim report, with corrections, and augments it with the results of the final one and one half year of effort.

Both stability and forced vibration are considered with a blade model that increases in complexity (and verisimilitude) from a spring-restrained point mass, to a uniform cantilever, to a twisted uniform cantilever, to a tapered twisted cantilever of arbitrary cross-section. In every instance the formulation is from first principles using a finite element based on beam theory. Both ramp-type and periodic-type precessional angular displacements are considered. In concluding, forced vibrating and flutter are studied using the final and most sophisticated structural model.

The analysis of stability is presented in some detail and a number of numerical examples are worked out. One example is given approximating a shroud-type restraint at the 3/4 span point. One other set of calculations demonstrate the role of structural

damping in the phenomenon. The practical occurrence of this type of instability is discussed.

The forced vibration problem is treated, with forcing present at one and two times the rotational frequency with amplitude dependent upon the precessional rate. Finally there are presented some considerations on the effect of subsonic aerodynamic damping on the dynamics of twisted cantilever blades. The conclusion is that when flutter occurs it is of the coalescent type with the two lowest modes coupling to account for the vanishing of the aerodynamic damping.

## 2. Introduction to Precession-Induced Instability of Rotor Blades

An operating turbine-type aeroengine may be considered a gyroscope with the turbomachine rotor blades representing a large number of radially disposed beams. These blades are subject to a wide variety of vibratory forcing mechanisms as well as flutter, or self-excitation. Hence rotor blade vibrations, as well as those of stator vanes, have received a great deal of analytical and experimental attention, forming a very large sub-discipline in the field of aeroelastic and mechanical vibrations. The excitation and self-excitation studied in this present research program relate to the fact that the engine spin axis may be forcibly precessed with angular rates that are developed by the entire vehicle in which the aeroengine is mounted.

The potential sources of precession of the rotor shaft axis are several in number. In highly maneuverable aircraft the pilot may intentionally institute rapid pull-up, nose-over or yawing motions with angular rates approaching, or even exceeding one radian per second. With a maneuver lasting only a few seconds the rotor may turn through hundreds of revolutions providing ample time for self-excitation to occur or for forced vibrations to build up.

In addition to this ramp-type precession, the rotor may be subjected to an harmonic precession of the engine axis due to flying through a turbulent atmosphere. A wing-mounted engine would be subjected to the same harmonic angular rate as the wing chord in a flutter situation, assuming the flutter mode had an appreciable wing torsion component. In the latter case, however, the fluttering system would consist of the wing/pylon/engine and the inertial and aeroelastic characteristics of the engine and its nacelle would have to be included in the flutter stability determination.

Another potential source of harmonic precession is the operation of turbine engined aircraft on rough runways, or the operation of land vehicles in rough terrain. In these cases, as well as in the turbulent atmosphere, the precession might be expected to have a certain statistical distribution centered about the natural frequency of the entire complex vibrating structure.

Other vehicular applications of gas turbines and the seismic motion of stationary gas turbine mounts are additional situations in which gyroscopic influences on blade stability may be important.

For the ultimate treatment of these gyroscopic phenomena in turboblading the aerodynamic influences should be included in the analysis. However, initially it is convenient to ignore the aerodynamic forces and deal with only elasticity and inertia. If the assumed operation is far from a flutter condition this assumption is tantamount to ignoring the aerodynamic damping provided by the working fluid (air, or combustion products in a turbine).

The order of investigation is therefore as follows:

- i) Develop a finite element for a tapered, twisted beam
- ii) Qualify the element by static loadings and rotating natural frequency determination
- iii) Conduct stability analyses and forced vibration analyses under both precession histories, steady (or ramp variation) and harmonic
- iv) Include the aerodynamic forces in the forced vibration analysis, and, if possible, in the self-excitation analysis
- v) Include the shaft restraint in the analysis (i.e., allow for a "coning" of the shaft as additional degrees of freedom)

In the present report items i) to iii) are included, representing the results of the first 18 months of work under the present contract. (These results have been reported in 3 published papers 1, 2, 3).



### 3. Blade Idealized as a Cantilever Beam Under Rotor Spin and Space-Fixed Precession

#### 3.1 Introduction

This section deals with the study of vibratory behavior of turbo-machine blades under combined rotor spin and angular precession. The turbine blade is idealized as a cantilever beam. Pretwist is not considered. The effects of blade taper, variable precession rate, damping and Coriolis forces are studied.

The purpose of this study is to gain insight into the complicated problem of blade vibrations under combined rotor spin and precession by first studying a simplified model. The results of this study can also be used as references for the numerical solution obtained from the more complete model employed in Section 4.

The equations of motion are derived from Lagrange's equations. The kinetic and potential energy expressions required are developed in the sequel.

#### 3.2 Kinetic and Potential Energies

It is assumed that the precessional velocity vector is space fixed and the origin of the rotor fixed xyz coordinate system (see Fig. 1) is a fixed inertial point.

The angular velocity of the rotor is

$$\vec{\omega} = \omega i + \Omega (\cos \theta j + \sin \theta k) \quad (1)$$

where  $\theta = -\omega t$  and  $\omega$  is the magnitude of the rotor spin velocity. The position vector of a displaced point on the beam can be given as

$$\vec{r} = (x + \delta_x) i + (y + \delta_y) j + (z + \delta_z) k \quad (2)$$

where  $\delta_x, \delta_y, \delta_z$  are the centroidal displacement components of an arbitrary beam cross section. For the purposes of this section  $\delta_z$  can be considered to include only the fore-shortening effect (4) and is given by

$$\delta_z = -\frac{1}{2} \int_R^z \left[ \left( \frac{\partial \delta_x}{\partial z} \right)^2 + \left( \frac{\partial \delta_y}{\partial z} \right)^2 \right] dz \quad (3)$$

Taking the time derivative of equation (2) the velocity of a point on the beam is

$$\vec{v} = \dot{\delta}_x i + \dot{\delta}_y j + \dot{\delta}_z k + \vec{\omega} \times \vec{r} \quad (4)$$

Using equations (1) and (2) the velocity can be written more explicitly

$$\begin{aligned} \vec{v} = & \left[ \dot{\delta}_x + (z + \delta_z) \omega \cos \theta - (y + \delta_y) \omega \sin \theta \right] i \\ & + \left[ \dot{\delta}_y - (z + \delta_z) \omega \sin \theta + (x + \delta_x) \omega \cos \theta \right] j \\ & + \left[ \dot{\delta}_z + (y + \delta_y) \omega - (x + \delta_x) \omega \cos \theta \right] k \end{aligned} \quad (5)$$

The kinetic energy is obtained from

$$T = \frac{1}{2} \int_V \dot{v} \cdot \dot{v} \rho dV \quad (6)$$

We neglect all the terms which include  $x$  and  $y$  in the above integral because these terms are due to shear deformations and/or due to rotary inertia which are usually neglected in beam type analysis. Equation (6) can be simplified

$$T = \frac{1}{2} \int_R^{R+L} \dot{v} \cdot \dot{v} \rho A(z) dz \quad (7)$$

where  $A(z)$  is the variable cross sectional area. In practice blades usually have a very nearby linear thickness variation

$$A(z) = A \left[ (t_r - 1) \frac{z - R}{L} + 1 \right], \quad z > R \quad (8)$$

where  $A$  is the cross sectional area at the root of the blade, and  $t_r$  is the ratio of tip thickness to that of the base.

In order to reduce the beam problem with many degrees of freedom to a single degree of freedom, only bending vibration perpendicular to the major axis of cross section is considered. This leads to

$$\begin{aligned} \delta_y &= \bar{\delta}(z, t) \cos \beta \\ \delta_x &= -\bar{\delta}(z, t) \sin \beta \end{aligned} \quad (9)$$

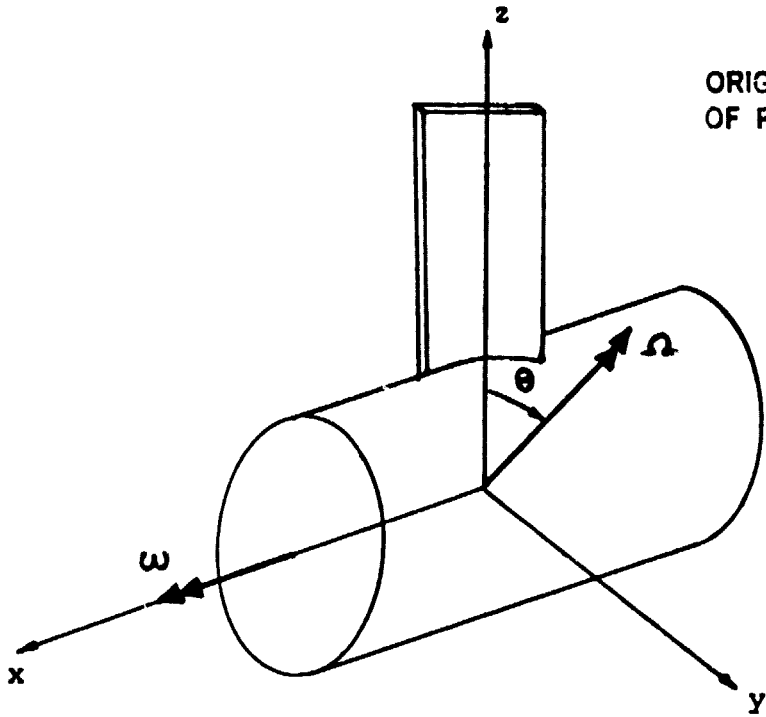


Fig. 1 Space-fixed Precession in the Rotor-fixed Coordinate System  $xyz$

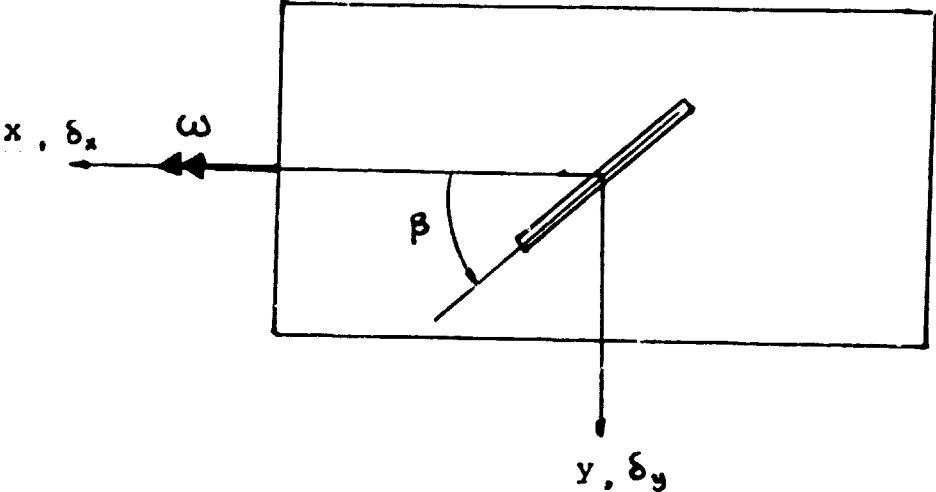


Fig. 2 Setting Angle for Straight Blades

where  $\beta$  is the setting angle measured from the axis of spin to the major axis of the local cross-section, (see Fig. 2) and  $\delta$  is the displacement in the direction of the minor axis of cross section. Furthermore the fore-shortening effect can be written as:

$$\delta_s = -\frac{1}{2} \int_R^z \left( \frac{\partial \bar{\delta}}{\partial z} \right)^2 dz \quad (10)$$

Hence the kinetic energy integral (7) can be completely expressed in terms of the displacement,  $\bar{\delta}(z, t)$  in the flexible direction of the blade. For completeness we retain the terms that contain cross sectional coordinates  $\xi$  and  $\eta$ .

$$\begin{aligned} \vec{v} \cdot \vec{v} = & \dot{\bar{\delta}} + \xi^2 \left( \frac{\partial \bar{\delta}}{\partial z} \right) + 2\xi \left( \frac{\partial \bar{\delta}}{\partial z} \right) \int_R^z \left( \frac{\partial \bar{\delta}}{\partial z} \right) \left( \frac{\partial \bar{\delta}}{\partial z} \right) dz \\ & + \left[ \int_R^z \left( \frac{\partial \bar{\delta}}{\partial z} \right) \left( \frac{\partial \bar{\delta}}{\partial z} \right) dz \right]^2 + \left\{ z^2 - 2z \left( \xi \frac{\partial \bar{\delta}}{\partial z} + \frac{1}{2} \int_R^z \left( \frac{\partial \bar{\delta}}{\partial z} \right)^2 dz \right. \right. \\ & \left. \left. + \xi^2 \left( \frac{\partial \bar{\delta}}{\partial z} \right)^2 + \xi \frac{\partial \bar{\delta}}{\partial z} \int_R^z \left( \frac{\partial \bar{\delta}}{\partial z} \right)^2 dz + \frac{1}{4} \left[ \int_R^z \left( \frac{\partial \bar{\delta}}{\partial z} \right)^2 dz \right]^2 \right\} * \\ & (\omega^2 + \Omega^2 \cos^2 \theta) + (\omega^2 + \Omega^2 \sin^2 \theta) \left\{ \xi^2 \cos^2 \beta + \eta^2 \sin^2 \beta \right. \\ & \left. - \xi \eta \sin 2\beta + 2\xi \bar{\delta} \cos^2 \beta - \eta \bar{\delta} \sin 2\beta + \bar{\delta}^2 \cos^2 \beta \right\} \\ & + \Omega^2 \left\{ \xi^2 \sin^2 \beta + \eta^2 \cos^2 \beta + \eta \xi \sin 2\beta + 2\bar{\delta} \xi \sin^2 \beta \right. \\ & \left. + \eta \bar{\delta} \sin 2\beta + \bar{\delta}^2 \sin^2 \beta \right\} \\ & - \dot{\bar{\delta}} 2\Omega \sin \beta \left\{ \left( z - \xi \frac{\partial \bar{\delta}}{\partial z} - \frac{1}{2} \int_R^z \left( \frac{\partial \bar{\delta}}{\partial z} \right)^2 dz \right) \cos \theta \right. \\ & \left. - (\xi \cos \beta - \eta \sin \beta) \sin \theta \right\} \\ & - \dot{\bar{\delta}} 2 \cos \beta \left\{ \left( z - \xi \frac{\partial \bar{\delta}}{\partial z} - \frac{1}{2} \int_R^z \left( \frac{\partial \bar{\delta}}{\partial z} \right)^2 dz \right) \omega + (\xi \sin \beta + \right. \\ & \left. \eta \cos \beta) \Omega \sin \theta \right\} \end{aligned}$$

$$\begin{aligned}
 & -2 \left\{ \xi \left( \frac{\partial \bar{\delta}}{\partial z} \right) + \int_r^z \left( \frac{\partial \bar{\delta}}{\partial z} \right) \left( \frac{\partial \bar{\delta}}{\partial z} \right) dz \right\} \left\{ \omega (\eta \sin \beta - \xi \cos \beta + \bar{\delta} \cos \beta) \right. \\
 & \quad \left. + \Omega \cos \theta (\xi \sin \beta + \eta \cos \beta + \bar{\delta} \sin \beta) \right\} \\
 & - \left\{ z - \xi \frac{\partial \bar{\delta}}{\partial z} - \frac{1}{2} \int_r^z \left( \frac{\partial \bar{\delta}}{\partial z} \right)^2 dz \right\} (\xi \cos \beta - \eta \sin \beta + \bar{\delta} \cos \beta) \Omega^2 \sin 2\theta \quad (11) \\
 & + \left\{ z - \xi \frac{\partial \bar{\delta}}{\partial z} - \frac{1}{2} \int_r^z \left( \frac{\partial \bar{\delta}}{\partial z} \right)^2 dz \right\} (\xi \sin \beta + \eta \cos \beta + \bar{\delta} \sin \beta) 2 \Omega \omega \sin \theta \\
 & + \left\{ (\xi^2 - \eta^2 + 2 \xi \bar{\delta} + \bar{\delta}^2) \sin 2\beta + 2 (\xi \eta + \bar{\delta} \eta) \cos 2\beta \right\} \omega \Omega \cos \theta
 \end{aligned}$$

Neglecting shear deformations the potential energy is given as:

$$U = \frac{1}{2} \int EI \left( \frac{\partial^2 \bar{\delta}}{\partial z^2} \right)^2 dz \quad (12)$$

With an known displacement function  $\bar{\delta}$  this integral can be evaluated.

### 3.3 Uniform Blades

#### 3.3.1 Equation of Motion

To study the behavior of uniform cantilever blades for which  $t_r = 1$ , we may assume a reasonable distribution of displacements along the blade as follows

$$\bar{\delta}(z, t) = \bar{u}(t) \left( 1 - \cos \frac{\pi(z-R)}{2L} \right) \quad (13)$$

$\bar{u}(t)$  being the tip displacement of the blade. This assumed form is inserted into the kinetic energy T and potential energy U expressions and the Rayleigh-Ritz procedure is applied to both integrals.

From Lagrange's equation

$$\frac{d}{dt} \left( \frac{\partial L}{\partial \dot{\bar{u}}} \right) - \frac{\partial L}{\partial \bar{u}} = 0 \quad (14)$$

where  $L = T - U$ , the equation of the beam tip motion is obtained

$$\begin{aligned} \frac{d^2 \bar{u}}{d\theta^2} + [a_0 + \epsilon^2 a_1 + \epsilon q_1 \cos \theta + \epsilon^2 q_2 \cos 2\theta] \bar{u} \\ - \epsilon q_3 \sin \theta \bar{u}^2 + q_4 \left[ -\bar{u}^3 + 2\bar{u}^2 \frac{d^2 \bar{u}}{d\theta^2} + 2\bar{u} \left( \frac{d\bar{u}}{d\theta} \right)^2 \right] \\ = \epsilon^2 F \sin 2\theta - 2\epsilon F \tan \beta \sin \theta \end{aligned} \quad (15)$$

where the quantities  $a_0, a_1, q_1, q_2, q_3, q_4$  and F are all dependent on blade parameters as follows:

$$\theta = -\omega t \quad (\text{dimensionless time})$$

$$\epsilon = \Omega / \omega \ll 1 \quad (\text{typically about } 0.0001)$$

$$a_0 = \frac{13.42 EI}{mL^3 \omega^2} - \cos^2 \beta + 1.2619 + 1.6173 \frac{R}{L}$$

$$a_1 = -0.369 + 0.5 \cos^2 \beta + 0.809 \frac{R}{L} \quad (16)$$

$$q_1 = -\sin 2\beta$$

$$q_2 = 0.631 + 0.5 \cos^2 \beta + 0.809 \frac{R}{L}$$

$$q_3 = -1.094 \sin \beta / L$$

$$q_4 = 0.608 / L^2$$

$$F = -L \cos \beta \left( 0.5921 + 0.801 \frac{R}{L} \right)$$

The blade parameters are setting angle (stagger)  $\beta$ , blade length  $L$ , rotor radius  $R$ , mass of blade  $m$ , section modulus  $EI$ .  $\omega$  is the rotor spin velocity whereas  $\Omega$  is the magnitude of the space fixed precessional velocity.

The parameters given in equation (16) are for uniform blades. If the blade is tapered these parameters have different expressions and they reflect taper effects. However, the equation of motion (15) retains the same form and the characteristics of the solutions presented in this section remain general.

It should be pointed out here that  $xyz$  coordinates used in equation (15) are rotating with the rotor angular velocity  $\omega$ . Therefore, the tip deflection  $\bar{u}$  is located in a moving coordinate system. This in turn produces the Coriolis term  $(\epsilon q_3 \sin \theta \bar{u}^2)$  which is not explicitly dependent on velocity.

Comparing the parameter  $q_4$  to the other parameters in the differential equation (15),  $q_4$  can be neglected for large blade length



L. Since gyroscopic instability is important for relatively long turbine or fan blades this nonlinear term will be omitted from further consideration in this section. For the time being it is worthwhile to mention that this term is due to higher order effects of the foreshortened axial displacement.

The two terms on the right hand side of equation (15) represent forcing functions. They are generated by the centrifugal acceleration associated with the rotor rotation. The first term is a time function with twice the frequency of the rotor spin i.e. the force becomes zero four times in every rotation. This force vector is in the y direction of the moving coordinate system. The second term is generated by a force vector that is in the x direction of the moving coordinate system. Both inhomogeneous terms on the right hand side of equation (15) represent components of these force vectors that cause blade bending in the  $\bar{u}$  direction.

### 3.3.2 Stability of the Linear Equation of Motion

Equation of motion (15) is nonlinear even though the higher order effects of foreshortened axial displacements are ignored by dropping terms that are dependent on  $q_4$ . In this section we shall omit the other nonlinear term  $\epsilon q_3 \sin \theta \bar{u}^2$ . Since the stability of the motion is determined by the homogeneous part of the equation of motion the linearized equation (15) is reduced to

$$\frac{d^2 \bar{u}}{d\theta^2} + [a_0 + \epsilon^2 a_1 + \epsilon q_1 \cos \theta + \epsilon^2 q_2 \cos 2\theta] \bar{u} = 0 \quad (17)$$

The stability characteristics of this equation was discussed

in reference (5). The equation is identical to the Mathieu equation if the  $\epsilon^2$  terms are ignored. The stability of Mathieu's equation is studied by means of the so-called Strutt diagram, (6). The terms that are of order  $O(\epsilon^2)$  generate additional unstable regions and augment the standard stability regions in the Strutt diagram. The derivation of these stability curves is based on Floquet theory.

The period of the time-dependent coefficient in equation (17) is  $2\pi$ . The perturbation method of strained parameters (7) can be used to determine the periodic solutions of  $\bar{u}$ . This requires the expansion of the solution  $\bar{u}(\theta)$  in terms of

$$\bar{u} = u_0 + \epsilon u_1 + \epsilon^2 u_2 \quad (18)$$

Also it is necessary to expand the dimensionless squared frequency  $a_0$  in terms of  $\epsilon$ .

$$a_0 = b_0 + \epsilon b_1 + \epsilon^2 b_2 \quad (19)$$

Substituting equation (18) and (19) into (17) a set of differential equations are obtained

$$\begin{aligned} \frac{d^2 u_0}{d\theta^2} + b_0 u_0 &= 0 \\ \frac{d^2 u_1}{d\theta^2} + b_0 u_1 &= -(b_1 + q_1 \cos \theta) u_0 \\ \frac{d^2 u_2}{d\theta^2} + b_0 u_2 &= -(b_2 + a_1 q_2 \cos 2\theta) u_0 \\ &\quad - (b_1 + q_1 \cos \theta) u_1 \end{aligned} \quad (20)$$

etc.

The differential equations (20) are solved successively and secular terms are suppressed by imposing conditions on the expansion parameters  $b_1, b_2$ , etc. This is based on Floquet theory for the transition behavior between stable and unstable solutions. The solution of the first differential equation (20) is a harmonic function

$$u_0 = A_0 \cos \sqrt{b_0} \theta + B_0 \sin \sqrt{b_0} \theta \quad (21)$$

with constants  $A_0$  and  $B_0$ . Substituting this expression into the second differential equation (20)

$$\frac{d^2 u_1}{d\theta^2} + b_0 u_1 = -(b_1 + q_1 \cos \theta) u_0 \quad (22)$$

and solving this differential equation yields

$$\begin{aligned} u_1(\theta) = & - \frac{A_0 b_1 \sin \sqrt{b_0} \theta}{2\sqrt{b_0}} + \frac{B_0 b_1 \theta \cos \sqrt{b_0} \theta}{2\sqrt{b_0}} \\ & - \frac{A_0 q_1}{2} \left[ \frac{\cos(1 - \sqrt{b_0})\theta}{2\sqrt{b_0} - 1} - \frac{\cos(1 + \sqrt{b_0})\theta}{2\sqrt{b_0} + 1} \right] \\ & - \frac{B_0 q_1}{2} \left[ \frac{\sin(1 - \sqrt{b_0})\theta}{2\sqrt{b_0} - 1} + \frac{\sin(1 + \sqrt{b_0})\theta}{2\sqrt{b_0} + 1} \right] \end{aligned} \quad (23)$$

The first two terms on the right hand side of (23) are secular terms. Additional secular terms arise when  $\sqrt{b_0} = 1/2$ . If this analysis is carried out further by inserting the above solution (23) into the third differential equation (20) it is determined that

besides  $\sqrt{b_0} = 1/4$  ,  $\sqrt{b_0} = 1$  also gives rise to more secular terms. Analysis in the higher powers of  $\epsilon$  generates even more secular terms but for most practical purposes  $O(\epsilon^2)$  is accurate enough.

Starting with  $\sqrt{b_0} = 1/2$  equation (22) becomes

$$\begin{aligned} \frac{d^2 u_1}{d\theta^2} + \frac{1}{4} u_1 &= (-b_1 - \frac{q_1}{2}) A_0 \cos \frac{1}{2} \theta + (-b_1 + \frac{q_1}{2}) B_0 \sin \frac{1}{2} \theta \\ &- \frac{q_1 A_0}{2} \cos \frac{3\theta}{2} - \frac{q_1 B_0}{2} \sin \frac{3\theta}{2} \end{aligned} \quad (24)$$

Eliminating the secular terms in (24) requires that either

$$b_1 = -\frac{q_1}{2} \quad , \quad B_0 = 0 \quad (25)$$

or

$$b_1 = \frac{q_1}{2} \quad , \quad A_0 = 0 \quad (26)$$

The two values of  $b_1$  in equations (25) and (26), when inserted into equation (19), correspond to two different stability transition curves in the  $(a_0, \epsilon)$  plane. These curves separate stable from unstable regions.

Using these results, the second order approximation of the transition curves can be obtained by eliminating secular terms in the solution of the third differential equation in (20). This requires that

$$(b_2 + a_1 + \frac{1}{8} q_1^2) A_0 = 0 \quad (27)$$

and

$$(b_2 + a_1 + \frac{1}{8} q_1^2) B_0 = 0 \quad (28)$$

Equations (27) and (28) indicate that

$$b_2 = -a_1 - \frac{1}{8} q_1^2 \quad (29)$$

is the sufficient condition for the elimination of secular terms in  $u_2$ .

Equations (25), (26), and (29) are inserted into (19) to obtain the equations for the two transition curves that emanate from  $a_0 = 1/4, \epsilon = 0$ .

$$a_0 = \frac{1}{4} \pm \epsilon \frac{q_1}{2} - \epsilon^2 \left( a_1 + \frac{1}{8} q_1^2 \right) \quad (30)$$

The above process is repeated at the other singular point:  $a_0 = 1$  and  $\epsilon = 0$ . The transition curves are described by

$$a_0 = 1 + \epsilon^2 \left[ \frac{5q_1^2}{12} - \frac{q_2}{2} - a_1 \right] \quad (31)$$

and

$$a_0 = 1 + \epsilon^2 \left[ -\frac{q_1^2}{12} + \frac{q_2}{2} - a_1 \right] \quad (32)$$

Emanating from each singular point on the  $a_0$  axis of  $(a_0, \epsilon)$  plane there are two transition curves. The loci of transition values separate the  $(a_0, \epsilon)$  plane into regions of stability and regions of instability. Additional unstable regions can be derived for higher values of  $a_0$ . However, these regions of instability are narrow (order of  $\epsilon^3$ ) and do not have much practical significance.

In the stable regions equation of motion (15) can be approximated by the following differential equation.

$$\frac{d^2 \bar{u}}{d\theta^2} + a_0 \bar{u} = \epsilon^2 F \sin 2\theta - 2\epsilon F \tan \beta \sin \theta \quad (33)$$

This approximation is not valid in the unstable regions of the  $(a_0, \epsilon)$  plane.

### 3.3.3 Numerical Example

The equations (30), (31) and (32) for stability transition curves derived by the perturbation method contain blade parameters  $\beta$ ,  $R/L$  etc. In this section using these equations for some typical blade we may construct a stability chart. The stability chart of Fig. 12 is given for a particular set of blade parameters,  $R/L = 1.384$ ,  $L = 10$  in.,  $\beta = -45^\circ$  which yields the following parameters  $a_1 = 1$ ,  $q_1 = 1$ , and  $q_2 = 2$ .

For every pair of curves that emanates from the discrete  $a_0$  values, the region between the transition curves correspond to  $(a_0, \epsilon)$  values which give unbounded solutions of the equation of motion. Therefore these are regions of instability. It should be noted that the unstable region at  $a_0 = 1$  is considerably narrower than the region at  $a_0 = 1/4$ .

We now check the validity of the stability transition curves that are given in Fig. 12 by an independent numerical procedure. According to reference (8) the solutions of the homogeneous differential equation (17) are stable if

$$|v_1(2\pi) + v_2'(2\pi)| < 2 \quad (34)$$

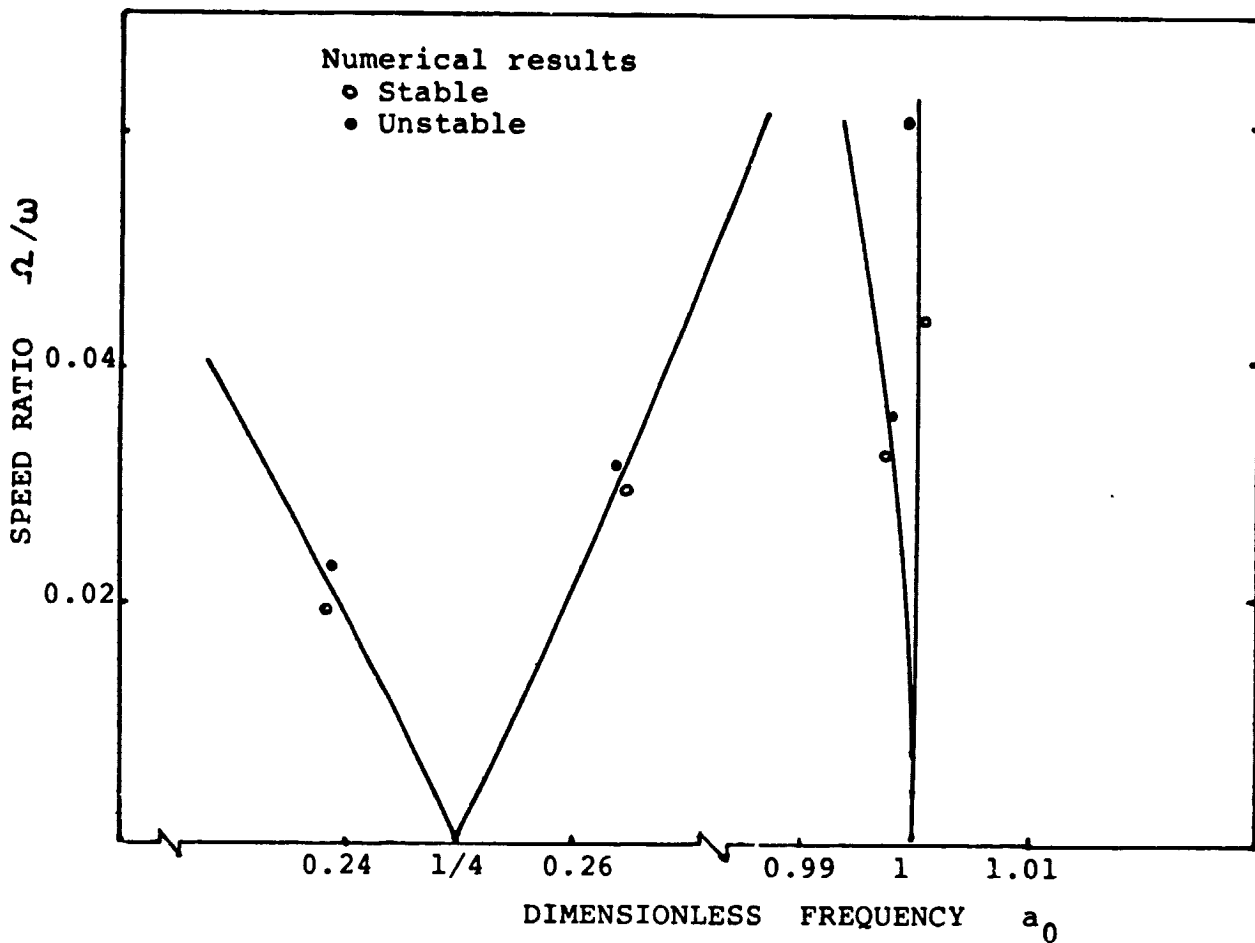


Fig. 3 Stability Chart for the Linear Equation of Motion

where  $v_1(\theta)$  and  $v_2(\theta)$  are numerical solutions of (17) with the following initial conditions

$$\begin{aligned} v_1(0) &= 1, & v_1'(0) &= 0 \\ v_2(0) &= 0, & v_2'(0) &= 1 \end{aligned} \tag{35}$$

The predictor-corrector numerical scheme of Adams-Bashforth was used to obtain  $v_1(\theta)$  and  $v_2(\theta)$  for given  $(a_0, \epsilon)$  values when  $a_1 = 1$ ,  $q_1 = 1$ , and  $q_2 = 2$ . The stable and unstable points are marked on the stability chart of Fig. 3. Excellent agreement is observed with the results of perturbation methods.

### 3.3.4 Effect of the Nonlinear Coriolis Term

If the nonlinear Coriolis term,  $\epsilon q_3 \sin \theta \bar{u}^2$  is retained in the equation of motion (15) a general stability analysis becomes impossible. However certain predictions can be made about systems which have the form

$$\frac{d^2 \bar{u}}{d\theta^2} + a_0 \bar{u} = \epsilon f(\nu\theta, \bar{u}, \frac{d\bar{u}}{d\theta}) \tag{36}$$

where  $\epsilon$  is small and  $f(\nu\theta, \bar{u}, \frac{d\bar{u}}{d\theta})$  is periodic with a period  $2\pi$  in the product variable  $\nu\theta$ . In these systems "resonance" occurs only if

$$\sqrt{a_0} \approx \frac{q}{p} \nu \tag{37}$$

where  $p$  and  $q$  are small and mutually prime integers (9). If  $\sqrt{a_0}$  is irrational and cannot be obtained by the division of two integers the solutions to (36) are not periodic but usually bounded. Therefore



it suffices to make the stability analysis of (15) for only those  $\sqrt{a_0}$  values which can be represented as a division of two mutually prime integers

$$\sqrt{a_0} = \frac{q}{p} \quad (38)$$

Neglecting terms that depend on  $q_4$ , the equation of motion (15) can be written in the form of equation (36). The coefficient  $\epsilon$  in this equation is the ratio of the precessional angular velocity  $\Omega$  to the spin angular velocity  $\omega$ . In general this ratio is very small compared to  $a_0$ . Therefore it can be expected that the solution of (15) is nearly harmonic. An approximate linearized differential equation can be obtained by assuming that the solution consists of two parts:

$$\bar{u} = u_L + \epsilon u \quad (39)$$

The first part  $u_L$  satisfies the equation:

$$\frac{d^2 u_L}{d\theta^2} + a_0 u_L = 0 \quad (40)$$

which has the solution:

$$u_L = A_L \cos \sqrt{a_0} \theta + B_L \sin \sqrt{a_0} \theta \quad (41)$$

Substituting equations (39) and (40) into equation (15) and linearizing by neglecting the  $(\epsilon u)^2$  term, results in

$$\frac{d^2 u}{d\theta^2} + [a_0 + \epsilon^2 a_1 + \epsilon q_1 \cos \theta + \epsilon^2 q_2 \cos 2\theta]$$

$$- \epsilon 2q_3 \sin \theta u_L] u$$

ORIGINAL PAGE IS  
OF POOR QUALITY

$$= \epsilon F \sin 2\theta - 2\epsilon F \tan \beta \sin \theta$$

$$+ q_3 \sin \theta u_L^2$$

$$- (\epsilon a_1 + q_1 \cos \theta + \epsilon q_2 \cos 2\theta) u_L$$

(42)

The stability of the above differential equation can be studied by considering the homogeneous part only.

$$\frac{d^2 u}{d\theta^2} + [a_0 + \epsilon^2 a_1 + \epsilon q_1 \cos \theta + \epsilon^2 q_2 \cos 2\theta$$

$$- \epsilon 2q_3 \sin \theta u_L] u = 0$$

(43)

Under the condition of equation (38) the period of the coefficient of  $u$  in the above differential equation is  $2p\pi$ . Furthermore the stability of this differential equation can be studied by means of Floquet theory.

Here we apply the perturbation method of strained parameters, again.

$$u = u_0 + \epsilon u_1 + \epsilon^2 u_2$$

(44)

$$a_0 = b_0 + \epsilon b_1 + \epsilon^2 b_2$$

(45)

Substituting the above equations into (43) a set of differential equations are obtained

$$\frac{d^2 u}{d\theta^2} + b_0 u_0 = 0$$

$$\frac{d^2 u_1}{d\theta^2} + b_0 u_1 = -(b_1 + q_1 \cos \theta - 2q_2 \sin \theta u_1) u_0$$

$$\frac{d^2 u_2}{d\theta^2} + b_0 u_2 = -(b_2 + q_1 + q_2 \cos 2\theta) u_0$$

$$-(b_1 + q_1 \cos \theta - 2q_2 \sin \theta u_1) u_1$$

(46)

etc.

The differential equations (46) are solved successively and secular terms are suppressed by imposing conditions on the expansion parameters  $b_1$ ,  $b_2$ , etc. The solution of the first differential equation in (46) is an harmonic function

$$u_0 = A_0 \cos \sqrt{b_0} \theta + B_0 \sin \sqrt{b_0} \theta \quad (47)$$

with constants  $A_0$  and  $B_0$ . Substituting this equation into the second differential equation in (46)

$$\frac{d^2 u_1}{d\theta^2} + b_0 u_1 = -(b_1 + q_1 \cos \theta - 2q_2 \sin \theta u_1) u_0 \quad (46)$$

and solving this differential equation it is determined that secular terms arise when  $\sqrt{b_0} = 1$ ,  $\sqrt{b_0} = 1/2$ , and  $\sqrt{b_0} = 1/3$ .

As before, the differential equation (48) has to be solved for these specific values of  $b_0$  and the secular terms that arise must be eliminated by imposing conditions on  $b_1$ .

Starting with  $b_0 = 1/9$ , equation (48) is

$$\begin{aligned} \frac{d^2 u_1}{d\theta^2} + \frac{1}{9} u_1 = & -b_1 A_0 \cos \frac{\theta}{3} - b_1 B_0 \sin \frac{\theta}{3} \\ & + \frac{1}{2} A_0 A_L q_3 \sin \frac{\theta}{3} + \frac{1}{2} A_0 B_L q_3 \cos \frac{\theta}{3} \\ & + \frac{1}{2} B_0 A_L q_3 \cos \frac{\theta}{3} - \frac{1}{2} B_0 B_L q_3 \sin \frac{\theta}{3} + \dots \end{aligned} \quad (49)$$

Eliminating the secular terms in (49) requires that

$$\begin{aligned} -b_1 A_0 + \frac{1}{2} B_L q_3 A_0 + \frac{1}{2} A_L q_3 B_0 &= 0 \\ -b_1 B_0 - \frac{1}{2} B_L q_3 B_0 + \frac{1}{2} A_L q_3 A_0 &= 0 \end{aligned} \quad (50)$$

Equations (50) can be written in matrix form

$$\begin{bmatrix} -b_1 + \frac{q_3}{2} B_L & \frac{q_3}{2} A_L \\ \frac{q_3}{2} A_L & -b_1 - \frac{q_3}{2} B_L \end{bmatrix} \begin{Bmatrix} A_0 \\ B_0 \end{Bmatrix} = \begin{Bmatrix} 0 \\ 0 \end{Bmatrix} \quad (51)$$

ORIGINAL FILED  
OF POOR QUALITY

To obtain nontrivial solutions the determinant of the coefficient matrix must be zero. This yields the following equation

$$b_1^2 - \frac{q_3^2}{4} (A_L^2 + B_L^2) = 0$$

or

$$b_1 = \pm \frac{q}{2} \sqrt{A_L^2 + B_L^2} \quad (52)$$

The two values of  $b_1$  in equation (52), when inserted into equation (45), correspond to two different stability transition curves that emanate from  $a_0 = 1/9$ ,  $\epsilon = 0$ .

For each  $b_1$  that is obtained from equation (52) the corresponding relation between  $A_0$  and  $B_0$  is determined from equation (51).

$$\frac{A_0}{B_0} = \frac{B_L \pm \sqrt{A_L^2 + B_L^2}}{A_L} \quad (53)$$

When this analysis is extended to the second power of  $\epsilon$  we face an inconsistency that prevents us from eliminating the secular terms. For each transition curve that corresponds to a particular  $b_1$  value we obtain two conditions on  $b_2$  instead of one.

$$b_2 = -a_1 - \frac{q}{10} q_1^2 + \frac{q}{8} q_3^2 B_L \sqrt{A_L^2 + B_L^2} - (39A_L^2 - 33B_L^2) \frac{q_3^2}{32} \quad (54)$$

$$b_2 = -a_1 - \frac{9}{10} q_1^2 + \frac{9}{8} q_3^2 B_L \sqrt{A_L^2 + B_L^2} - (75 \Omega_L^2 + 3 A_L^2) \frac{q_3^2}{32}$$

(55)

Obviously conditions (54) and (55) cannot be satisfied simultaneously for arbitrary  $A_L$  and  $B_L$ . Examining the two expressions for  $b_2$  in these equations, the difference is in the last term of the equations. If these terms are neglected the perturbation solution (44) will not be exactly periodic due to  $u_2$ . The prerequisites for applying Floquet theory to the transition curve will be violated. The method of strained parameters fails to determine the stability transition curves to the second and also to higher powers of  $\epsilon$ . Therefore the solution so obtained is not uniformly valid as  $t \rightarrow \infty$ . Other perturbation methods have been tried without success in resolving this inconsistency. This remains a mathematical problem that may be tackled rigorously at a future time.

Fortunately, in most practical cases the ratio,  $\epsilon$ , of precessional speed to rotor spin is small. The numerical error resulting from omitting these inconsistent terms is negligible. In order to verify these approximated stability curves the independent numerical method of previous section is applied to the linear equation (43) directly. This is presented in the next section.

The approximate equations (54) and (55) for  $b_2$  and equation (52) for  $b_1$  are inserted into (45) to obtain the equations for the two transition curves that emanate from  $a_0 = 1/9$ ,  $\epsilon = 0$ .

$$a_0 = \frac{1}{9} \pm \epsilon \frac{q_3}{2} \sqrt{A_L^2 + B_L^2} - \epsilon^2 \left[ a_1 + \frac{9}{10} q_1^2 \pm \frac{9}{8} q_3^2 B_L \sqrt{A_L^2 + B_L^2} \right] \quad (56, 57)$$

The above process is repeated at other singular points:  $\epsilon = 0$  and  $a_0 = 1/4, 1$  etc. The approximate transition curves at  $a_0 = 1/4$  are

$$a_0 = \frac{1}{4} + \epsilon \frac{q_1}{2} + \epsilon^2 \left[ -a_1 - \frac{q_1^2}{8} + \frac{q_3^2}{15} (14A_L^2 - 6B_L^2) \right] \quad (58)$$

$$a_0 = \frac{1}{4} - \epsilon \frac{q_1}{2} + \epsilon^2 \left[ -a_1 - \frac{q_1^2}{8} + \frac{q_3^2}{15} (14B_L^2 - 6A_L^2) \right] \quad (59)$$

and at  $q = 1$  are

$$a_0 = 1 + \epsilon \frac{q_3}{2} \left[ 2B_L \pm \sqrt{A_L^2 + B_L^2} \right] - \epsilon^2 \left[ a_2 - \frac{q_3^2}{32} (A_L^2 + B_L^2) \right] \quad (60, 61)$$

It should be mentioned that these are not the only stability curves. Additional unstable regions can be derived for higher values of  $a_0$ . However, these additional regions are exceedingly narrow and therefore they are less important.

All of these transition curves contain  $A_L$  and  $B_L$  which are the initial condition constants of the basic solution  $u_L$ . The dependence of stability on the initial conditions is typical for nonlinear systems. But these transition curves do not depend on the constants  $A_0$  and  $B_0$  in equation (47) of the perturbed solution. This indicates that the stability curves are valid for any arbitrary initially perturbed motion.

### 3.3.5 Numerical Example

The equations for stability transition curves (56), (57), (58), (59), (60), and (61) contain the initial condition constants  $A_L$  and  $B_L$  as well as the blade parameters  $\beta$ ,  $R/L$ ,  $L$  etc. For each of these parameters one can construct a family of stability curves while the other parameters are held constant. We choose to examine the effect of initial conditions on the stability curves for a given set of blade parameters.

Stability charts of Figs. 4, 5, 6 are constructed for the same blade data that were used in section 4.3.3 which yield  $a_1 = 1$ ,  $q_1 = 1$ ,  $q_2 = 2$ , and  $q_3 = 0.1547$ .

For this purpose two dimensionless initial value parameters,  $\eta_1$  and  $\eta_2$  are defined as follows:

$$\eta_1 = \frac{A_L}{L}$$

$$\eta_2 = \frac{B_L}{L}$$

(62)



Note that  $A_L$  is the initial displacement,  $u_L(0)$  and  $B_L$  is proportional to the initial velocity.

Fig. 4, Fig. 5, and Fig. 6 correspond to different initial displacement values,  $\eta_1 = 0$ ,  $\eta_1 = 0.05$ , and  $\eta_1 = 0.1$  respectively. In each figure four pairs of transition curves are drawn for four different values of  $\eta_2$  : 0, 0.05, 0.1, and 0.5. Note that  $\eta_2 = 0.5$  corresponds to a significant initial speed. For example, if the spin velocity is 4000 rpm the initial speed for the transition curves emanating from  $a_0 = 1/4$  is 87 ft/sec.

In the unstable regions, between a pair of curves emanating from discrete  $a_0$  values, the perturbed motion  $u$  grows and consequently, according to equation (39), the blade tip motion  $\bar{u}$  is unstable.

In Fig. 4 the transition curves for  $\eta_1 = \eta_2 = 0$  are of particular interest. These are stability transition curves when the nonlinear Coriolis term is not taken into consideration as given in section 4.3.3. From the expressions for stability curves it can be seen that if the Coriolis term is neglected the stability characteristics of the blade tip motion will not depend on initial conditions ( $A_L, B_L$ ). This is expected since the stability of linear systems should be independent of initial conditions. Also when there is no initial motion ( $A_L = 0, B_L = 0$ ) relative to the spinning system the Coriolis acceleration does not effect the stability regions.

An interesting effect of Coriolis acceleration is the creation of additional region of instability at  $a_0 = 1/9$ . This region is not predicted by the linear analysis of section 3.3.2.

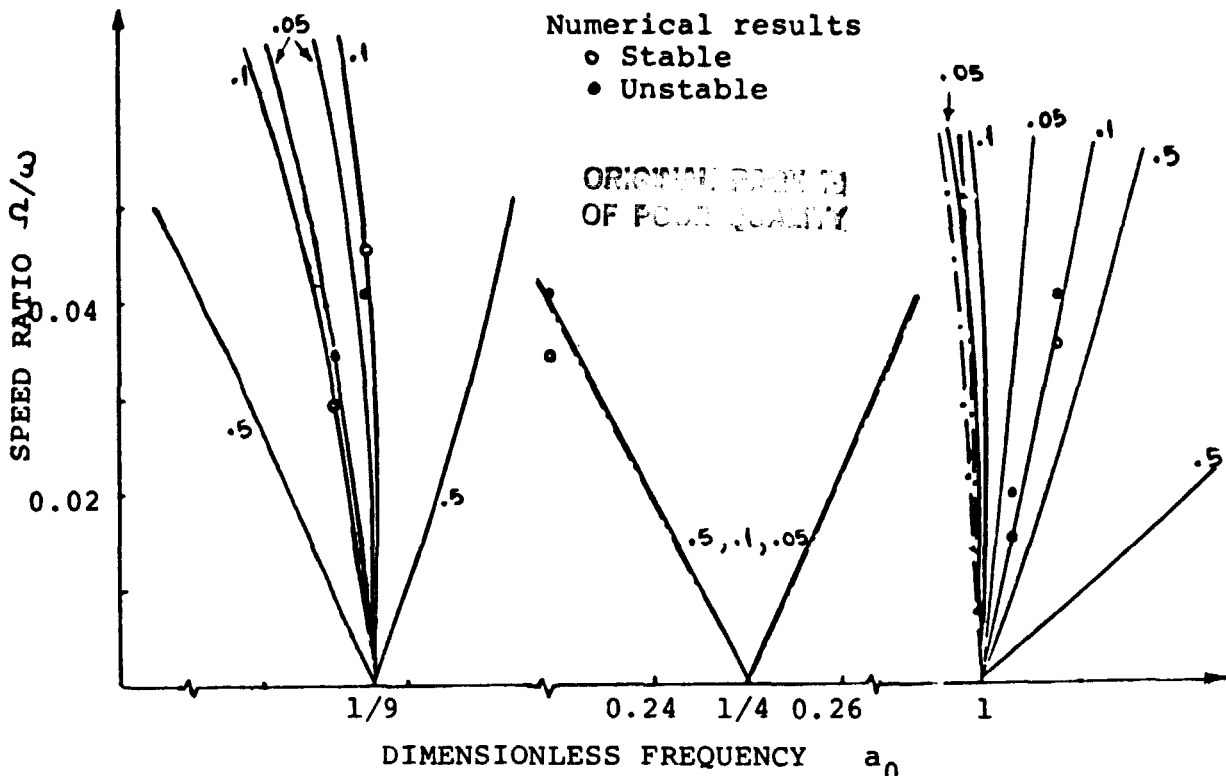


Fig. 4 Stability Chart for Zero Initial Displacement  $\eta_1 = 0$  and for Different Initial Speed  $\eta_2$   
 -----  $\eta_2 = 0$

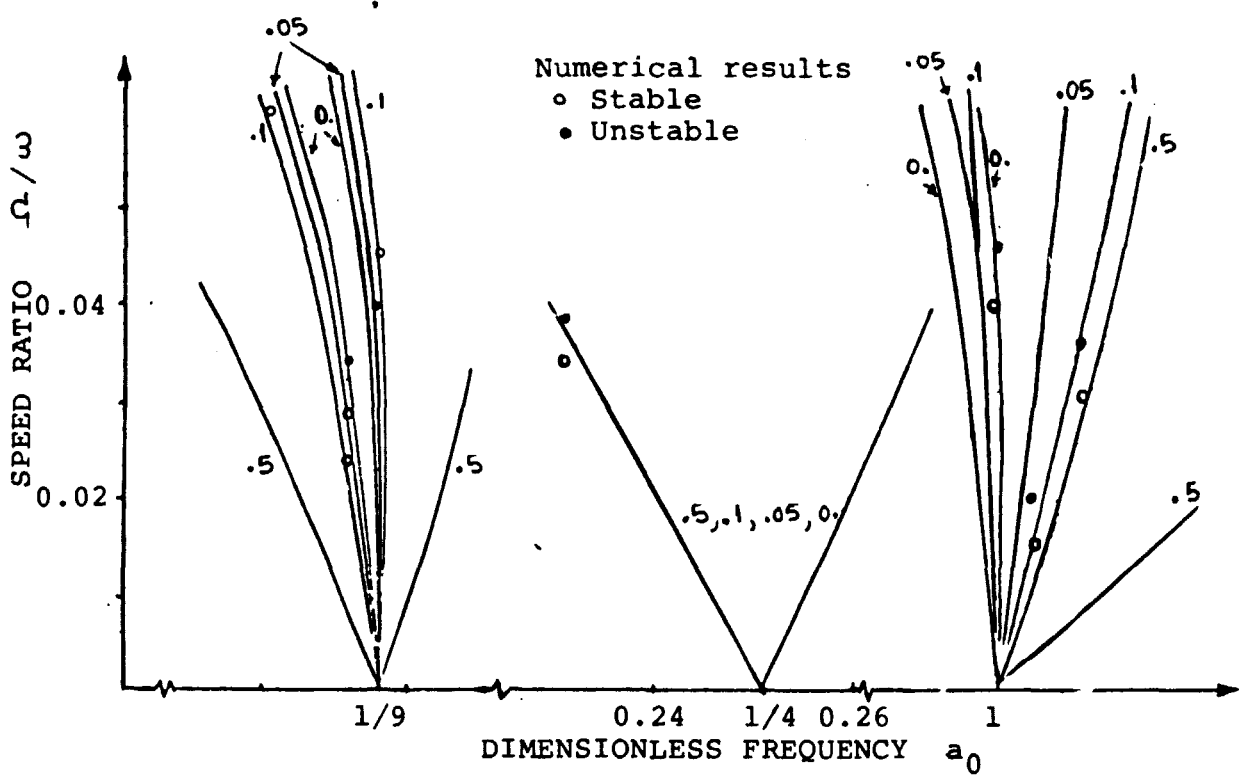


Fig. 5 Stability Chart for Initial Displacement  $\eta_1 = 0.05$  and for Different Initial Speed  $\eta_2$

ORIGINAL PAGE IS  
OF POOR QUALITY

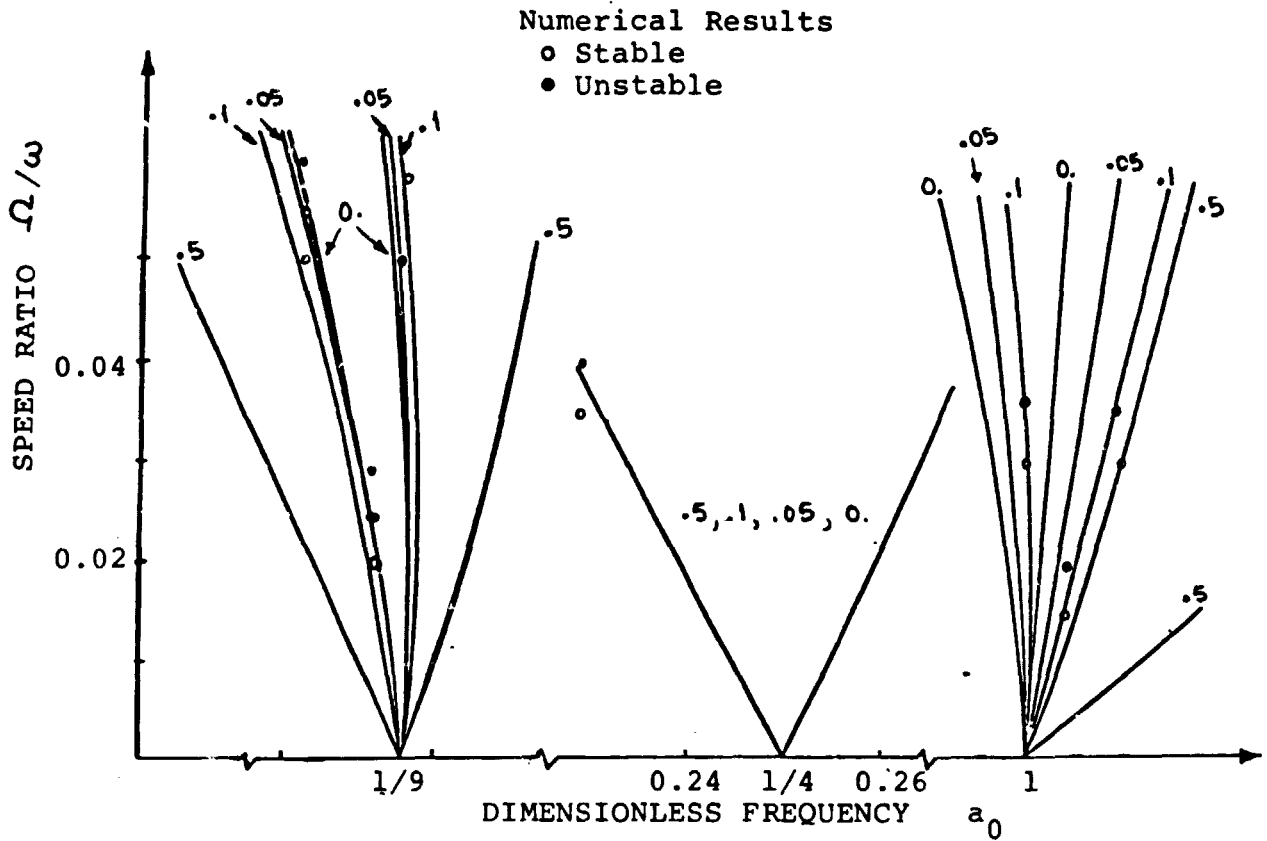


Fig. 6 Stability Chart for Initial Displacement  $\eta_1 = 0.1$   
and for Different Initial Speed  $\eta_2$

Unstable regions at  $a_0 = 1/9$  and  $a_0 = 1$  are quite narrow for practical initial values ( $\eta_1 < 0.1$ ,  $\eta_2 < 0.05$ ) and widen for increased values of initial condition parameters  $\eta_1$  and  $\eta_2$ . On the other hand, the unstable region at  $a_0 = 1/4$  does not depend on the initial conditions. This region was predicted by linear analysis and is unaffected from the nonlinear Coriolis term.

Studying the three stability charts it might be concluded that for moderate initial values and low precession rates the effect of Coriolis force on motion stability can be neglected for blades undergoing gyroscopic motion.

So far the stability of tip motion has been analyzed by the perturbation method. Because of the uncertainty in the accuracy of this method it was decided to verify the stability charts presented in Fig. 4, Fig. 5, and Fig. 6 by the numerical procedure that was described in section 3.3.3. The solutions to the linearized equation (43) are stable if

$$|v_1(2p\pi) + v_2'(2p\pi)| < 2 \quad (63)$$

where  $v_1(\theta)$  and  $v_2(\theta)$  are numerical solutions of equation (43) with the following initial conditions

$$\begin{aligned} v_1(0) = 1 \quad , \quad v_1'(0) = 0 \\ v_2(0) = 0 \quad , \quad v_2'(0) = 0 \end{aligned} \quad (64)$$

Using this numerical method the transition curves that correspond to  $\eta_2 = 0.1$  are checked. The stable and unstable  $(a_0, \epsilon)$  points that are predicted by the numerical method are marked on the

stability charts of Fig. 4, Fig. 5, and Fig. 6. They indicate that the stability curves obtained from the perturbation method are quite reliable.

### 3.3.6 Forced Vibrations

The equation of motion (15) indicates that the gyroscopic beam motion is a forced vibratory motion. From the stability analysis it has been determined that the motion in the unstable regions of the  $(a_0, \epsilon)$  plane is unbounded. This is due to the fact that the forcing function initiates vibrations which lead to parametric resonance. Hence it is only necessary to give the forced response away from the resonance regions.

In the stable regions the solution to the equation of motion (15) can be assumed to be

$$\bar{u} = u_L + \epsilon u \quad (65)$$

where  $u_L$  now includes the forced response

$$\frac{d^2 u_L}{d\theta^2} + a_0 u_L = \epsilon^2 F \sin 2\theta + 2\epsilon F \cot \beta \sin \theta \quad (66)$$

where  $F$  is given in equation (16) and is in the order of  $O(L)$ , and  $u$  is the perturbed solution due to the remaining terms in (15) expecting the  $q_4$  term. As indicated before the terms with  $q_4$  has not been included in our analysis for the reasons noted earlier.

In the stable regions the perturbed motion is bounded.

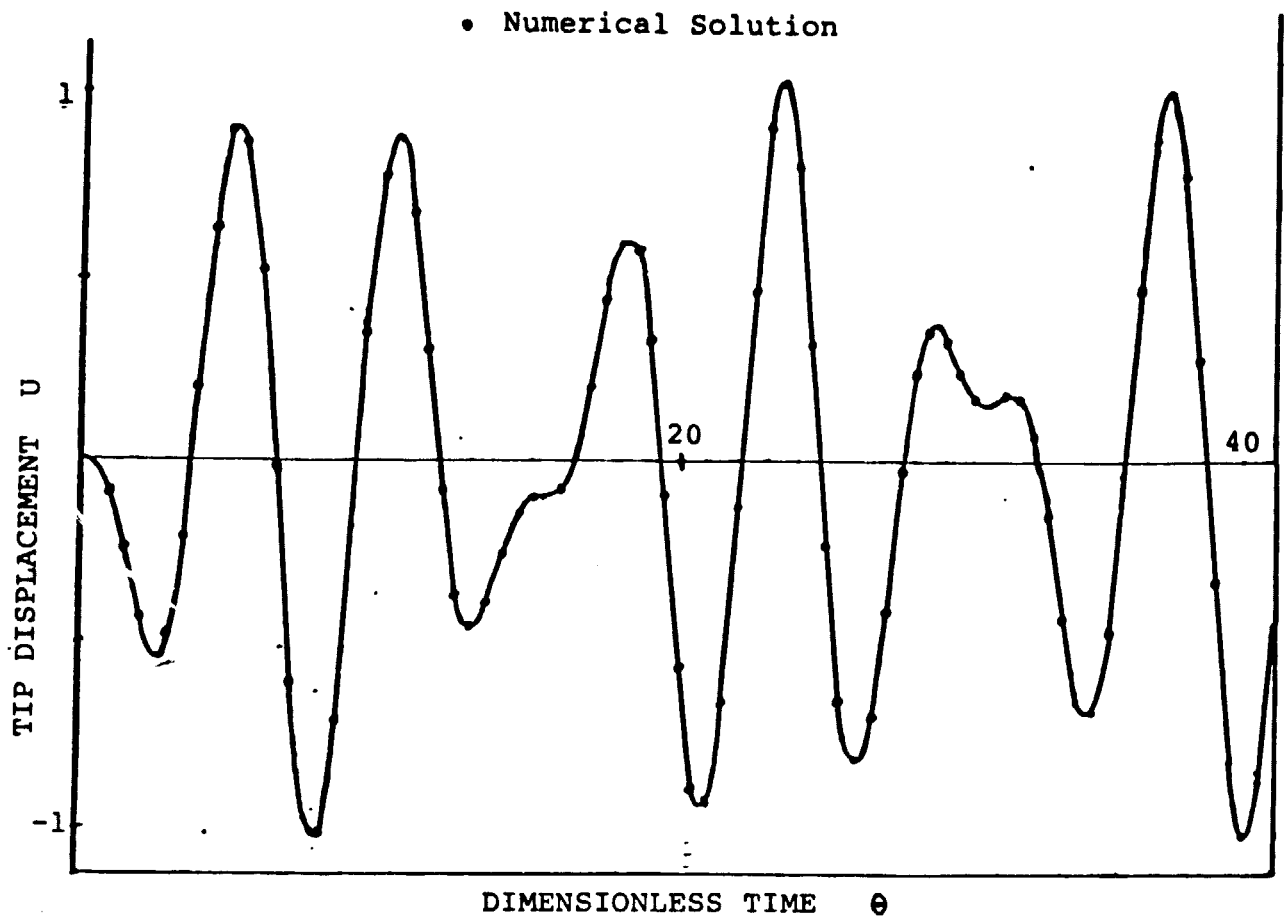


Fig. 7 Comparison of Numerical and Approximate Solutions in the Stable Region with Zero Initial Conditions

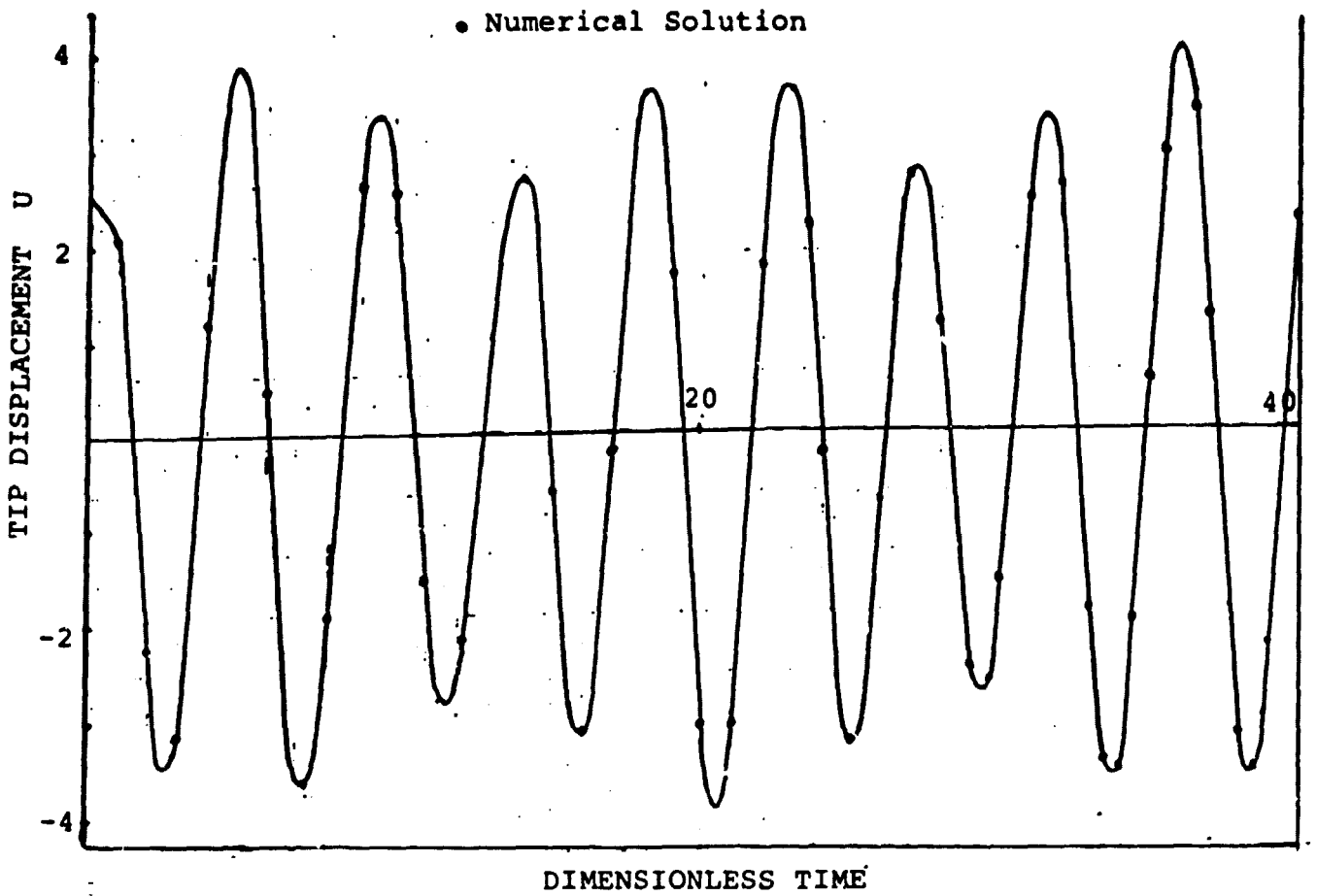


Fig. 8 Comparison of Numerical and Approximate Solutions in the Stable Region When Initial Conditions are  $\bar{u}(0)=2.54$  cm and  $\frac{d\bar{u}}{d\theta}=2.54$  cm

From equation (65) the error in taking  $u_L$  equal to  $\bar{u}$  is in the order of  $\epsilon$ . Therefore in the stable region the forced response of the equation of motion (15) with error of order  $\epsilon$  can be obtained from equation (66) directly

$$\bar{u} \approx u_L = A \cos \sqrt{a_0} \theta + B \sin \sqrt{a_0} \theta + \frac{\epsilon^2 F}{a_0 - 4} \sin 2\theta + \frac{2\epsilon F}{a_0 - 1} \cot \beta \sin \theta \quad (67)$$

where

$$A = \bar{u}(0)$$

$$\beta = \frac{1}{\sqrt{a_0}} \left[ \left. \frac{d\bar{u}}{d\theta} \right|_{\theta=0} - \frac{2\epsilon^2 F}{a_0 - 4} - \frac{2\epsilon F \cot \beta}{a_0 - 1} \right] \quad (68)$$

The peak value of (67) can be determined by summing the amplitudes of individual harmonics:

$$|\bar{u}|_{\max} = \sqrt{A^2 + B^2} + \left| \frac{\epsilon^2 F}{a_0 - 4} \right| + \left| \frac{2\epsilon F \cot \beta}{a_0 - 1} \right| \quad (69)$$

To check the validity of the solution (67) the equation of motion (15), disregarding the  $q_4$  term, is integrated directly. The predictor-corrector numerical scheme of Adams-Bashforth is used again. Both the numerical solution and the approximate solution are plotted in Figs. 7 and 8. Fig. 7 is constructed with zero initial conditions whereas in Fig. 17 the initial values are  $u(0) = 1$  in.,  $\left. \frac{d\bar{u}}{d\theta} \right|_{\theta=0} = 1$  in.



which corresponds to  $\left. \frac{d\bar{u}}{dt} \right|_{t=0} = \omega$  in/sec. The solutions in Fig. 7 and Fig. 8 correspond to a stable point in the  $(a_0, \epsilon)$  plane which is  $a_0 = 2$  and  $\epsilon = 0.01$ . The particular blade data used in these figures is the same as those used in the stability chart.

The approximate solution of (15) in the stable region which are obtained from equation (67) are in very good agreement with direct numerical solutions of (15) as can be seen in Figs. 7 and 8. For smaller and more realistic  $\epsilon$  values the accuracy of the approximate solution will be even better.

The previous discussion leads us to conclude that for practical purposes the peak value of the vibratory motion which is governed by equation (15) can be predicted from equation (69) provided the particular blade and rotary data correspond to points inside the stable region of the  $(a_0, \epsilon)$  plane. It is worthwhile to note that bending moments associated with peak tip displacements in this case ( $\epsilon = 0.01$ ) are acceptable. Therefore the forced motion of a blade under gyroscopic disturbance is generally less important than the corresponding parametric stability problem.

### 3.4 Blades with Different Geometry

In this part we show how to modify the analysis of previous section to take into account some common blade geometry, namely tapered cross sections and shrouding of blades. It can be shown that these properties do not change the general form of equation of motion (15). The parameters in equation (16) are changed however.

They include blade geometry effects. Since the differential equation of motion (15) preserves its original form the stability analysis of previous section remains valid.

### 3.4.1 Tapered Cantilever Blades

In section 3.3.1 we have given equation of motion for uniform blades that have a taper parameter,  $t_r = 1$ . If  $t_r \neq 1$  the parameters in equation (16) take the following form

$$\theta = -\omega t$$

$$\epsilon = \Omega / \omega$$

$$N = 0.2268 + 0.184 (t_r - 1)$$

$$q_0 = \frac{1}{N} \left\{ \frac{EA^2 (0.2537)}{\rho b^2 L^4 \omega^2} \left[ \frac{(t_r + 1)(t_r^2 + 1)}{4} - \frac{6(t_r - 1) [\pi^2 t_r^2 - 3(t_r - 1)^2]}{\pi^4} \right] \right\} \quad (70)$$

$$+ 0.2862 + 0.3668 \frac{R}{L} - 0.2268 \cos^2 \beta$$

$$+ (t_r - 1) \left( 0.2341 + 0.2862 \frac{R}{L} - 0.196 \cos^2 \beta \right) \left. \vphantom{\frac{EA^2 (0.2537)}}{}} \right\}$$

$$q_1 = \frac{1}{N} \left\{ -0.0837 + 0.1834 \frac{R}{L} + 0.1134 \cos^2 \beta \right.$$

$$\left. + (t_r - 1) \left( -0.069 + 0.1431 \frac{R}{L} + 0.093 \cos^2 \beta \right) \right\}$$

$$q_2 = -\sin 2\beta \quad (\text{unchanged})$$

$$q_2 = \frac{1}{N} \left\{ 0.1431 + 0.1834 \frac{R}{L} + 0.1134 \cos^2 \beta \right. \\ \left. + (t_r - 1) \left( 0.1171 + 0.1431 \frac{R}{L} + 0.093 \cos^2 \beta \right) \right\}$$

$$q_3 = -\frac{1}{N} \frac{\sin \beta}{L} \left[ 0.2482 + (t_r - 1) 0.2082 \right]$$

$$F = -\frac{L \cos \beta}{N} \left[ 0.1343 + 0.1817 \frac{R}{L} + (t_r - 1) \right. \\ \left. \left( 0.1064 + 0.1344 \frac{R}{L} \right) \right] \quad (70 \text{ cont.})$$

The new blade parameters which appear in the above equation (70) are material density,  $\rho$ , the width of the blade,  $b$  which is assumed constant, the root cross sectional area,  $A$  and  $t_r$ , the area ratio of the tip to the root.  $N$  is some shape factor which is defined above.

### 3.4.2 Tapered Blades with a Shroud at $z = R + 3L/4$

Except the assumed displacement distribution (13) the general procedure described in Section 4.2 and Section 4.3 is exactly repeated. The assumed displacement shape is now

$$\bar{\delta}(z, t) = \bar{u}(t) \left[ 4 \left( \frac{z-R}{L} \right)^3 - 3 \left( \frac{z-R}{L} \right)^2 \right] \quad (71)$$

which satisfies the geometric boundary conditions since

$$\bar{\delta}(R, t) = \bar{\delta}\left(R + \frac{3}{4}L, t\right) = 0$$

$$\frac{\partial \bar{\delta}}{\partial z}(R, t) = 0 \quad (72)$$

$\bar{u}(t)$  is again the tip displacement at  $z = R + L$ .

For this case the parameters in equation (16) of cantilever blades take the following form

$$\theta = -\omega t$$

$$\epsilon = \Omega / \omega$$

$$N = 0.0857 + (t_r - 1) 0.0714$$

$$a_0 = \frac{EA^2}{N \rho b^2 L^4 \omega^2} \left\{ 3.933 (t_r - 1)^3 + 13.8 (t_r - 1)^2 + 16.5 (t_r - 1) + 7 \right\}$$

$$+ \frac{1}{N} \left\{ 0.05719 + 0.0857 \frac{R}{L} - N \cos^2 \beta + t_r (0.4571 + 0.5143 \frac{R}{L}) \right\} \quad (73)$$

$$a_1 = \frac{1}{2N} \left\{ 0.05719 - 2N + N \cos^2 \beta + 0.0857 \frac{R}{L} + t_r (0.4571 + 0.5143 \frac{R}{L}) \right\}$$

$$q_1 = -\sin 2\beta$$

$$q_2 = \frac{1}{2N} \left\{ 0.05719 + 0.0857 \frac{R}{L} + N \cos^2 \beta + t_r (0.4571 + 0.5143 \frac{R}{L}) \right\}$$

(continued)

$$q_3 = . . .$$

$$F = \frac{L \cos \beta}{2N} \left[ 0.01667 + 0.05 \frac{R}{L} - t_r \left( 0.0667 + 0.05 \frac{R}{L} \right) \right]$$

(73 cont)

### 3.5 Time-Varying Precession

In Section 4.2 we derived the kinetic energy expression for space-fixed, constant magnitude precessional angular motion of the rotor. In practice, however, time dependent precessional velocities are very possible. In this section we will examine the case when the magnitude of the precessional angular velocity vector is an harmonic time function

$$|\vec{\Omega}| = \Omega \cos \lambda t. \quad (74)$$

Under this condition the angular velocity vector is expressed as

$$\vec{\omega} = \omega i + \Omega \cos \lambda t (\cos \theta j + \sin \theta k) \quad (75)$$

where  $\lambda$  is the frequency of the precession and  $\theta = -\omega t$  as before.

#### 3.5.1 Linear Equation of Motion and the Its Stability

The equation of motion is obtained by the same procedure that

was discussed in Section 4.2 and Section 4.3. Disregarding the nonlinear terms the equation of motion is given

$$\begin{aligned}
 & \frac{d^2 \bar{u}}{d\theta^2} + \left\{ a_0 + \frac{q_2 - 1}{2} \epsilon^2 + \epsilon \frac{q_1}{2} [\cos(1+\nu)\theta + \cos(1-\nu)\theta] \right. \\
 & + \frac{\epsilon^2}{2} \left[ q_2 \cos 2\theta + (q_2 - 1) \cos 2\nu\theta + \frac{q_2}{2} \cos 2(1+\nu)\theta \right. \\
 & \left. \left. + \frac{q_2}{2} \cos 2(1-\nu)\theta \right] \right\} \bar{u} \qquad (76) \\
 & = -\epsilon F \tan \beta [\sin(1+\nu)\theta + \sin(1-\nu)\theta] \\
 & + \epsilon^2 F \left[ \frac{1}{2} \sin 2\theta + \frac{1}{4} \sin 2(1+\nu)\theta + \right. \\
 & \left. \frac{1}{4} \sin 2(1-\nu)\theta \right]
 \end{aligned}$$

where  $\bar{u}$  indicates the tip displacement again. The quantities  $a_0$ ,  $a_1$ ,  $q_1$ ,  $q_2$ , and  $F$  are related to the blade parameters as follows

$$\begin{aligned}
 \theta &= -\omega t \\
 \epsilon &= \frac{\Omega}{\omega} \ll 1 \\
 \nu &= \frac{\lambda}{\omega} \qquad (77)
 \end{aligned}$$

$$\omega_0^2 = \frac{13.42 EI}{mL^3}$$

(continued)

$$q_0 = \frac{\omega_0^2}{\omega^2} - \cos^2 \beta + 1.2619 + 1.617 \frac{R}{L}$$

GENERAL THEORY  
OF POOR QUALITY

$$q_1 = -\sin 2\beta$$

$$q_2 = 0.631 + 0.5 \cos^2 \beta + 0.809 \frac{R}{L}$$

$$F = -L \cos \beta \left( 0.5921 + 0.8011 \frac{R}{L} \right) \quad (77 \text{ cont})$$

The equation of motion (76) represents a forced oscillation whose stability characteristics are determined by its homogeneous solutions. The homogeneous equation can be rewritten in the form

$$\frac{d^2 u}{d\theta^2} + a_0 u = u \cdot f(\theta, \epsilon). \quad (78)$$

Assuming the solution of the above equation to be in the form

$$u = A \cos(\sqrt{a_0} \theta + c), \quad c = \text{constant} \quad (79)$$

equation (78) may be solved by first substituting equation (79) into equation (78). The amplitude in equation (79) is then determined by the equation

$$\begin{aligned} \frac{1}{A} \frac{dA}{d\theta} = \frac{q_1}{8a_0^{1/2}} \epsilon \left( \sin[(2\sqrt{a_0} + 1 + \nu)\theta + 2c] + \sin[(2\sqrt{a_0} - 1 - \nu)\theta + 2c] \right. \\ \left. + \sin[(2\sqrt{a_0} + 1 - \nu)\theta + 2c] + \sin[(2\sqrt{a_0} - 1 + \nu)\theta + 2c] \right) \end{aligned}$$

$$+ \frac{\epsilon^2}{4a_0^{1/2}} (q_2 - 1) \sin [2(\sqrt{a_0} \theta + c)]$$

ORIGINAL PAGE IS  
OF POOR QUALITY

$$+ \frac{\epsilon^2}{8a_0^{1/2}} (q_2 - 1) (\sin [(2\sqrt{a_0} + 2\nu)\theta + 2c] + \sin [(2\sqrt{a_0} - 2\nu)\theta + 2c])$$

$$+ \frac{\epsilon^2}{8a_0^{1/2}} q_2 (\sin [(2\sqrt{a_0} + 2)\theta + 2c] + \sin [(2\sqrt{a_0} - 2)\theta + 2c])$$

$$+ \frac{\epsilon^2}{16a_0^{1/2}} q_2 (\sin [(2\sqrt{a_0} + 2 + 2\nu)\theta + 2c] + \sin [(2\sqrt{a_0} - 2 - 2\nu)\theta + 2c]$$

$$+ \sin [(2\sqrt{a_0} + 2 - 2\nu)\theta + 2c] + \sin [(2\sqrt{a_0} - 2 + 2\nu)\theta + 2c]).$$

(80)

If any term on the right hand side of this equation is not harmonic, the solution amplitude in (79) will be unbounded. This leads to unstable solutions at certain  $a_0$  values. The unstable values are indicated schematically in Fig. 9.

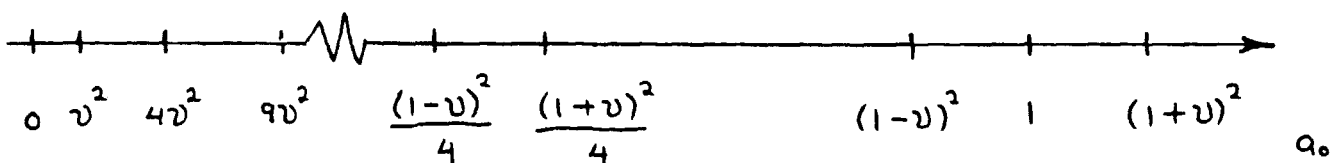


Fig. 9 Schematic Indication of Unstable Values



The general stability of equation (78) can be studied conveniently again by means of the parameter plane  $(a_0, \epsilon)$ . The plane can be divided into regions of stability and instability by the so-called boundary curves or transition curves, separating these regions. The perturbation method is used to derive these stability boundary curves at each of the unstable  $a_0$  values given above. In order to apply the perturbation technique for the determination of stability it is required that the function  $f(\theta, \epsilon)$  in equation (78) be periodic.

The sufficient condition for  $f(\theta, \epsilon)$  to be periodic is that  $\nu$  is a rational number, i.e., obtained by division of two mutually prime integers  $m_1$  and  $m_2$ .

$$\nu = \frac{m_2}{m_1} \tag{81}$$

Under this condition the period of  $f(\theta, \epsilon)$  is  $\pi m_1$  if  $m_1$  and  $m_2$  are both odd. Otherwise the period is  $2\pi m_1$ . Later in this section we will restrict  $m_1$  and  $m_2$  to odd numbers only.

By limiting  $f(\theta, \epsilon)$  to periodic functions Floquet theory for linear differential equations with periodic coefficients is now applicable. Here we use the method of strained parameters again.

The solution of (78) is assumed in the form

$$u = u_0 + \epsilon u_1 + \epsilon^2 u_2 + \dots \tag{82}$$

with the stipulation that the solution  $u$  is periodic with the period of  $f(\theta, \epsilon)$ , whereas the fundamental frequency  $a_0$  is given by

$$a_0 = b_0 + \epsilon b_1 + \epsilon^2 b_2 + \dots \quad (83)$$

Substituting equations (82) and (83) into equation (78) a system of equations is obtained

$$\frac{d^2 u_0}{d\theta^2} + b_0 u_0 = 0$$

$$\frac{d^2 u_1}{d\theta^2} + b_0 u_1 = b_1 u_0 - \frac{1}{2} u_0 q_1 [\cos(1+\nu)\theta + \cos(1-\nu)\theta]$$

$$\begin{aligned} \frac{d^2 u_2}{d\theta^2} + b_0 u_2 = & b_1 u_1 + b_2 u_0 - \frac{1}{2} u_1 q_1 [\cos(1+\nu)\theta + \cos(1-\nu)\theta] \\ & + \frac{1}{2} u_0 [(q_2 - 1) \cos 2\nu\theta + q_2 \cos 2\theta + \frac{1}{2} q_2 \cos 2(1+\nu)\theta \\ & + \frac{1}{2} q_2 \cos 2(1-\nu)\theta] \end{aligned}$$

(84)

Equations (84) are solved recursively. Following the same pattern that was described in Section 3.3 secular terms are eliminated at each step and the equations for stability transition curves are obtained. We give the equations for these curves at  $a_0 = \nu^2$ ,  $a_0 = 1$ ,  $a_0 = \frac{1-\nu}{4}$ , and  $a_0 = \frac{1+\nu}{4}$ .

At  $a_0 = \nu^2$

$$a_0 = \nu^2 + \left[ -\frac{q_2 - 1}{2} + \frac{q_1^2 (3\nu^2 - 1)}{4(\nu^2 - 1)(9\nu^2 - 1)} \right] \epsilon^2 - \left[ \frac{q_1^2}{8(1 - \nu^2)} + \frac{q_2 - 1}{4} \right] \epsilon^2$$

$$a_0 = \nu^2 + \left[ -\frac{q_2 - 1}{2} + \frac{q_1^2 (3\nu^2 - 1)}{4(\nu^2 - 1)(9\nu^2 - 1)} \right] \epsilon^2 + \left[ \frac{q_1^2}{8(1 - \nu^2)} + \frac{q_2 - 1}{4} \right] \epsilon^2 \quad (85)$$

At  $q_0 = 1$

$$q_0 = 1 + \left[ -\frac{q_2 - 1}{2} + \frac{q_1^2}{4} \frac{(3 - v^2)}{(1 - v^2)(9 - v^2)} \right] \epsilon^2 + \left[ \frac{q_1^2}{8(1 - v^2)} - \frac{q_2}{4} \right] \epsilon^2$$

$$q_0 = 1 + \left[ -\frac{q_2 - 1}{2} + \frac{q_1^2}{4} \frac{(3 - v^2)}{(1 - v^2)(9 - v^2)} \right] \epsilon^2 - \left[ \frac{q_1^2}{8(1 - v^2)} - \frac{q_2}{4} \right] \epsilon^2 \quad (86)$$

At  $q_0 = \frac{1 - v}{4}$

$$q_0 = \frac{1 - v}{4} + \epsilon \frac{q_1}{4} \quad (87)$$

At  $q_0 = \frac{1 + v}{4}$

$$q_0 = \frac{1 + v}{4} + \epsilon \frac{q_1}{4} \quad (88)$$

Other transition curves are obtained accordingly.

### 3.6 The Effect of Damping

So far we have not considered damping in the analysis. In reality blade motion is damped by external and internal dissipative forces. Air resistance is a typical form of external damping and internal damping may be due to dissipative stresses in the blade which is called material damping.

The dependence of dissipative forces on blade motion is quite complicated. In this section we shall study a simple model in which damping force is proportional to the velocity. Introducing

a damping force  $2 \frac{c}{\omega} \frac{d\bar{u}}{d\theta}$  into the linear equation of motion  
 (17) the equation becomes

$$\frac{d^2 \bar{u}}{d\theta^2} + 2 \frac{c}{\omega} \frac{d\bar{u}}{d\theta} + [a_0 + \epsilon^2 a_1 + \epsilon q_1 \cos \theta + \epsilon^2 q_2 \cos 2\theta] \bar{u} = 0 \quad (89)$$

The constant  $c$  in the above equation represents the viscous damping factor.

In order to study the stability of the motion governed by equation (89) the equation is reduced to a Hill's type of equation through the transformation

$$\bar{u}(\theta) = e^{-\frac{c}{\omega} \theta} u(\theta) \quad (90)$$

under which

$$\frac{d^2 u}{d\theta^2} + [a_0 - \frac{c^2}{\omega^2} + \epsilon^2 a_1 + \epsilon q_1 \cos \theta + \epsilon^2 q_2 \cos 2\theta] u = 0 \quad (91)$$

From the results of section 4.3.2 it can be inferred that the solution to equation (91) is singular at  $a_0 - \frac{c^2}{\omega^2} = 1/4$  and  $a_0 - \frac{c^2}{\omega^2} = 1$ . In other words, the singular points on the  $a_0$  axis of  $(a_0, \epsilon)$  plane for the undamped case are shifted to the left. In general  $c^2$  is a very small quantity so that the singular points may be assumed approximately coincident with those of the undamped system. Since the other parameters in the differential equation (91) are the same as those of the undamped system of equation (17) the stability transition curves will have the same form.

In the unstable regions the solution to equation (91) has the following form

$$u(\theta) = e^{\mu\theta} \bar{\Phi}(\theta) \quad (92)$$

where  $\bar{\Phi}(\theta + 2\pi) = \bar{\Phi}(\theta)$ , i.e.  $\bar{\Phi}$  is a periodic function of  $\theta$ . The coefficient  $\mu$  governs the growth rate of the solution  $u$  in the unstable regions and therefore sometimes it is termed the "negative damping coefficient". In the following steps we will obtain  $\mu$  in terms of the parameters in the differential equation (91).

Inserting the assumed solution (92) into the differential equation (91) we obtain a differential equation in terms of the periodic function

$$\frac{d^2 \bar{\Phi}}{d\theta^2} + 2\mu \frac{d\bar{\Phi}}{d\theta} + [a_0 - \frac{c^2}{\omega^2} + \mu^2 + \epsilon^2 a_1 + \epsilon q_1 \cos \theta + \epsilon^2 q_2 \cos 2\theta] \bar{\Phi} = 0 \quad (93)$$

Following Whittaker's perturbation method that is given in reference (7) we expand the solution and the parameters of equation (93) in terms of  $\epsilon$  as follows

$$\begin{aligned} \bar{\Phi} &= \phi_0 + \epsilon \phi_1 + \epsilon^2 \phi_2 \\ a_0 - \frac{c^2}{\omega^2} &= b_0 + \epsilon b_1 + \epsilon^2 b_2 \\ \mu &= \epsilon \mu_1 + \epsilon^2 \mu_2 \end{aligned} \quad (94)$$

Substituting the above expansion forms into equation (93) and rearranging in powers of  $\epsilon$  we obtain

$$\phi_0'' + b_0 \phi_0 = 0$$

$$\phi_1'' + b_0 \phi_1 = -2\mu_1 \phi_0' - b_1 \phi_0 - q_1 \cos \theta \phi_0$$

$$\phi_2'' + b_0 \phi_2 = -2\mu_2 \phi_0' - 2\mu_1 \phi_1' - b_1 \phi_1$$

$$- (b_2 + \mu_1^2 + a_1) \phi_0 - q_1 \cos \theta \phi_1 - q_2 \cos 2\theta \phi_0$$

(95)

Equations (95) should be solved in the neighborhood of the singular points mentioned before, namely  $a_0 - \frac{c^2}{\omega^2} = \frac{1}{4}$  and  $a_0 - \frac{c^2}{\omega^2} = 1$ . The resulting secular terms are eliminated in each power of  $\epsilon$  so that periodicity of  $\Phi$  is maintained at each step. At  $a_0 - \frac{c^2}{\omega^2} = \frac{1}{4}$  we obtain the following conditions for eliminating secular terms in  $\phi_1$ ,

$$b_1 = \mp \sqrt{\frac{q_1^2}{4} - \mu_1^2} \quad (96)$$

$$\frac{A_0}{B_0} = \frac{1}{\mu_1} \left[ -\frac{q_1}{2} \mp \sqrt{\frac{q_1^2}{4} - \mu_1^2} \right] \quad (97)$$

where  $A_0, B_0$  are the solution constants of  $\phi_0$ . Equation (96) represents a relation between  $b_1$  and  $\mu_1$  which can be used to express  $\mu_1$  in terms of the other parameters. A better approximation is obtained by eliminating secular terms in  $\phi_2$ . This requires that

$$\mathcal{M}_2 \frac{-\sqrt{\frac{q_1^2}{4} - b_1^2}}{-(b_1 + \frac{q_1}{2})} = b_2 + \mathcal{M}_1^2 + a_1 + \frac{q_1^2}{8} \quad (98)$$

$$\mathcal{M}_2 \frac{-\sqrt{\frac{q_1^2}{4} - b_1^2}}{-(b_1 - \frac{q_1}{2})} = b_2 + \mathcal{M}_1^2 + a_1 + \frac{q_1^2}{8} \quad (99)$$

from which it can be shown that

$$\mathcal{M}_2 = 0 \quad (100)$$

and

$$b_2 = -\mathcal{M}_1^2 - a_1 - \frac{q_1^2}{8} \quad (101)$$

In equations (100), (101), and (96) the frequency expansion parameters  $b_i$  are related to the negative damping parameters  $\mathcal{M}_i$  in the neighborhood of  $a_0 = 1/4$ . We will give the expression for a constant  $\mathcal{M}$  curve in the unstable region near  $a_0 = 1/4$ . From equation (94)

$$\mathcal{M}_1 = \frac{\mathcal{M}}{\epsilon} \quad (102)$$

and

$$a_0 - \frac{c^2}{\omega^2} = \frac{1}{4} + \epsilon b_1 + \epsilon^2 b_2 \quad (103)$$

Inserting equation (102) into eq. (101) and eq. (96) and then by substitution into equation (103) we get the expression for a  $\mu =$  constant curve in the  $(a_0, \epsilon)$  plane.

$$a_0 - \frac{\mu^2}{\omega^2} = \frac{1}{4} + \sqrt{\frac{q_1^2}{4} \epsilon^2 - \mu^2} - \epsilon^2 \left( a_1 + \frac{q_1^2}{8} \right) - \mu^2 \quad (104)$$

By finding the extrema of the above expression it can easily be shown that the lowest value of  $\epsilon$  is

$$\epsilon_{\min} = \frac{2\mu}{q_1} \quad (105)$$

This equation can be used to determine the lowest  $\epsilon$  value that will cause instability when damping is present in the system.

The analysis is repeated in the neighborhood of  $a_0 = 1$  to obtain the negative damping curves that correspond to a  $\mu =$  constant value. In the first power of  $\epsilon$  it is determined that

$$\begin{aligned} \mu_1 &= 0 \\ b_1 &= 0 \end{aligned} \quad (106)$$

and in the second power of  $\epsilon$ ,

$$b_2 = \frac{q_1^2}{6} - a_1 + \frac{1}{2} \sqrt{\left( q_2 - \frac{q_1^2}{2} \right) - 16\mu_2^2} \quad (107)$$

Equation (96) takes the following form

$$a_0 - \frac{\epsilon^2}{\omega^2} = 1 + \epsilon^2 b_2 \quad (108)$$



$$\mu_2 = \frac{\mu}{\epsilon^2} \quad (109)$$

Inserting equation (109) into (107) and in turn substituting into equation (108) we obtain the negative damping curve that corresponds to  $\mu = \text{constant}$  curve in  $(a_0, \epsilon)$  plane in the neighborhood of  $a_0 = 1$

$$a_0 - \frac{c^2}{\omega^2} = 1 + \epsilon \left( \frac{q_1^2}{6} - a_1 \right) \mp \frac{1}{2} \sqrt{\epsilon^4 \left( q_2 - \frac{q_1^2}{2} \right)^2 - 16\mu^2} \quad (110)$$

The minimum value of  $\epsilon$  on this curve is

$$\epsilon_{\min}^2 = \frac{8\mu}{2q_2 - q_1^2} \quad (111)$$

It should be noted that the negative damping coefficient in the neighborhood of  $a_0 = 1$  is in the order of  $\epsilon^2$  whereas that of  $a_0 = 1/4$  is in the order of  $\epsilon$ . Hence the growth rate is slower in the unstable region near  $a_0 = 1$ . It can be expected that the growth rate at other singular points will be successively smaller.

So far we have analyzed the growth rate of  $u$  that was defined by equation (90). The next step is to link the growth rate of  $u$  to that of  $\bar{u}$  which is the solution to the equation of motion (89) for

blade vibrations when damping is present. It must be noted that this dissipative damping has no relation to the negative damping that was mentioned before.

Equations (92) and (90) can be combined to give

$$\bar{u}(\theta) = e^{(1-\frac{c}{\omega})\theta} \bar{\Phi}(\theta) \quad (112)$$

where  $\bar{\Phi}$  is periodic. From this equation we clearly see the criteria for stability of damped blade vibrations. The vibrations with damping will grow in time if the negative damping coefficient associated with parametric excitation is larger than the dissipative damping coefficient of the system.

$$\frac{c}{\omega} > \mu \quad \text{for stability} \quad (113)$$

The stability transition curves of equation of motion (89) are obtained by setting

$$\frac{c}{\omega} = \mu \quad (114)$$

Inserting equation (114) into the negative damping curves (110) and (104) the stability transition curves for the differential equation of (89) are obtained.

$$a_0 = \frac{1}{4} \mp \sqrt{\frac{q_1^2}{4} \epsilon^2 - \frac{c^2}{\omega^2}} - \epsilon^2 \left( a_1 + \frac{q_1^2}{8} \right) \quad (115)$$

$$a_0 = 1 + \frac{c^2}{\omega^2} + \epsilon^2 \left( \frac{q_1^2}{6} - a_1 \right) \mp \frac{1}{2} \sqrt{\epsilon^4 \left( q_2 - \frac{q_1^2}{2} \right)^2 - 16 \frac{c^2}{\omega^2}} \quad (116)$$

ORIGINAL PAGE OF  
OF POOR QUALITY

ORIGINAL PAGE IS  
OF POOR QUALITY

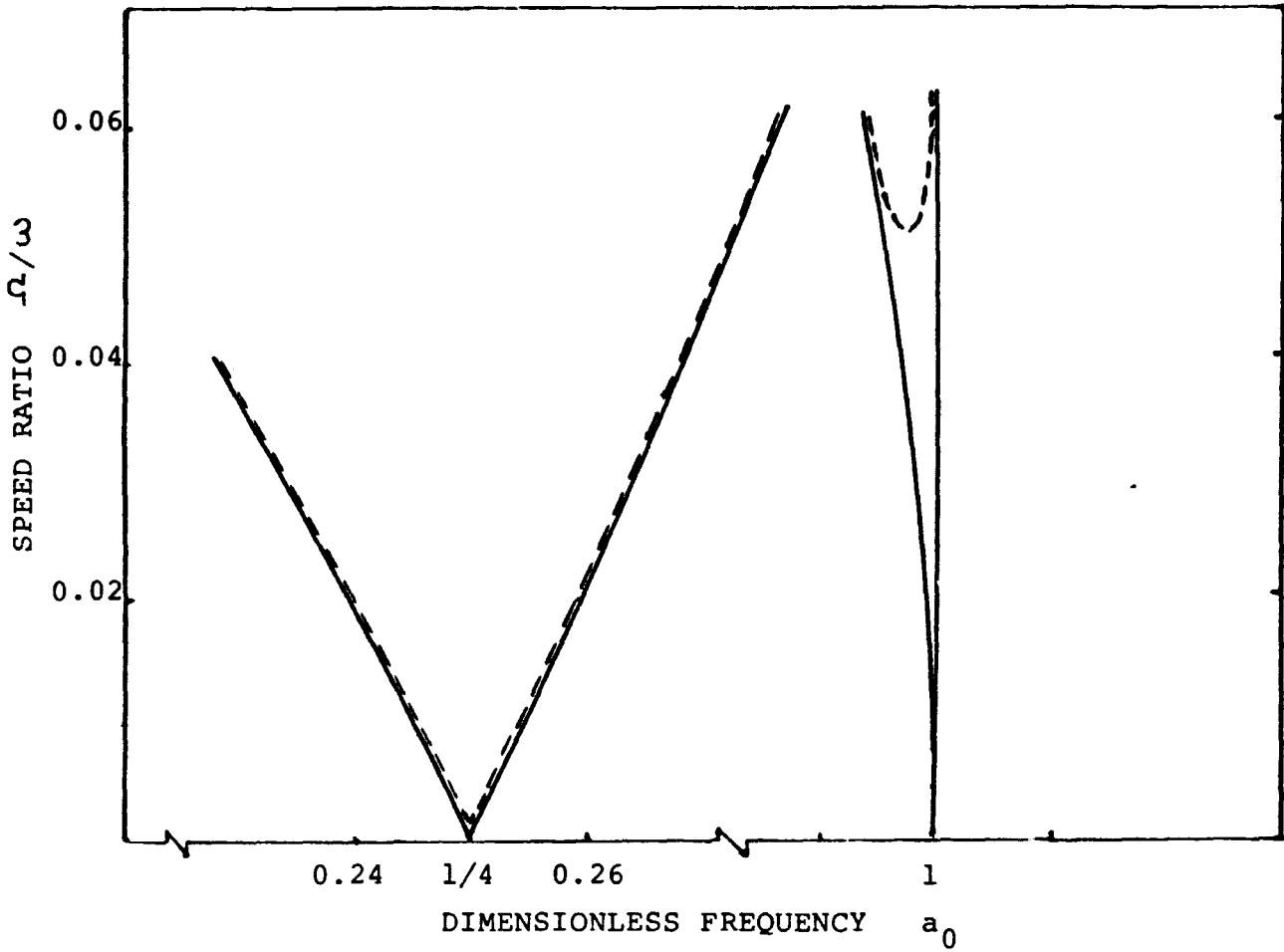


Fig. 10 Stability Chart for Damped Vibrations

These equations for transition curves could be obtained by directly applying Whittaker's method to equation (89) and searching for periodic solutions.

Equations (115) and (116) are plotted in Fig. 10 for a particular blade data that yields  $a_1 = 1$ ,  $q_1 = 1$ , and  $q_2 = 2$ . The stability transition curves that correspond to a particular damping factor,  $c/\omega = 10^{-3}$ , are compared to the undamped case. If  $\omega$  is 5000 RPM  $c/\omega = 10^{-3}$  corresponds to a viscous damping factor,  $c = 0.5$ . As  $c$  becomes smaller the transition curves in Fig. 10 approach the curves for the undamped case.

From Fig. 10 it can be seen that a finite damping coefficient causes blade instability to occur at lower precessional rates. For a particular damping factor the range of safe precessional speeds can be determined from equations (111) and (105) when negative damping coefficient  $\mu$  is set equal to the damping factor,  $c/\omega$ . Hence we obtain

$$\Omega_s = \frac{2c}{q_1} \quad \text{at} \quad q_0 = \frac{1}{4} \quad (117)$$

and

$$\Omega_s^2 = \frac{8c\omega}{(2q_2 - q_1^2)} \quad \text{at} \quad q_0 = 1 \quad (118)$$

where  $\Omega_s$  represents the safe precessional speed. From these equations and Fig. 10 it can be inferred that higher precessional

rates are required at  $a_0 = 1$  for instability as compared to  
 $a_0 = 1/4$ . For the particular example ( $c = 0.5$ ) the safe range  
of precession in terms of  $\epsilon = \Omega/\omega$  are  $\epsilon_s = 0.002$   
at  $a_0 = 1/4$  and  $\epsilon_s = 0.051$  at  $a_0 = 1$ .

## 4. Arbitrary Blades Under Combined Rotor Spin and Space-Fixed Precession

### 4.1 Introduction

The stability analysis performed in section 3 are based upon an assumed blade deformation shape (see equation 3.13) which might be different from the actual shape that would occur. Another deficiency of the approach used in the last section is that pretwisted blades can not be analyzed in the same fashion. In this section a general numerical formulation to analyze the stability of a pretwisted blade of arbitrary cross-section is presented. Results obtained by this method are compared with those computed in section 3. In addition the behavior of a turbomachinery blade with realistic dimensions is studied. The same approach may be used to analyze forced vibrations of a pretwisted blade under gyroscopic excitation.

The first step is to derive a stiffness matrix for the twisted blade. In order to handle blades with arbitrary geometry, finite element approach is selected. For a twisted blade usually the shell element is the most appropriate finite element. However, the numerical method for dealing with the stability problem is quite complicated. It is desirable not to employ too many degrees of freedom for the modeling of the blade. For this reason the beam element is chosen. Since the problem interested in this work happens almost exclusively to long and slender blades this simplification is not considered serious. A  $12 \times 12$  beam element stiffness matrix for twisted blades is formulated based on a theory proposed by Downs (10). Static deflection solutions are used to study the accuracy

of this stiffness matrix.

The derivations for mass matrix and the changes in stiffness matrix due to rotational motions are based on Lagrange's formulation of equations of motion. Before the equations of motion with time dependent coefficients are analyzed the natural frequencies in both rotating and non-rotating force fields are calculated. The computed solutions are compared with known analytical and experimental results. The subsequent stability analysis of the pretwisted blade under both rotor spin and space-fixed precession is studied via numerical methods based on Floquet's theory.

#### 4.2 Stiffness Matrix

The elementary beam theory cannot be directly applied to the study of twisted blade. The modified beam theory assumes that the undeformed blade is pretwisted along its length about a straight longitudinal axis through shear centers of cross sections. These cross sections are parallel to the rotor fixed xy plane (see Fig. 3.1). The blade surface is supposed to be composed of helical fibers. If the position of an arbitrary point on the cross section is indicated by its principal coordinates  $\xi$  and  $\eta$ , the distance of this point from the shear center is

$$d = (\xi^2 + \eta^2)^{1/2} \quad (1)$$

By designating  $\alpha$  as the initial twist of the blade in radians per unit length and considering a portion of the blade with unit length, any helical fiber of length  $l_H$  which is at a distance  $d$





from the shear center forms a small spiral angle  $\gamma$  (see Fig. 1) with the longitudinal axis. The length of this helical fiber can be approximated as

$$l_H = (1 + \alpha^2 d^2)^{1/2} \quad (2)$$

Knowing this length, the axial strain of a helical fiber due to bending, axial load and torsion can be derived. The axial filament strain caused by an extension of "a" per unit length is

$$\epsilon_a = \frac{[(1+a)^2 + \alpha^2 d^2]^{1/2} - [1 + \alpha^2 d^2]^{1/2}}{[1 + \alpha^2 d^2]^{1/2}} \quad (3)$$

Neglecting higher order terms in  $\alpha$  this equation may be reduced to

$$\epsilon_a = a \left(1 - \frac{1}{2} \alpha^2 d^2\right) \quad (4)$$

The axial strain due to an elastic twist  $\bar{\phi}$  per unit length can be given in a similar manner

$$\epsilon_{\bar{\phi}} = \frac{[1 + (\alpha + \bar{\phi})^2 d^2]^{1/2} - [1 + \alpha^2 d^2]^{1/2}}{[1 + \alpha^2 d^2]^{1/2}} \quad (5)$$

Again ignoring higher order terms in  $\bar{\phi}$  and  $\alpha$

$$\epsilon_{\bar{\phi}} = \bar{\phi} \alpha d^2 \left(1 - \frac{1}{2} \alpha^2 d^2\right) \quad (6)$$

The total axial strain from axial extension, bending and torsion can be derived

$$\epsilon = (1 - \frac{1}{2}\alpha^2 d^2) \left[ \frac{dw}{dz} - \xi^* \frac{d^2 u_\xi}{dz^2} - \eta^* \frac{d^2 u_\eta}{dz^2} + \frac{d\phi}{dz} \alpha d^2 \right] \quad (7)$$

where  $\xi^* = \xi - e_x, \eta^* = \eta - e_y$  ( $e_x, e_y$  are positions of the centroid) and where  $u_\xi$  and  $u_\eta$  are the deformations in the principal directions.

The stiffness matrix is obtained from the potential energy of a beam element

$$U = \frac{1}{2} \int \sigma^T \epsilon dv \quad (8)$$

where  $\epsilon$  is the deformation strain and  $\sigma$  its corresponding stress. Substituting the axial strain given by equation (7) into the strain energy expression (8) the stiffness matrix is determined after performing the integration. Since torsional strain was not included in the strain equation (7), torsional rigidity has to be added to the final stiffness matrix. It is worth noting that other effects such as shear deformation, warping and rotary initial terms can be included in the strain expression (7) if they are considered important. The integrand in equation (8) may be written in matrix form

$$\begin{aligned} \sigma^T \epsilon = & E (1 - \frac{1}{2}\alpha^2 d^2)^2 \begin{Bmatrix} \frac{dw}{dz} \\ \frac{d^2 u_\xi}{dz^2} \\ \frac{d^2 u_\eta}{dz^2} \\ \frac{d\phi}{dz} \end{Bmatrix}^T \begin{bmatrix} 1 & -\xi^* & -\eta^* & \alpha d^2 \\ -\xi^* & \xi^{*2} & \xi^* \eta^* & -\xi^* \alpha d^2 \\ -\eta^* & \xi^* \eta^* & \eta^{*2} & -\eta^* \alpha d^2 \\ \alpha d^2 & -\xi^* \alpha d^2 & -\eta^* \alpha d^2 & \alpha^2 d^4 \end{bmatrix} \begin{Bmatrix} \frac{dw}{dz} \\ \frac{d^2 u_\xi}{dz^2} \\ \frac{d^2 u_\eta}{dz^2} \\ \frac{d\phi}{dz} \end{Bmatrix} \quad (9) \\ & = E (1 - \frac{1}{2}\alpha^2 d^2)^2 \{ D_2 u \}^T [P] \{ D_2 u \} \end{aligned}$$

ORIGINAL PAGE IS  
OF POOR QUALITY

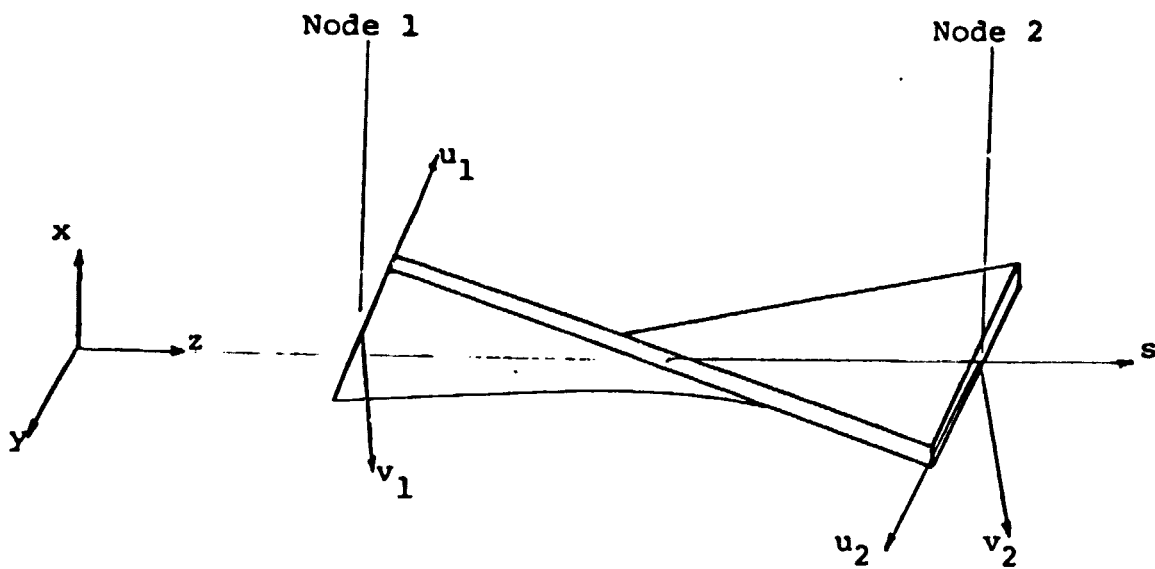


Fig.3 Principal Nodal Displacements in Bending

For the finite element formulation the deformations within an element  $\{Du\}$  have to be expressed in terms of nodal displacements. This is accomplished by assuming reasonable distributions for the element deformations between end nodes and relating these deformations to nodal displacements by shape functions. Element bending deformations  $u_\xi$  and  $u_\eta$  in equation (9) are in the principal directions of the cross sections and hence they rotate with the pretwist angle along the longitudinal axis. This will lead to complicated finite element shape functions. In order to keep the shape functions simple the principal displacements  $\bar{u}$  and  $\bar{v}$  at the middle of the blade element are selected to represent the element bending deformations. They are related to bending displacements of an arbitrary cross section by (see Fig. 3)

$$\begin{aligned} u_\xi &= \bar{u} \cos \alpha s + \bar{v} \sin \alpha s \\ u_\eta &= -\bar{u} \sin \alpha s + \bar{v} \cos \alpha s \end{aligned} \quad (10)$$

The coordinate  $s$  originates from the middle of an element. It coincides with the longitudinal  $z$  axis and they have the following relationship

$$s = z - R - \sum_{i=1}^{n-1} l_i - \frac{l}{2}, \quad |s| < \frac{l}{2} \quad (11)$$

where  $n$  is the number of the element and  $l_i$  represents the length of each element. The length of the  $n$ th element under consideration is  $l$ .  $R$  is the rotor radius.

All the displacements are approximated by polynomials

$$\begin{aligned}
 \omega &= C_1 s + C_2 \\
 \bar{u} &= C_3 + C_4 s + C_5 s^2 + C_6 s^3 \\
 \bar{v} &= C_7 + C_8 s + C_9 s^2 + C_{10} s^3 \\
 \phi &= C_{11} s + C_{12}
 \end{aligned}
 \tag{12}$$

The constants  $C_i$  are determined by the nodal displacement variables at the two end nodes (1 and 2)

$$\{u_i\}^T = \{\omega_1, \phi_{x1}, u_1, \phi_{y1}, v_1, \phi_1, \omega_2, \phi_{x2}, u_2, \phi_{y2}, v_2, \phi_2\}
 \tag{13}$$

The expressions of  $C_i$  are listed in Appendix A.

The deformation variables  $\{D_{\frac{1}{2}}u\}$  used in equation (9) can now be expressed in terms of nodal displacement variables  $\{u_i\}$ . The bending curvatures in  $\{D_{\frac{1}{2}}u\}$  are related to curvatures in the middle of the element.

$$\begin{aligned}
 \frac{d^2 u_{\xi}}{ds^2} &= \frac{d^2 \bar{u}}{ds^2} \cos \alpha s + \frac{d^2 \bar{v}}{ds^2} \sin \alpha s \\
 \frac{d^2 u_{\eta}}{ds^2} &= -\frac{d^2 \bar{u}}{ds^2} \sin \alpha s + \frac{d^2 \bar{v}}{ds^2} \cos \alpha s
 \end{aligned}
 \tag{14}$$

Differentiating equation (12) with respect to  $s$  the following equations are obtained

ORIGINAL PAGE IS  
OF POOR QUALITY

$$\frac{dw}{ds} = C_1$$

$$\frac{d\bar{u}}{ds} = C_4 + 2C_5s + 3C_6s^2$$

$$\frac{d^2\bar{u}}{ds^2} = 2C_5 + 6C_6s$$

$$\frac{d\bar{v}}{ds} = C_8 + 2C_9s + 3C_{10}s^2$$

(15)

The constants  $C_i$  are known in terms of nodal displacement variables  $\{u_i\}$ . They are substituted into equation (15), and with equation (14) the transformation matrix between deformation variables and nodal displacement variables  $\{D_u\}$  is obtained

$$\begin{Bmatrix} \frac{dw}{ds} \\ \frac{d^2u_x}{ds^2} \\ \frac{d^2u_y}{ds^2} \\ \frac{d\phi}{ds} \end{Bmatrix} = \begin{bmatrix} T_{1,1} & . & . & . & T_{1,12} \\ T_{2,1} & . & . & . & . \\ T_{3,1} & . & . & . & . \\ T_{4,1} & . & . & . & T_{12,12} \end{bmatrix} \begin{Bmatrix} w_1 \\ \frac{du_x}{ds} \Big|_1 \\ u_1 \\ \frac{du_y}{ds} \Big|_1 \\ v_1 \\ \phi_1 \\ w_2 \\ \frac{du_x}{ds} \Big|_2 \\ u_2 \\ \frac{du_y}{ds} \Big|_2 \\ v_2 \\ \phi_2 \end{Bmatrix} \quad (16)$$

or  $\{D_u\} = [T_i] \{u_i\}$

The elements of transformation matrix  $[T_i]$  are given in Appendix B.

Inserting equation (16) into equation (9) and after performing the matrix algebra the potential energy is

$$U = \frac{1}{2} \{u_i\}^T \int_V [s] dv \{u_i\} \quad (17)$$

where the matrix [S] is

$$[s] = E(1 - \nu^2 d^2) [T_i]^T [P] [T_i] \quad (18)$$

From the potential energy equation (17) the stiffness matrix is derived

$$[K] = \int_V [s] dv \quad (19)$$

To extend this integration for the stiffness matrix to a relatively complicated cross section of the type which is liable to occur in real turbomachinery blades requires the introduction of a method known as the isoparametric transformation in the finite element analysis (11). With this approach the evaluation of the stiffness matrix represented by equation (19) can include cross sections of any arbitrary form. This involves the distortion of a simple basic square form into areas with arbitrary boundary shapes. The accuracy of the 'mapping' depends on the number of nodes introduced around the circumference. In this report all results are based on eight boundary nodes.

In the standard isoparametric formulation of three dimensional distortion, mapping takes place in all three directions. In the present approach, the integral (19) of the stiffness matrix already contain the blade pretwist effect. Therefore, it suffices to perform distortion in two dimensions of the blade cross-sectional area only. This reduces the amount of required numerical computation in evaluating the stiffness matrix. It also assumes that the axis of pretwist is a straight line.

The isoparametric formulation begins with the establishment of a one-to-one correspondence between the Cartesian and curvilinear coordinates. The variables  $\xi$  and  $\eta$  in matrix [P] of equation (18) are related to the curvilinear coordinates x and y

$$\begin{Bmatrix} \xi \\ \eta \end{Bmatrix} = f \begin{Bmatrix} x \\ y \end{Bmatrix} \quad (20)$$

Once such coordinate relationships are known, shape functions can be specified in local undistorted coordinates and by suitable transformations the stiffness matrix evaluated.

The most convenient way of establishing the coordinates relationship in (20) is to use the shape functions  $N_i$  associated with the eight boundary nodes. This may be written as

$$\begin{aligned} \xi &= N_1 \xi_1 + N_2 \xi_2 + \dots + N_8 \xi_8 \\ \eta &= N_1 \eta_1 + N_2 \eta_2 + \dots + N_8 \eta_8 \end{aligned} \quad (21)$$



in which  $N_i$  are shape functions given in terms of the local coordinates  $(x,y)$ . Based on the basic square form the shape function expressions are

Corner nodes

$$N_i = \frac{1}{4} (1 + xx_i)(1 + yy_i)(xx_i + yy_i - 1) \quad (22)$$

Mid-side nodes

$$\begin{aligned} x_i = 0, \quad N_i &= \frac{1}{2} (1 - x^2)(1 + y^2 y_i^2) \\ y_i = 0, \quad N_i &= \frac{1}{2} (1 + xx_i)(1 - y^2) \end{aligned} \quad (23)$$

where  $i$  is the number of the shape function, and  $x_i, y_i$  are either +1 or -1 or zero depending on the location of the boundary node.

To evaluate the stiffness matrix in equation (19) two transformations are necessary. In the first place  $\xi$  and  $\eta$  are defined in terms of local (curvilinear) coordinates  $x, y$  by equation (21). In the second place the volume over which the integration has to be carried out needs to be expressed in terms of the local coordinates. A standard process will be used which involves the determinant of the Jacobian matrix  $[J]$ . Thus

$$d\xi d\eta ds = \det [J] dx dy ds \quad (24)$$

The Jacobian matrix  $[J]$  is found explicitly in terms of the local coordinates by

$$[J] = \begin{bmatrix} \frac{dN_1}{dx} & \frac{dN_2}{dx} & \dots & \frac{dN_s}{dx} \\ \frac{dN_1}{dy} & \frac{dN_2}{dy} & \dots & \frac{dN_s}{dy} \end{bmatrix} \begin{bmatrix} \xi_1 & \eta_1 \\ \xi_2 & \eta_2 \\ \vdots & \vdots \\ \xi_s & \eta_s \end{bmatrix} \quad (25)$$

After substituting equations (21) and (24) into the integral expression for the stiffness matrix (19) the stiffness matrix of an arbitrary cross-section is

$$[K] = \int_V [s'] \det [J] dx dy ds \quad (26)$$

The above integration must be evaluated numerically. A flow-chart showing how to compute this 12 x 12 matrix using Gaussian integration is given in Appendix C.

In order to establish the accuracy of this numerical method the static deflections of cantilever beams with arbitrary cross-section were investigated. For different elliptical and triangular cross-sections the errors in computed free end deflections using this approach with six elements remained below 3% of the theoretical values. This seems adequate for most engineering applications. In particular for the stability analysis of interest in this work the accuracy of the approximated stiffness matrix is sufficient.

Another interesting example selected to evaluate the numerical accuracy in computing the stiffness matrix is the cross-section defined by a convex and a concave edge and shaped like a crescent (see Fig. 2). Two nodal distribution schemes were tested. They

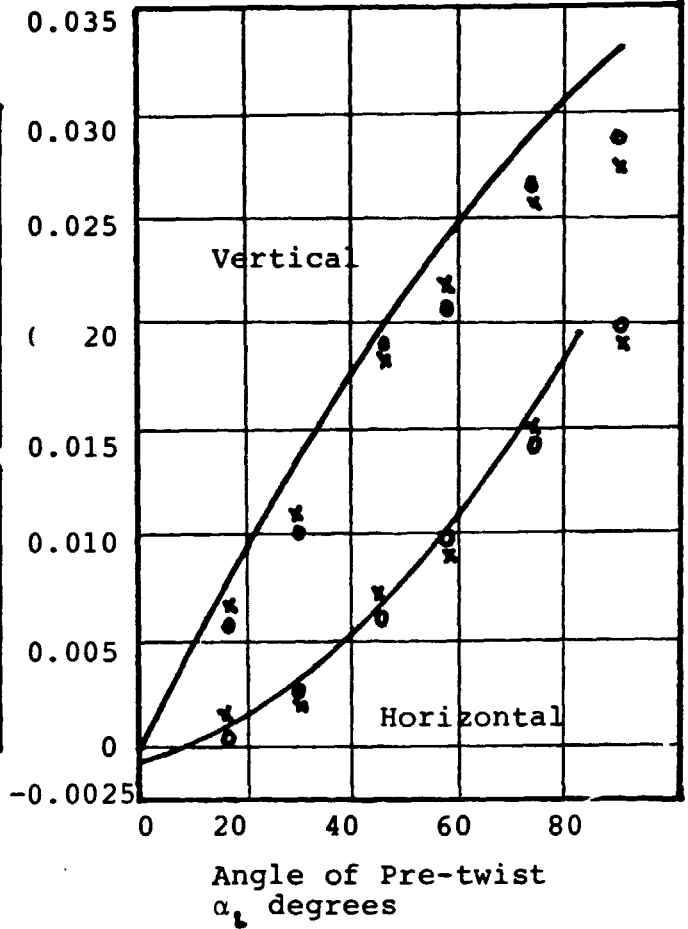
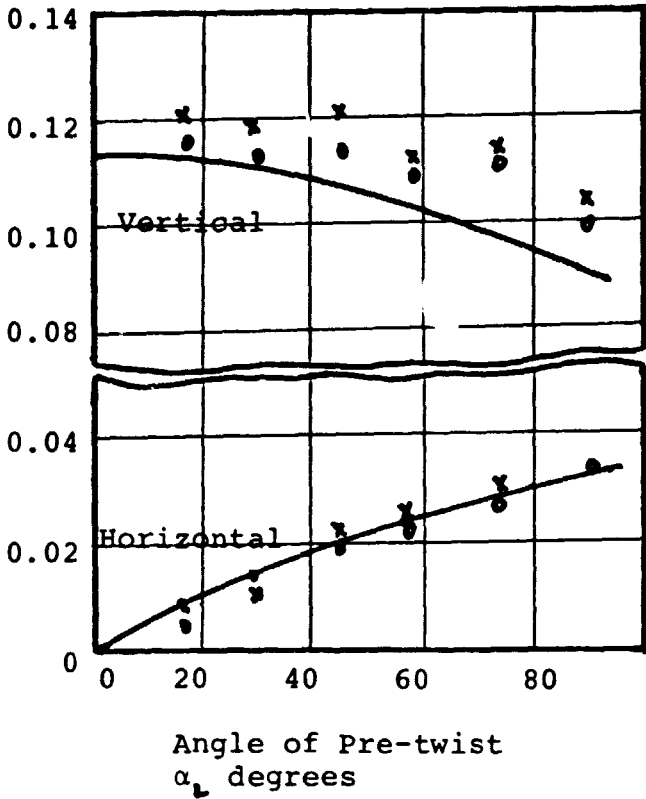
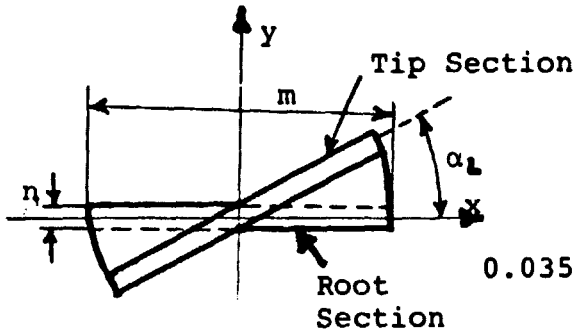
are shown in Fig. 2a and 2b. For a 6 inch long cantilever beam with 3000 lb. load at the free end the vertical and horizontal free end deflections are compared with those obtained by the numerical method (six elements):

	x-direction	y-direction
Scheme A	.5296	.0841
Scheme B	.5890	.0898
Beam Solution	.5608	.0877

This indicates that the eight nodes in case b are better placed than the ones in case a. The numerical interpolation is quite sensitive. If three nodal points are employed along the circular edge only, the results can be as much as 100% off the correct values. This is due to the fact that the three node parabolic approximation cannot represent the circular edge correctly.

For twisted blade with rectangular cross section some experimental results were presented by W. Carnegie (12). In these experiments the blades were uniformly pretwisted over a 6 inch (15.2 cm) length and had cross sectional dimensions of 1 in x 1/16 in. (2.54 cm x 0.16 cm). The blade material was mild steel with density of  $\rho = .000735 \text{ lbf-sec}^2/\text{in}^4$  and with Young's modulus of  $E = 30 \times 10^6$  psi. Using the same blade data and six finite elements the static deflection under unit load at the tip was computed. The results are compared to Carnegie's experimental results in Fig. 4. As can be seen deflections in the horizontal and vertical directions become

ORIGINAL PART IS  
OF POOR QUALITY



x = Microscopic                      o = Dial gauges                      — = Present Solution

a. Load Applied Vertically

b. Load Applied Horizontally

Figure 4: Static Deflections of Rectangular Cross-Section Blades  
Subjected to Concentrated Loading. ( 6 Elements )

due to pretwist. Satisfactory agreement is obtained in these comparisons.

### 4.3 Kinetic Energy and Mass Matrix

The mass matrix is derived from the kinetic energy which also determines the changes in the stiffness matrix due to rotational motions. For the case of space fixed precession these changes in stiffness matrix are time dependent and might lead to instability of the system. Without precessional angular velocity usually the primary interest is in the calculation of natural frequencies. After deriving the kinetic energy and the associated matrices, the correctness of these matrices will be tested by comparing the computed natural frequencies in rotating and non-rotating force fields with known experimental and analytical solutions.

Beginning with the displacement vector  $\vec{r}$  of an arbitrary point  $(x, y, z)$  of the beam

$$\begin{aligned} \vec{r} = & (x + u - y\phi)\vec{i} + (y + v + x\phi)\vec{j} \\ & + (z + w + \phi\alpha(x^2 + y^2) - \frac{1}{2} \int_R^z [(\frac{\partial u}{\partial z})^2 + (\frac{\partial v}{\partial z})^2] dz \\ & - \frac{1}{2} (x^2 + y^2) \int_R^z (\frac{\partial \phi}{\partial z})^2 dz)\vec{k} \end{aligned} \quad (27)$$

The  $x, y, z$  coordinates employed in this displacement equation are the rotor-fixed coordinates shown in Fig. 3.1. The corresponding velocity is

$$\begin{aligned} \vec{v} = & (\dot{u} - y\dot{\phi})i + (\dot{v} + x\dot{\phi})j \\ & + (\dot{\omega} + \dot{\phi}\alpha(x^2 + y^2) - \int_r^z \left[ \frac{\partial u}{\partial z} \cdot \frac{\partial \dot{u}}{\partial z} + \frac{\partial v}{\partial z} \cdot \frac{\partial \dot{v}}{\partial z} \right] dz \\ & - (x^2 + y^2) \int_r^z \frac{\partial \dot{\phi}}{\partial z} \cdot \frac{\partial \dot{\phi}}{\partial z} dz) k + \vec{\omega} \times \vec{r} \end{aligned} \quad (28)$$

where  $\vec{\omega}$  is the angular velocity of the rotor and was defined in equation (3.1) of section 3. The velocity  $\vec{v}$  is to be inserted into the kinetic energy

$$T = \frac{1}{2} \rho \int_V \vec{v} \cdot \vec{v} dV \quad (29)$$

For the finite element analysis, the deformation variables

$$\{u_F\}^T = \left\{ u, v, \omega, \phi, \frac{\partial u}{\partial z}, \frac{\partial v}{\partial z}, \frac{\partial \phi}{\partial z} \right\}$$

in the velocity  $\vec{v}$  equation (28) have to be expressed in terms of nodal displacement variables  $\{u_i\}$  employed in the stiffness matrix (19). Due to the angle between the major principal bending axis of a cross section and the rotor spin axis the deformation variables  $\{u_F\}$  can be related to deformation variables  $\{u_A\}$  at an arbitrary cross section

$$\begin{Bmatrix} u \\ v \\ \omega \\ \phi \\ \frac{\partial u}{\partial z} \\ \frac{\partial v}{\partial z} \\ \frac{\partial \phi}{\partial z} \end{Bmatrix} = \begin{bmatrix} \cos\beta & -\sin\beta & 0 & 0 & 0 & 0 & 0 \\ \sin\beta & \cos\beta & 0 & 0 & 0 & 0 & 0 \\ 0 & 0 & 1 & 0 & 0 & 0 & 0 \\ 0 & 0 & 0 & 1 & 0 & 0 & 0 \\ 0 & 0 & 0 & 0 & \cos\beta & -\sin\beta & 0 \\ 0 & 0 & 0 & 0 & \sin\beta & \cos\beta & 0 \\ 0 & 0 & 0 & 0 & 0 & 0 & 1 \end{bmatrix} \begin{Bmatrix} u_A \\ u_B \\ \omega \\ \phi \\ \frac{\partial u_A}{\partial z} \\ \frac{\partial u_B}{\partial z} \\ \frac{\partial \phi}{\partial z} \end{Bmatrix} \quad (30)$$

ORIGINAL PAGE IS  
OF POOR QUALITY

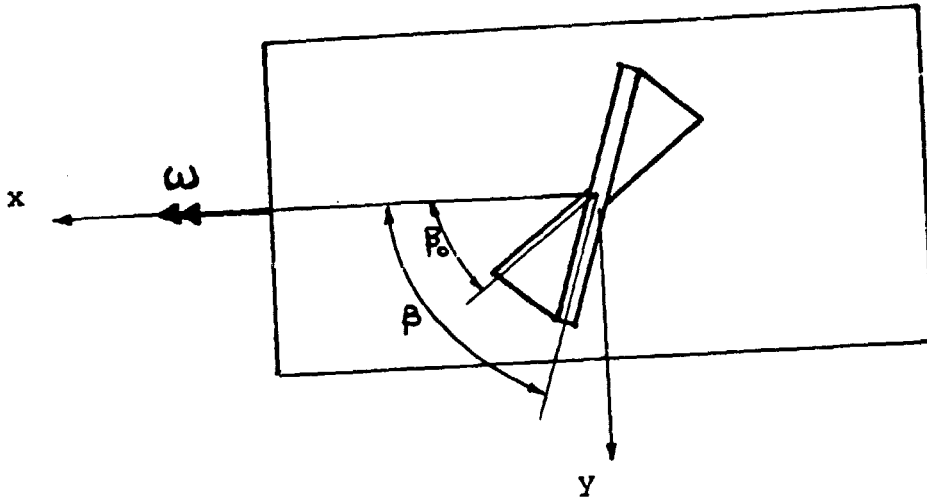


Fig.5 Setting Angle and Global Displacements

$$\text{or } \{u_F\} = [T_2] \{u_A\}$$

where the angle  $\beta$  is between the rotor spin axis and the major principal bending axis of an arbitrary cross section. If the pretwist angle per unit length  $\alpha$  is constant the angle  $\beta$  is (see Fig. 5)

$$\beta = \beta_0 + \alpha z \quad (31)$$

with  $\beta_0$  as the blade setting angle at the root.

To be consistent with the shape functions employed in the derivation of the stiffness matrix the principal displacements  $\vec{u}$  and  $\vec{v}$  at the middle of an element are selected to represent the element bending deformations. The angle of twist of the nth element middle cross section is

$$\beta_m = \beta_0 + \sum_{i=1}^{n-1} \alpha_i l_i + \frac{1}{2} \alpha_n l_n \quad (32)$$

where  $\alpha_i$  and  $l_i$  are the pretwist rate and length of elements before the nth element. With  $\beta = \beta_m$  in equation (30) the deformation variables  $\{u_F\}$  are functions of

$$\{u_m\}^T = \left\{ \vec{u}, \vec{v}, w, \phi, \frac{\partial \vec{u}}{\partial z}, \frac{\partial \vec{v}}{\partial z}, \frac{\partial \phi}{\partial z} \right\} \quad (33)$$

Repeating the procedure used to derive equation (16) for the stiffness matrix the above variables can be determined in terms of nodal variables  $\{u_i\}$



$$\{u_m\} = [T_3] \{u_i\} \quad (34)$$

The elements of matrix  $[T_3]$  are listed in Appendix D. With  $\{u_n\} = \{u_m\}$  in equation (30) and  $\{u_m\}$  from equation (34) the variables in the velocity  $\vec{v}$  equation (28) are expressed as functions of the nodal variables  $\{u_i\}$ . Substituting this velocity into the kinetic energy (29), this leads to the kinetic energy of an element

$$T = \frac{1}{2} \rho \int \left[ \{\dot{u}_i\} [M_1] \{\dot{u}_i\} + \{u_i\} [M_2] \{u_i\} + \{\dot{u}_i\} [M_3] \{u_i\} + \{M_4\}^T \{\dot{u}_i\} + \{M_5\}^T \{u_i\} \right] dV \quad (35)$$

where  $\{u_i\}$  are the nodal displacement variables and  $\{\dot{u}_i\}$  their time derivatives. The matrices  $[M_i]$  are

$$\begin{aligned} [M_1] &= [T_3]^T [T_2]^T [A_1] [T_2] [T_3] \\ [M_2] &= [T_3]^T [T_2]^T [A_2] [T_2] [T_3] \\ [M_3] &= [T_3]^T [T_2]^T [A_3] [T_2] [T_3] \\ \{M_4\} &= [T_3]^T [T_2]^T \{A_4\} [T_2] [T_3] \\ \{M_5\} &= [T_3]^T [T_2]^T \{A_5\} [T_2] [T_3] \end{aligned} \quad (36)$$

The matrices  $[A_i]$  are listed in Appendix E.

With both kinetic and potential energies the equations of motion can be derived via Lagrange's formulation. The mass matrix is obtained after integrating matrix  $[M_1]$ . This mass matrix is not exactly the same as the standard mass matrix because of the pretwist effect. The differences are, however, very minor. The elements of matrix  $[M_2]$  are time dependent. They reflect the effects of both rotational and precessional motions on the beam stiffness. This matrix is combined with the stiffness matrix of equation (26) to form a time dependent matrix representing the spring stiffness coefficient matrix of the equations of motion. Matrix  $[M_3]$  does not appear in the equations of motion. The forcing terms of the equations of motion are obtained from matrices  $\{M_4\}$  and  $\{M_5\}$ . The integrations in equation (35) are performed numerically. For arbitrary cross-sections the same numerical distortion procedure used in the evaluation of stiffness matrix has to be applied.

Without the precessional angular velocity the integrated matrix  $[M_2]$  represents the change of blade stiffness due to rotor spin. To demonstrate the accuracy of the present approach the following numerical example was calculated: length,  $l = 7$  in., width,  $w = 3$  in., thickness,  $t = 0.09$  in., Young's modulus,  $E = 1 \times 10^7$  psi, Poisson's ratio,  $\nu = 0.3$ , and mass density,  $\rho = 2.587 \times 10^{-4}$  lbm/in<sup>3</sup>. The results are presented in Figs. 5 and 6 and are compared with the experimental and numerical results obtained by MacBain (13) using NASTRAN program and 230 plate elements. The present numerical results, based upon the beam theory, are obtained using 6 beam elements. In Fig. 6, the first, second and

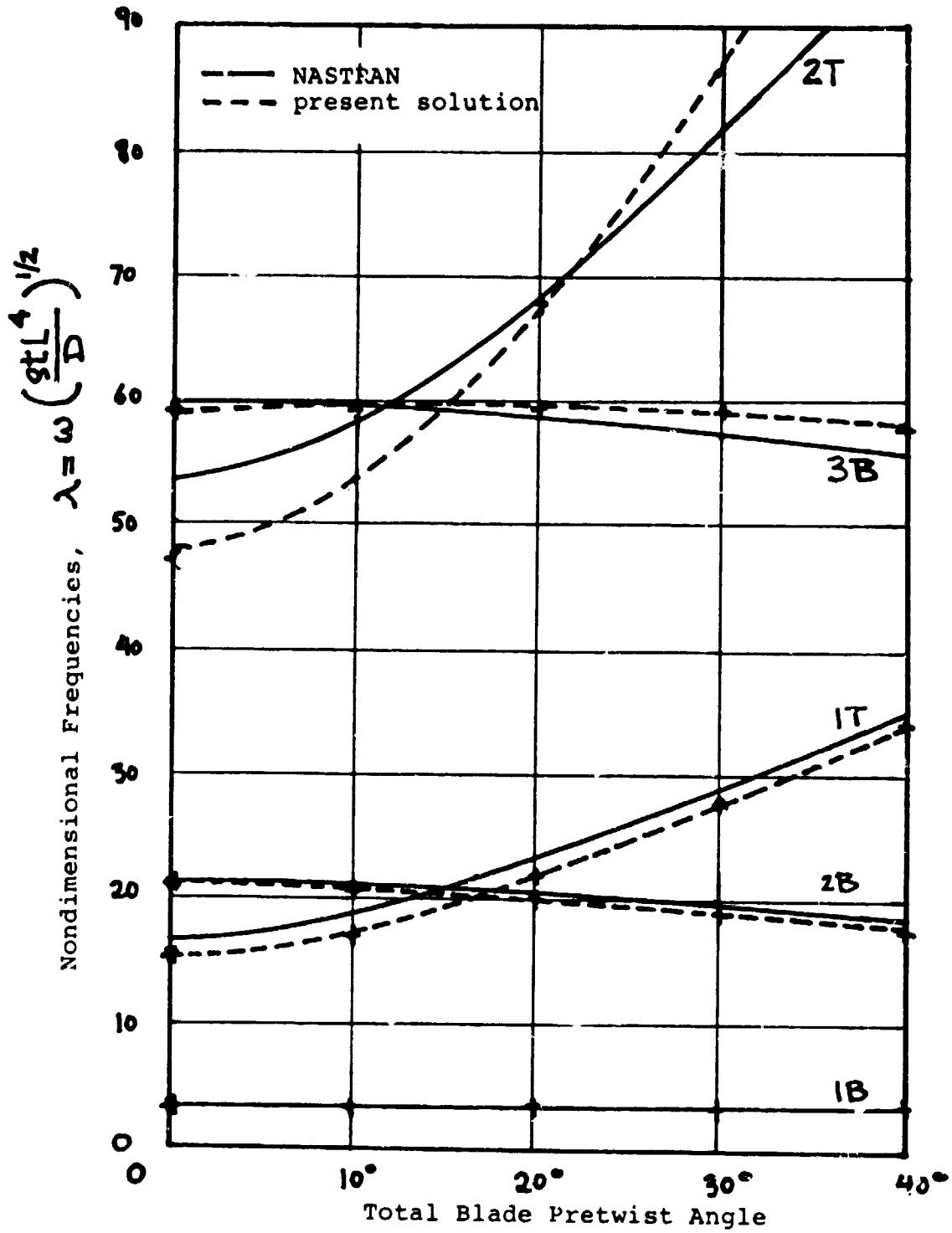


Fig. 6 Natural Frequencies vs Pretwist Angle

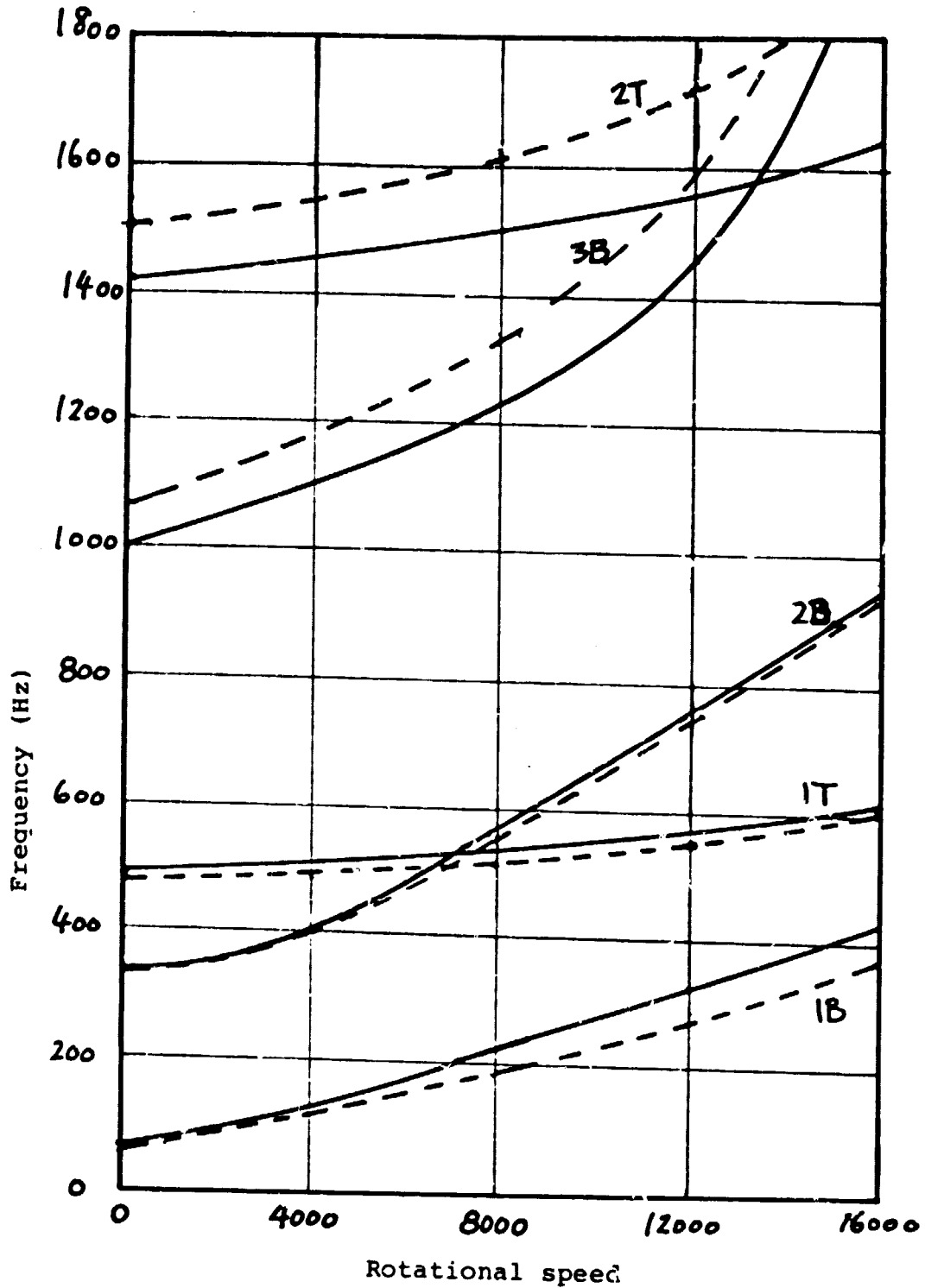


Fig. 7 Natural frequency vs rotational speed  
(30 deg pretwist angle)

third bending frequencies and the first and second torsional frequencies at zero spin velocity are plotted vs. the total pretwist angle of the blade. In Fig. 7, the same frequencies with  $30^\circ$  deg pretwist angle are plotted vs. the rotational speed. In this case the blade setting angle  $\beta_0 = 0$  and hub radius  $R = 7$  in.

The same examples were used by Chen and Dugundji (14) to show the accuracy of a twisted beam finite element derived from the governing differential equations of motion provided by Houbolt and Brooks (15). Since the theoretical assumptions made by Houbolt and Brooks are essentially the same as those made in this report there is practically no difference in the numerical solutions. Comparing the derivation of stiffness and mass matrices for the finite element analysis the present approach is superior because of its straight-forward simplicity. Nonlinear material or geometrical effects can be easily included in the derivation. The evaluation of cross sectional properties are based on the shape of the area and not its moment of inertia which is often difficult to determine.

#### 4.4 Stability Analysis

The homogenous equations of motion for the study of stability due to precessional motion can be formulated as a system of linear differential equations with periodic coefficients. The system has the following form

$$[M_1] \{\ddot{u}\} + [K^*] \{u\} = 0 \quad (37)$$

$[M_1]$  is the mass matrix defined by equation (36).  $[K^*]$  is the effective stiffness matrix which is the combination of the structural stiffness matrix  $[K]$  defined in equation (26) and the  $[M_2]$  matrix given by equation (36). The periodicity enters equation (37) through the matrix,  $[M_2]$ , whose time dependent terms are due to the precessional motion.

A vast array of literature exists on the subject of ordinary differential equations with periodic coefficients. Some of them are procedures to study the stability problem. After reviewing these procedures, it was determined that most of them are not suitable for systems with many degrees of freedom such as equation (37). For large systems a general method of solution proposed by Friedman (16) was found to be most appropriate. The details of the method are not presented in this report because the procedure in reference (16) was adapted here without any major revision. Following the suggested procedure and employing the improved numerical integration scheme based on the Runge-Kutta method a computer program was developed to study the stability regions of the equations of motion governed by the matrix equation (37).

The first problem studied was the straight beam with constant cross section. This case was already analyzed using another method in section 3.3.2. The results were plotted in a stability chart in Fig. 3 of section 3. The linearized finite element solutions based on equation (37) with one and two elements were able to duplicate the same stability chart. This demonstrates that the basic approach employed in the finite element solution is correct.

Furthermore, since the stability chart is now obtained by two different solution methods, there is much more confidence in the validity of this chart.

The next case studied was the pretwisted beam with constant cross section. The stability chart for this case is basically very similar to the stability chart of the beam without pretwist. The effect of beam pretwist is to increase the structural stiffness in the effective stiffness matrix  $[K^*]$  of equation (37). This leads to an increase of the parameter  $a_0$  of the stability chart in Fig. 3 of section 3 depending on the amount of pretwist. Since the regions of instability decrease with increasing values of  $a_0$ , the pretwisted beam is less prone to unstable dynamic motion under precessional rotations.

The computation for each point in the stability chart using the finite element solution is very expensive and time consuming. Not enough stable or unstable points were calculated to chart a complete stability diagram.

## 5. Forced Vibration and Flutter

### 5.1 Introduction

The complete time dependent problem under precessional rotation solved by the finite element method can be reduced to a system of ordinary differential equations of the characteristic form

$$[m_1] \{\ddot{u}\} + [K^*] \{u\} = \{F\} \quad (38)$$

in which  $[M_1]$  and  $[K^*]$  are assembled mass and effective stiffness matrices. The force matrix  $\{F\}$  is obtained from matrices  $\{M_4\}$  and  $\{M_5\}$  defined in equation (36). In general, the above equations are non-linear; only linear cases will be studied. The forcing matrix  $\{F\}$  contains functions of first and second order in spin velocity; hence it is periodic. In the following the forced vibration problem will be solved by the determination of periodic responses to equation (38).

The availability of the twisted beam finite element program and a subroutine for unsteady subsonic aerodynamics (17) made possible a short study of "fan flutter" under realistic conditions of structural coupling due to twist. The effect of centrifugal forces on the flutter mode is taken into account as well. The terms associated with precessional rotation were removed. The equations of motion to study flutter have the following form

$$[m_1] \{\ddot{u}\} + [C] \{\dot{u}\} + [K^*] \{u\} = 0 \quad (39)$$



Matrix [C] represents aerodynamic damping and contains complex terms. Substituting

$$\{u\} = \{\bar{u}\} e^{\alpha t} \quad (40)$$

into equation (39) the characteristic equation is obtained

$$\left( \alpha^2 [M_1] + \alpha [C] + [K^*] \right) \{\bar{u}\} = 0 \quad (41)$$

where  $\alpha$  and  $\{\bar{u}\}$  are complex. The real part of the solution represents a decaying vibration. The complex eigenvalue problem involved in Eq. (41) is solved by a numerical procedure given in reference (18).

## 5.2 Forced Vibration

In section 3.3.6 the forced vibration of the simplified single degree of freedom system was studied. It was shown that dynamic responses are not sensitive to time dependent quantities in the stiffness term. It seems reasonable to remove time dependent quantities from the effective stiffness matrix [K\*] and reduce the coefficients of the differential equations (38) to constants.

The forcing term in Eq. (38) is periodic. It can be expressed as

$$\{F\} = \{\bar{F}\} e^{\alpha t} \quad (42)$$

where  $\alpha$  is complex. A general solution can be given as

$$\{u\} = \{\bar{u}\} e^{\alpha t} \quad (43)$$

Substituting (43) in Eq. (38) gives

$$\left( \alpha^2 [M_1] + [K^*] \right) \{ \bar{u} \} = \{ \bar{F} \} \quad (44)$$

By inverting the matrix

$$[D] = \alpha^2 [M_1] + [K^*] \quad (45)$$

and pre-multiplying with the force amplitude  $\{ \bar{F} \}$  the dynamic response  $\{ \bar{u} \}$  can be determined.

The first computational example selected for comparison is the straight beam without pretwist. Using a model with one finite element the same tip displacement responses were reproduced as those given in Fig. 7 and 8 of section 3. A few pretwisted beams were studied as well. In general, the peak displacements are smaller for pretwisted beam.

### 5.3 Flutter

The computational model chosen for examination is a steel cantilever rotor blade uniformly twisted from root to tip such that the stagger angle varies from 30 degrees at the attachment to 60 degrees at the free end. The blade is untapered and the cross section is taken to be a thin rectangle of 5.08 cm chord and 4% thickness ratio. Pitch/chord ratio at midradius is 0.878. The hub/tip radius ratio is 0.5. Axial inflow is assumed, uniform radially, such that the relative flow angle at the blade tip is 60 degrees. This specification determines the air velocity triangle at every radius; the aerodynamics are computed at the mean radius

of each beam (blade) element using the formulation outlined in [17].

The method of solution of the equations of motion was essentially the same as that described in reference [18], and known as the "p-k method". For a given Mach number, a value of reduced frequency,  $k$ , is assumed, the unsteady aerodynamic forces are computed using the aforementioned subroutine. The equations are then solved for the complex eigenvalues,  $\omega = \omega_R + i \omega_I$ . The motion having been assumed to have a time dependence described by  $\exp(i\omega t)$ , the computed value of  $\omega_R$  provided an improved estimate of the reduced frequency,  $k = \omega_R C / (2V)$  and the procedure can be iterated until  $\omega_R$  does not change. The converged value of  $\omega_R$  gives an estimate of the flutter frequency; the associated value of  $\omega_I$  at convergence is an indication of the nonaerodynamic forms of damping (positive or negative) that must be supplied to maintain the constant amplitude "flutter" condition. In the absence of such external damping, the flutter condition occurs with  $\omega_I = 0$ ; thus  $\omega_I < 0$  indicates instability, or potentially divergent motion.

In the previous series of calculations the interblade phase angle is a parameter. In practice this is limited to a finite number of possible values  $2\pi n/N$  where  $N$  is the number of blades in the row and  $n$  is any integer,  $0 < n \leq N$ . For the extraction of the greatest amount of information it is convenient to let the interblade phase angle range continuously over  $0, 2\pi$ . Thus, at each Mach number, a closed contour is obtained in  $\omega_R, \omega_I$  coordinates with interblade phase angle as a parameter.

The true flutter condition occurs at that Mach number where a closed loop is obtained, lying entirely in the positive  $\omega_I$  region

expect for one point at which the contour is tangent to the  $\omega_R$  axis.

Figures 4-1, 4-2, and 4-3 show the contours obtained for the model blade at absolute approach Mach numbers of 0.75, 0.85 and 0.95. It appears from these figures that flutter will occur at a Mach number just below 0.85 with an interblade phase angle in the neighborhood of  $100^\circ$ .

In each of the figures a cusp-like tangency or near tangency of the contour occurs in the neighborhood of  $\omega_R = 1023$  to  $1253$  rad/sec, depending on the relative Mach number, and hence rotor speed. These points, and the irregular nature of the curves near these tangencies, are attributable to the "aerodynamic resonance" phenomenon. At the combination of parameters which produce aerodynamic resonance the unsteady aerodynamic loading on the blades vanishes [18] and the blades vibrate as if in a vacuum. Thus, the computed eigenvalue is real and corresponds to the rotating natural frequency in vacuo. Although the aerodynamic damping does not go negative, operation at this point could result in large response to forcing and may be shown in some instances to lead to the accumulation of fatigue damage.

True flutter of the coalescent type is illustrated in Fig. 4-3. Here a slight amount of mechanical damping would produce a flutter point at  $\omega_R \cong 2330$  and  $\psi \cong 100^\circ$ . The mode shape represents a combination of the modes associated with the two lowest eigenfrequencies at  $\omega_R = 1138$  and  $\omega_R = 3296$ .

One concludes from this brief study, and other supplementary data, that the structural coupling introduced by blade twist results, at least in these fairly representative cases, in a classical "coalescence-type" flutter.

ORIGINAL PAGE IS  
OF POOR QUALITY

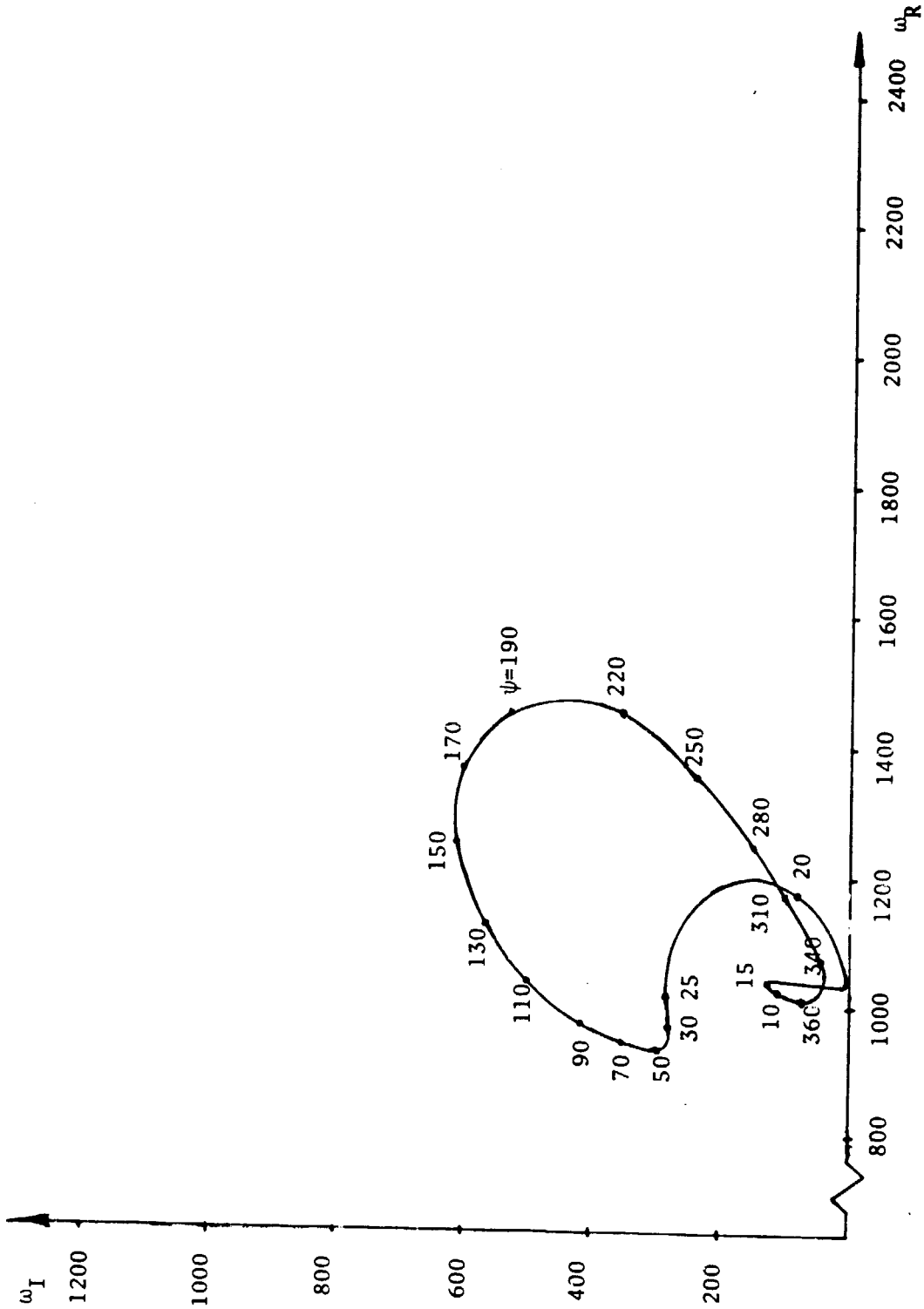


Fig. 4-1 Lowest Mode Eigenvalues for 0.75 Approach Mach Number

ORIGINAL PAGE IS  
OF POOR QUALITY

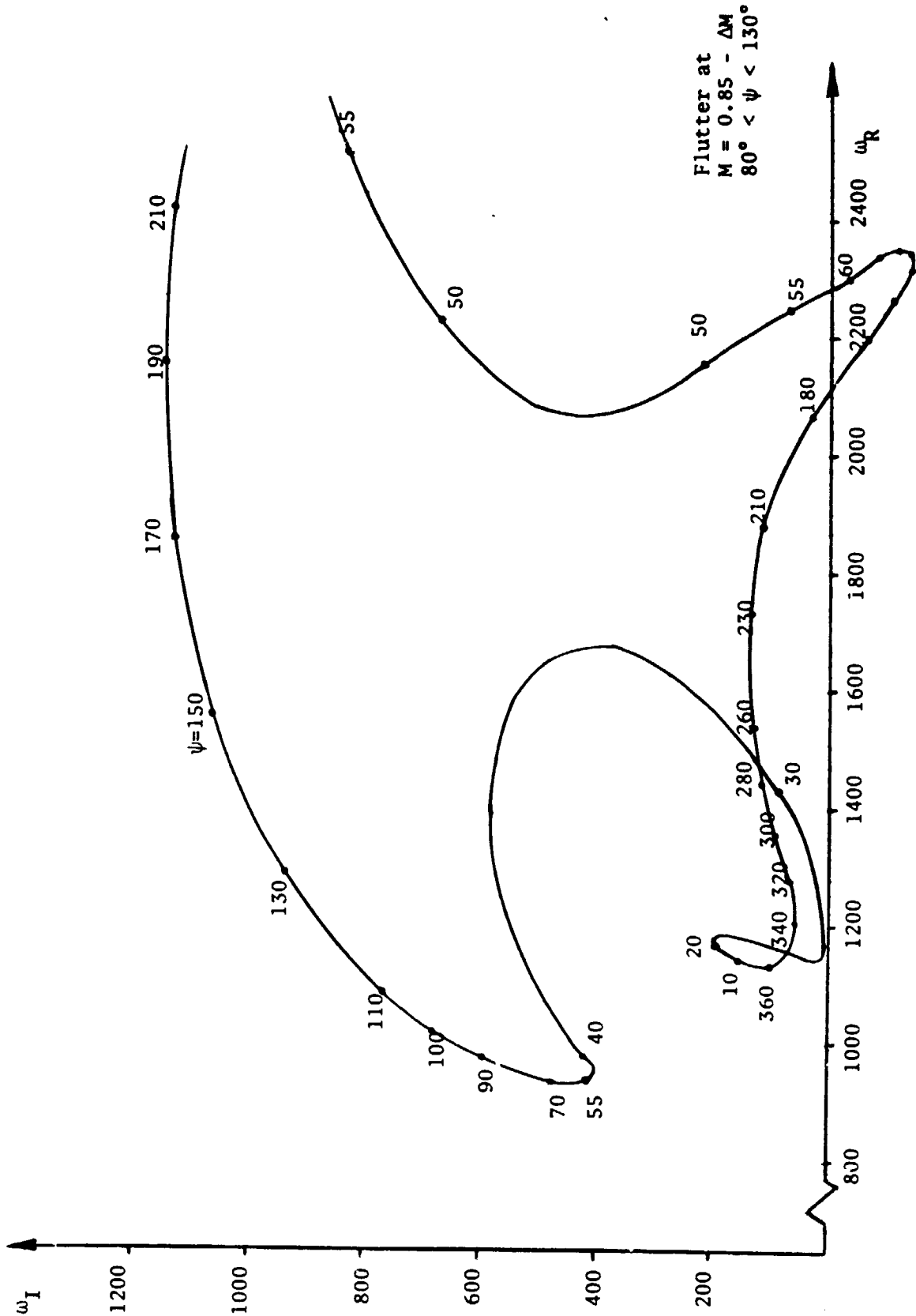


Fig. 4-2 Eigenvalues for Coalescing of Two Lowest Modes for  
0.85 Approach Mach Number

ORIGINAL PAGE IS  
OF POOR QUALITY

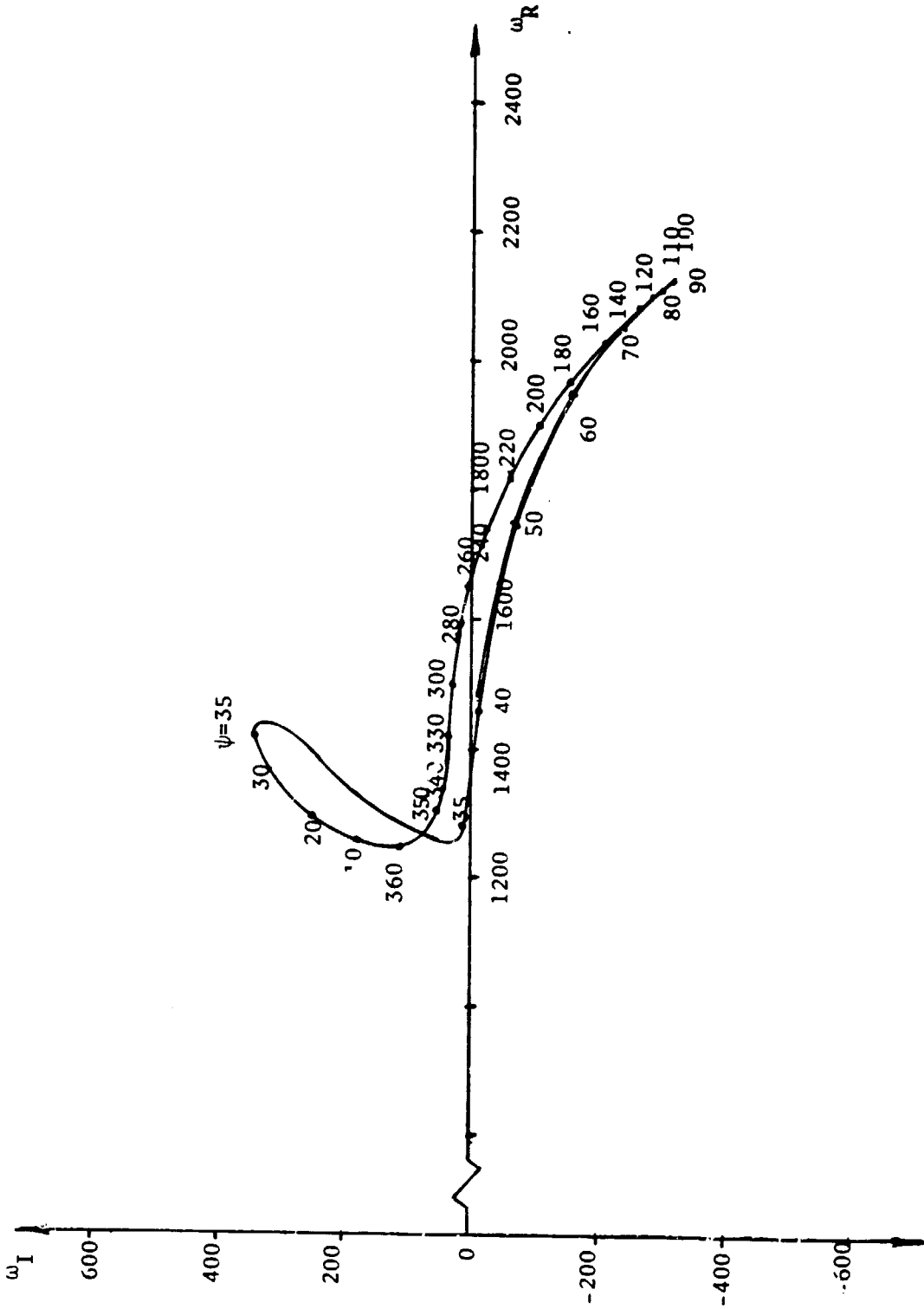


Fig. 4-3 Lowest Eigenvalues for 0.95 Approach Mach Number

## 6. Conclusions

The 3 year program of research supported by NASA and reported herein has resulted in four papers listed as references 1,2,3 and 5. Additionally, an interim technical report listed as reference 16, was issued after completion of the first half of the contract period and has been incorporated into the present report.

Analytical representations coupled with computer-based numerical solutions have been completed for a number of significant blade dynamics problems. The earliest of these are point mass and uniform cantilever models. A beam-type finite element, displaying the important foreshortening property, has been developed and forms the structural basis for all of the later programs. Blade twist, taper and cross-sectional shape are accounted for.

• Stability of a blade on a spinning and precessing rotor has been studied using this beam element. Both steady (ramp function) precessional displacement and harmonic precession have been studied and instability has been shown to be possible in both operational modes. The critical parameters discriminating unstable motion are found to be dependent primarily on the ratios of rotating natural frequency to spin frequency and of constant\* precession rate to spin frequency. The blade setting angle and ratio of blade length to attachment radius are also of significance. With harmonic precession the critical values of spin rate are found to be dependent upon the frequency of the harmonic variation of the precessional motion.

---

\* In the case of harmonic precession the maximum rate (or amplitude) replaces the constant of the steady precession case.



• Forced vibrations, outside the regions of instability and excited at three basic frequencies (a subharmonic, the spin frequency and twice the spin frequency) are attributable to the interaction of precession and spin and may be calculated in a straightforward manner.

• Blades (beams) modeled as pretwisted beam-type finite elements were subjected to subsonic cascade flutter analysis. It was demonstrated that it is important to take into account the structural coupling due to pretwist and to properly model the effect of the rotational field on the rotor blade mode shape.

The general conclusions of greatest importance are:

- 1) the rotor blade model for dynamic analysis in complex rotational fields and in air aerodynamic environment should properly reflect foreshortening and pretwist for reliable predictive capability, and
- 2) thin blades, on the order of 5% tip thickness, should properly be analyzed using a plate-type finite element incorporating foreshortening (as yet unformulated) and with arbitrary orientation in the force field due to arbitrary rotational motion (spin plus precession).
- 3) Twisted cantilever rotor blades at subsonic speeds tend to flutter in the coalescent mode in which the two gravest mode couple to produce the negative aerodynamic damping. This result is interesting since it is at odds with some of the theoretical predictions for untwisted blades.

## 7. Acknowledgement

The authors are grateful to L. James Kiraly and Robert Kielb of NASA-Lewis Laboratory who acted as Technical Officers during the course of this work.

. References

1. Sisto, F., Chang, A.T., "The Influence of Gyroscopic Forces on the Dynamic Behavior of Rotating Blades", The Fifth International Symposium on Airbreathing Engines, Feb. 16-21, 1981, Bangalore, India.
2. Sisto, F., Chang, A.T., and Sutcu, M., "Blade Excitation due to Gyroscopic Forces", IFTOMM Conference on Rotordynamic Problems in Power Plants, Sept. 27th-Oct. 3rd, 1982, Rome, Italy.
3. Sisto, F., Chang, A.T., and Sutcu, M., "The Influence of Coriolis Forces on Gyroscopic Motion of Spinning Blades", 27th International Gas Turbine Conference and Exhibit, London, England, April 18-22, 1982.
4. Vigneron, F.R., "Comment on Mathematical Modeling of Spinning Elastic Bodies for Modal Analysis", AIAA Journal, Vol. 13, No. 1, January 1975, pp. 126-127.
5. Sisto, F. and Chang, A.T., "A Refined Finite Element for Vibration Analysis of Twisted Blades Based on Beam Theory," Paper No. AIAA-83-0917-CP, 24th Structures, Structural Dynamics and Materials Conference, L. Tahoe, Nevada, May 1983.
6. Stoker, J.J., Nonlinear Vibrations, Interscience Publishers, New York, 1950, pp. 202-208.
7. Nayfeh, A.H., "The Mathieu Equation", Introduction to Perturbation Techniques, First Edition, John Wiley & Sons, 1981, pp. 235-249.
8. Magnus, W., Winkler, S., "Basic Concepts", Hill's Equation, Dover Edition, Dover, 1979, pp. 7-8.
9. Bogoliubov, N.N., Mitropolsky, Y.A., "Influence of External Periodic Forces", Asymptotic Methods in the Theory of Nonlinear Oscillations, Gordon and Breach Science Publishers, New York, 1963, pp. 196-198.
10. Downs, B., "The Effect of Substantial Pretwist on the Stiffness Properties of Thin Beams of Cambered Section", Journal of Applied Mechanics, Vol. 46, June 1979, pp. 341-344.
11. Zienkiewicz, O.C., "The Finite Element Method", Third Edition, McGraw-Hill Book Company (UK) Limited, London, 1977, pp. 178-209.
12. Carnegie, W., "Static Bending of Pretwisted Cantilever Blading", Proc. Inst. Mech. Engrs., Vol. 171, No. 32, 1957.
13. MacBain, J.C., "Vibratory Behavior of Twisted Cantilevered Plates", Journal of Aircraft, Vol. 12, No. 4, April 1975.

14. Chen, Lee-Tzong, Dugundji, J., "Investigation of the Vibration Characteristics of Shrouded Bladed Disk Rotor Stages", Journal of Aircraft, Vol. 17, No. 7, July 1980.
15. Houbolt, J.C., Brooks, G.W., "Differential Equations of Motion for Combined Flapwise Bending, Chordwise Bending, and Torsion of Twisted Nonuniform Blades" NACA TN3905, 1958.
16. Sisto, F. and Chang, A.T., "The Influence of Gyroscopic Forces on the Dynamic Behavior and Flutter of Rotating Blades", Report No. ME-RT-82006, Stevens Institute of Technology, Hoboken, NJ, August 1982.
17. Smith, S.N., "Discrete Frequency Sound Generation in Axial Flow Turbomachines", British ARC, R & M 3709, London, 1973.
18. Dowell, E.H., et. al, A Modern Course in Aeroelasticity, Sijthoff & Noordhoff, The Netherlands, 1978, p. 109.

# APPENDIX A

ORIGINAL PAGE IS  
OF POOR QUALITY

$$\frac{du_s}{ds} = \frac{d\bar{u}}{ds} \cos \alpha s + \frac{d\bar{v}}{ds} \sin \alpha s$$

$$\frac{du_\eta}{ds} = -\frac{d\bar{u}}{ds} \sin \alpha s + \frac{d\bar{v}}{ds} \cos \alpha s$$

$$\text{at } s = -l/2$$

$$\omega = \omega_1$$

$$\frac{du_s}{ds} = \phi_{x1}$$

$$u_s = u_1$$

$$\frac{du_\eta}{ds} = -\phi_{y1}$$

$$u_\eta = v_1$$

$$\text{at } s = l/2$$

$$\omega = \omega_2$$

$$\frac{du_s}{ds} = \phi_{x2}$$

$$u_s = u_2$$

$$\frac{du_\eta}{ds} = -\phi_{y2}$$

$$u_\eta = v_2$$

This leads to

ORIGINAL PAGE IS  
OF POOR QUALITY

$$C_1 = -\frac{1}{l} w_1 + \frac{1}{l} w_2$$

$$C_2 = \frac{1}{2} w_1 + \frac{1}{2} w_2$$

$$C_{11} = -\frac{1}{l} \phi_1 + \frac{1}{l} \phi_2$$

$$C_{12} = \frac{1}{2} \phi_1 + \frac{1}{2} \phi_2$$

$$C_3 = \frac{l \cos \frac{\alpha l}{2}}{8} (\phi_{x1} - \phi_{x2})$$

$$- \frac{l \sin \frac{\alpha l}{2}}{8} (\phi_{y1} + \phi_{y2})$$

$$+ \frac{\cos \frac{\alpha l}{2}}{2} (u_1 + u_2) + \frac{\sin \frac{\alpha l}{2}}{2} (v_1 - v_2)$$

$$C_4 = 3 \frac{\cos \frac{\alpha l}{2}}{2l} (-u_1 + u_2) \quad \frac{3 \sin \frac{\alpha l}{2}}{2l} (v_1 + v_2)$$

$$- \frac{\cos \frac{\alpha l}{2}}{4} (\phi_{x1} + \phi_{x2})$$

$$+ \frac{\sin \frac{\alpha l}{2}}{4} (\phi_{y1} - \phi_{y2})$$

$$C_5 = -\frac{\cos \frac{\alpha l}{2}}{2l} (\phi_{x1} - \phi_{x2})$$

$$+ \frac{\sin \frac{\alpha l}{2}}{2l} (\phi_{y1} + \phi_{y2})$$

ORIGINAL PAGE IS  
OF POOR QUALITY

$$C_6 = \frac{\cos \frac{\alpha l}{2}}{l^2} (\phi_{x1} + \phi_{x2})$$

$$- \frac{\sin \frac{\alpha l}{2}}{l^2} (\phi_{y1} - \phi_{y2})$$

$$+ \frac{2 \cos \frac{\alpha l}{2}}{l^3} (u_1 - u_2) + \frac{2 \sin \frac{\alpha l}{2}}{l^3} (v_1 + v_2)$$

$$C_7 = -\frac{\sin \frac{\alpha l}{2}}{2} (u_1 - u_2) + \frac{\cos \frac{\alpha l}{2}}{2} (v_1 + v_2)$$

$$- \frac{l \sin \frac{\alpha l}{2}}{8} (\phi_{x1} + \phi_{x2})$$

$$- \frac{l \cos \frac{\alpha l}{2}}{8} (\phi_{y1} - \phi_{y2})$$

$$C_8 = \frac{3 \sin \frac{\alpha l}{2}}{2l} (u_1 + u_2) + \frac{3 \cos \frac{\alpha l}{2}}{2l} (-v_1 + v_2)$$

$$+ \frac{\sin \frac{\alpha l}{2}}{4} (\phi_{x1} - \phi_{x2})$$

$$+ \frac{\sin \frac{\alpha l}{2}}{4} (\phi_{y1} + \phi_{y2})$$

$$C_9 = \frac{\sin \frac{\alpha l}{2}}{2l} (\phi_{x1} + \phi_{x2})$$

$$+ \frac{\cos \frac{\alpha l}{2}}{2l} (\phi_{y1} - \phi_{y2})$$

ORIGINAL PAGE IS  
OF POOR QUALITY

$$C_{10} = -\frac{2 \sin \frac{\alpha l}{2}}{l^3} (u_1 + u_2) + \frac{2 \cos \frac{\alpha l}{2}}{l^3} (v_1 - v_2)$$

$$- \frac{\sin \frac{\alpha l}{2}}{l^2} (\phi_{x1} - \phi_{x2})$$

$$- \frac{\cos \frac{\alpha l}{2}}{l^2} (\phi_{y1} + \phi_{y2})$$



# APPENDIX B

ORIGINAL PAGE IS  
OF POOR QUALITY

These are non-zero elements of the transformation matrix  $[T_i]$

$$T_{1,1} = -1/l$$

$$T_{2,2} = \left[ 2 \left( \frac{-\cos \frac{\alpha l}{2}}{2l} \right) + 6 \left( \frac{\cos \frac{\alpha l}{2}}{l^2} \right) s \right] \cos(\alpha s) \\ + \left[ 2 \left( \frac{\sin \frac{\alpha l}{2}}{2l} \right) + 6 \left( \frac{-\sin \frac{\alpha l}{2}}{l^2} \right) s \right] \sin(\alpha s)$$

$$T_{2,3} = \left[ 6 \left( \frac{2\cos \frac{\alpha l}{2}}{l^3} \right) s \right] \cos(\alpha s) \\ + \left[ 6 \left( \frac{-2\sin \frac{\alpha l}{2}}{l^3} \right) s \right] \sin(\alpha s)$$

$$T_{2,4} = \left[ 2 \left( \frac{\sin \frac{\alpha l}{2}}{2l} \right) + 6 \left( \frac{-\sin \frac{\alpha l}{2}}{l^2} \right) s \right] \cos(\alpha s) \\ + \left[ 2 \left( \frac{\cos \frac{\alpha l}{2}}{2l} \right) + 6 \left( \frac{-\cos \frac{\alpha l}{2}}{l^2} \right) s \right] \sin(\alpha s)$$

$$T_{2,5} = \left[ 6 \left( \frac{2\sin \frac{\alpha l}{2}}{l^3} \right) s \right] \cos(\alpha s) \\ + \left[ 6 \left( \frac{2\cos \frac{\alpha l}{2}}{l^3} \right) s \right] \sin(\alpha s)$$

$$T_{2,8} = \left[ 2 \left( \frac{-\cos \frac{\alpha l}{2}}{2l} \right) + 6 \left( \frac{\cos \frac{\alpha l}{2}}{l^2} \right) s \right] \cos(\alpha s)$$

$$+ \left[ 2 \left( \frac{\sin \frac{\alpha l}{2}}{2l} \right) + 6 \left( \frac{-\sin \frac{\alpha l}{2}}{l^2} \right) s \right] \sin(\alpha s)$$

$$T_{2,9} = \left[ -6 \left( \frac{2 \cos \frac{\alpha l}{2}}{l^3} \right) s \right] \cos(\alpha s)$$

$$+ \left[ 6 \left( \frac{-2 \sin \frac{\alpha l}{2}}{l^3} \right) s \right] \sin(\alpha s)$$

ORIGINAL PAGE IS  
OF POOR QUALITY

$$T_{2,10} = \left[ 2 \left( \frac{\sin \frac{\alpha l}{2}}{2l} \right) + 6 \left( \frac{-\sin \frac{\alpha l}{2}}{l^2} \right) s \right] \cos(\alpha s)$$

$$+ \left[ 2 \left( \frac{\cos \frac{\alpha l}{2}}{2l} \right) + 6 \left( \frac{-\cos \frac{\alpha l}{2}}{l^2} \right) s \right] \sin(\alpha s)$$

$$T_{2,11} = \left[ 6 \left( \frac{2 \sin \frac{\alpha l}{2}}{l^3} \right) s \right] \cos(\alpha s)$$

$$+ \left[ -6 \left( \frac{2 \cos \frac{\alpha l}{2}}{l^3} \right) s \right] \sin(\alpha s)$$

$$T_{4,6} = -1/l$$

$$T_{1,7} = 1/l$$

$$T_{3,2} = - \left[ 2 \left( \frac{-\cos \frac{\alpha l}{2}}{2l} \right) + 6 \left( \frac{\cos \frac{\alpha l}{2}}{l^2} \right) s \right] \sin(\alpha s)$$

$$+ \left[ 2 \left( \frac{\sin \frac{\alpha l}{2}}{2l} \right) + 6 \left( \frac{-\sin \frac{\alpha l}{2}}{l^2} \right) s \right] \cos(\alpha s)$$

$$T_{3,3} = - \left[ 6 \left( \frac{2 \cos \frac{\alpha l}{2}}{l^3} \right) s \right] \sin(\alpha s) \\ + \left[ 6 \left( \frac{-2 \sin \frac{\alpha l}{2}}{l^3} \right) s \right] \cos(\alpha s)$$

$$T_{3,4} = - \left[ 2 \left( \frac{\sin \frac{\alpha l}{2}}{2l} \right) + 6 \left( \frac{-\sin \frac{\alpha l}{2}}{l^2} \right) s \right] \sin(\alpha s) \\ + \left[ 2 \left( \frac{\cos \frac{\alpha l}{2}}{2l} \right) + 6 \left( \frac{-\cos \frac{\alpha l}{2}}{l^2} \right) s \right] \cos(\alpha s)$$

$$T_{3,5} = - \left[ 6 \left( \frac{2 \sin \frac{\alpha l}{2}}{l^3} \right) s \right] \sin(\alpha s) \\ + \left[ 6 \left( \frac{2 \cos \frac{\alpha l}{2}}{l^3} \right) s \right] \cos(\alpha s)$$

$$T_{3,8} = - \left[ 2 \left( \frac{-\cos \frac{\alpha l}{2}}{2l} \right) + 6 \left( \frac{\cos \frac{\alpha l}{2}}{l^2} \right) s \right] \sin(\alpha s) \\ + \left[ 2 \left( \frac{\sin \frac{\alpha l}{2}}{2l} \right) + 6 \left( \frac{-\sin \frac{\alpha l}{2}}{l^2} \right) s \right] \cos(\alpha s)$$

$$T_{3,9} = - \left[ -6 \left( \frac{2 \cos \frac{\alpha l}{2}}{l^3} \right) s \right] \sin(\alpha s) \\ + \left[ 6 \left( \frac{-2 \sin \frac{\alpha l}{2}}{l^3} \right) s \right] \cos(\alpha s)$$

$$T_{3,10} = - \left[ 2 \left( \frac{\sin \frac{\alpha l}{2}}{2l} \right) + 6 \left( \frac{-\sin \frac{\alpha l}{2}}{l^2} \right) s \right] \sin(\alpha s) \\ + \left[ 2 \left( \frac{\cos \frac{\alpha l}{2}}{2l} \right) + 6 \left( \frac{-\cos \frac{\alpha l}{2}}{l^2} \right) s \right] \cos(\alpha s)$$

$$T_{3,11} = - \left[ 6 \left( \frac{2 \sin \frac{\alpha l}{2}}{l^3} \right) s \right] \sin(\alpha s) \\ + \left[ -6 \left( \frac{2 \sin \frac{\alpha l}{2}}{l^3} \right) s \right] \cos(\alpha s)$$

$$T_{4,12} = 1/l$$

# APPENDIX C

Subroutine STIFF(A)  
Gauss - Legendre Integration  
A - Pretwist angle per unit length  
for one element



## Initial Data

Modulus of Elasticity - AMAT(1)  
Poissons Ratio - AMAT(2)  
Length, width & Thickness of the  $i$ th element - AL, W, T  
Coordinates of the nodes on the circumference of the cross section (origin at shear center)  
in x direction - SIP(i)  $i = 1, 2, \dots, 8$   
in y direction - ETAP(i)

Define :

Five point formula for Gauss - Legendre Integration

Roots  
 $x(1) = -.9061798459$   
 $x(2) = -.5384693101$   
 $x(3) = 0.$   
 $x(4) = -x(2)$   
 $x(5) = -x(1)$

weight factors  
 $WF(1) = .2369268850$   
 $WF(2) = .4786286704$   
 $WF(3) = .5688888889$   
 $WF(4) = WF(2)$   
 $WF(5) = WF(1)$



(A)

Initial variables  
 $FK(I,J) = 0, I = 1, \dots, 12$   
 $SM(I,J) = 0, J = 1, \dots, 12$

DO K1 = 1, 2

Integration in z direction  
two points formula

(C) Do Loop

$z = (-1)^K \cdot AL \cdot .57735027/\Delta$

DO K2 = 1, 5

Integration in x direction  
five points formula

(D) Do Loop

DO K3 = 1, 5

Integration in y direction  
five points formula

(E) Do Loop

Call Subroutine SHAP(X(K2), X(K3))  
 - Evaluation of the shape function  $N_i$   
 and its derivatives  $\frac{\partial N_i}{\partial \xi} + \frac{\partial N_i}{\partial \eta}$

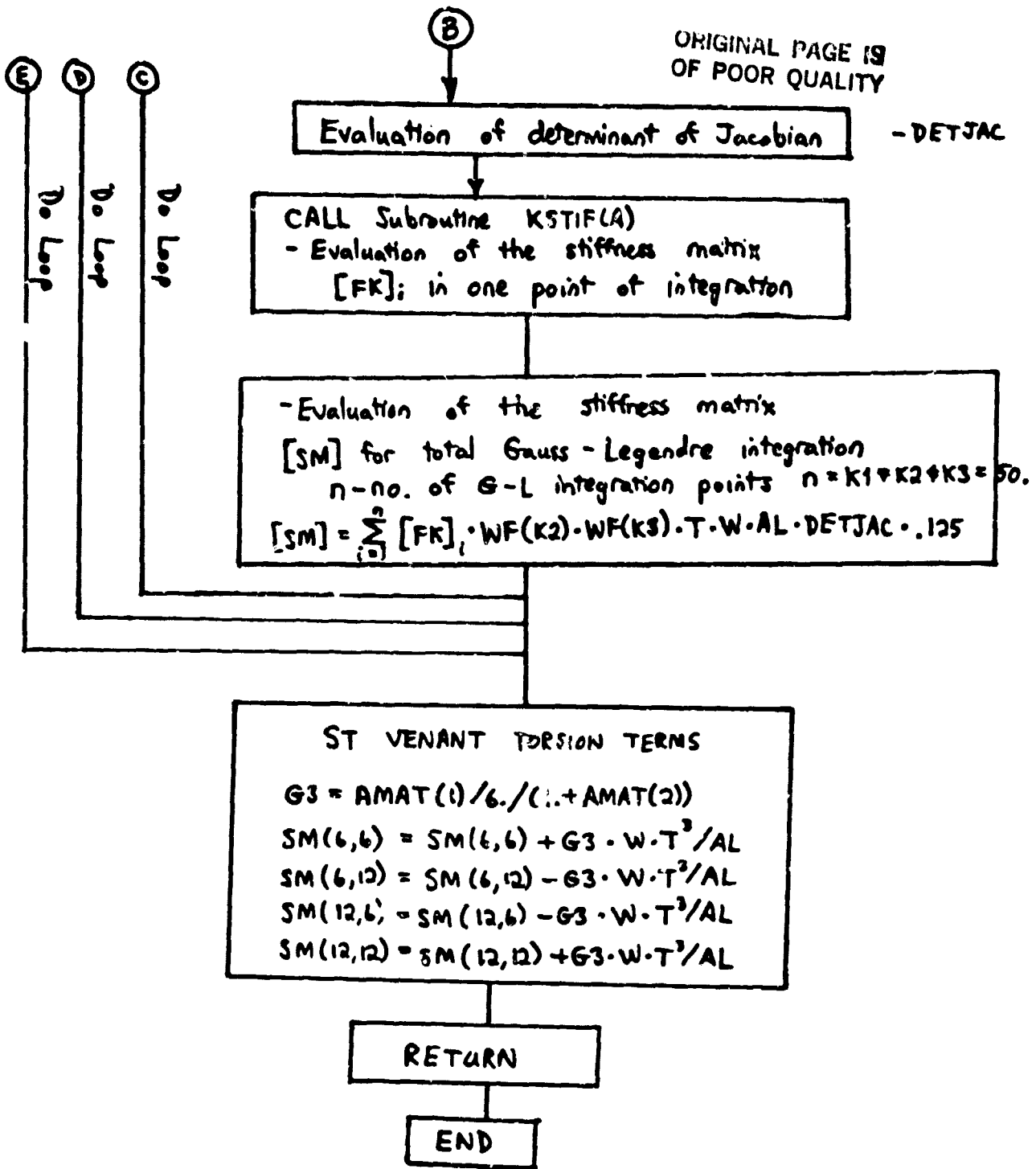
$N_j = \text{SHAPE}(J)$   
 $\frac{\partial N_i}{\partial \xi} + \frac{\partial N_i}{\partial \eta}$  are  
 $\text{DSHAPE}(I, J)$   
 $\xi - \text{SI} \quad \eta - \text{ET}$

$$\begin{Bmatrix} \xi \\ \eta \end{Bmatrix} = \begin{bmatrix} N_1 & 0 & N_2 & 0 & \dots & N_8 & 0 \\ 0 & N_1 & 0 & N_2 & \dots & 0 & N_8 \end{bmatrix} \begin{Bmatrix} \text{SIP}(1) \\ \text{ETAP}(1) \\ \vdots \\ \text{SIP}(8) \\ \text{ETAP}(8) \end{Bmatrix}$$

$$2 [\text{FJACOB}] = \begin{bmatrix} \frac{\partial N_1}{\partial \xi} & \frac{\partial N_2}{\partial \xi} & \dots & \frac{\partial N_8}{\partial \xi} \\ \frac{\partial N_1}{\partial \eta} & \frac{\partial N_2}{\partial \eta} & \dots & \frac{\partial N_8}{\partial \eta} \end{bmatrix} \begin{Bmatrix} \text{SIP}(1) \text{ ETAP}(1) \\ \vdots \\ \text{SIP}(8) \text{ ETAP}(8) \end{Bmatrix}$$

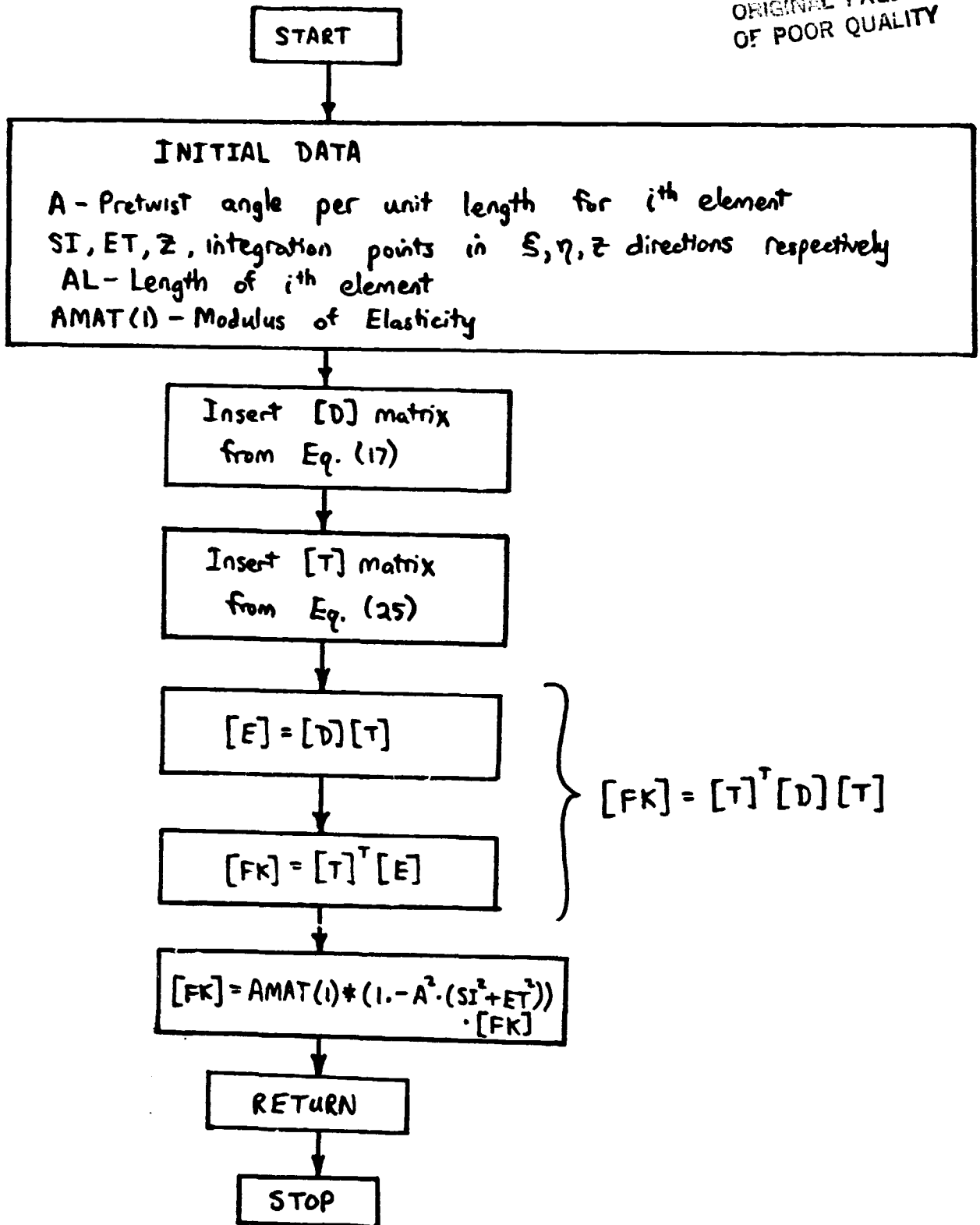
[Jacobian] =  
[FJACOB]

(B)



Subroutine KSTIF(A)  
 Evaluation of the stiffness matrix [FK]  
 for every point of G-L integration

ORIGINAL PAGE IS  
 OF POOR QUALITY





# Subroutine SHAP(X,Y)

Evaluation of the shape function  $N_i$   
and its derivatives  $\frac{\partial N_i}{\partial \xi} + \frac{\partial N_i}{\partial \eta}$

ORIGINAL PAGE IS  
OF POOR QUALITY

START

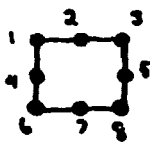
INITIAL DATA  
 $x + y$  are roots from  
Gauss-Legendre Integration, in  
 $\xi + \eta$  directions respectively

$$N_i = \text{SHAPE}(I)$$

$$\frac{\partial N_i}{\partial \xi} = \text{DSHAPE}(1, I)$$

$$\frac{\partial N_i}{\partial \eta} = \text{DSHAPE}(2, I)$$

Insert  $8(\xi + \eta)$  points of  
quadratic element  
in matrix form [RL]  
 $((RL(I, J), T=1, 8), I=1, 2)$   
/-1, 0, 1, -1, 1, -1, 0, 1, 1, 1, 1, 0, 0, -1, -1, -1/



DO I=1, 8

SX = R(1, I) \* X  
SY = R(2, I) \* Y

I=2  
OR I=7

I=4  
OR I=5

Do Loop

Evaluate shape function  $N_i$  + its derivatives  
for middle points in  
y direction

Evaluate shape function  $N_i$  + its derivatives  
for middle  
points in x direction

Evaluate shape function  $N_i$  + its derivatives  
for corner  
points

RETURN

END

## APPENDIX D

$$F1 = \frac{L}{8} + s \left[ -0.25 + s \left( -\frac{0.5}{L} + \frac{s}{L^2} \right) \right]$$

$$F2 = 0.5 + s \left[ -3 * \frac{0.5}{L} + \frac{2}{L} \left( \frac{s}{L} \right)^2 \right]$$

$$F3 = \frac{L}{8} + s \left[ 0.25 + s \left( -\frac{0.5}{L} - \frac{s}{L^2} \right) \right]$$

$$F4 = 0.5 + s \left[ 3 * \frac{0.5}{L} - \frac{2}{L} \left( \frac{s}{L} \right)^2 \right]$$

$$F5 = 0.25 + \frac{s}{L} \left( 1 - 3 \left( \frac{s}{L} \right) \right)$$

$$F6 = 3 \left[ \frac{0.5}{L} - \frac{2}{L} \left( \frac{s}{L} \right)^2 \right]$$

$$F7 = 0.25 - \frac{s}{L} \left( 1 + 3 \left( \frac{s}{L} \right) \right)$$

where  $\alpha$  is the pretwist angle per unit length for  $i$ th element

$L$  is the length of the  $i$ th element

$s$  is the coordinate along the  $i$ th element, its origin is at the middle of the element

0	$\frac{\omega L}{2} \cdot F1$	$\cos \frac{\omega L}{2} \cdot F2$	$-\sin \frac{\omega L}{2} \cdot F1$	$\sin \frac{\omega L}{2} \cdot F2$	0	0	$-\cos \frac{\omega L}{2} \cdot F3$	$\cos \frac{\omega L}{2} \cdot F4$	$-\sin \frac{\omega L}{2} \cdot F3$	$-\sin \frac{\omega L}{2} \cdot F4$	0
0	$-\sin \frac{\omega L}{2} \cdot F1$	$-\sin \frac{\omega L}{2} \cdot F2$	$-\cos \frac{\omega L}{2} \cdot F1$	$\cos \frac{\omega L}{2} \cdot F2$	0	0	$-\sin \frac{\omega L}{2} \cdot F3$	$\sin \frac{\omega L}{2} \cdot F4$	$+\cos \frac{\omega L}{2} \cdot F3$	$+\cos \frac{\omega L}{2} \cdot F4$	0
$-\frac{1}{2} \frac{\omega L}{2} + \frac{1}{2}$	0	0	0	0	0	$\frac{1}{2} \frac{\omega L}{2} + \frac{1}{2}$	0	0	0	0	0
0	0	0	0	0	$-\frac{1}{2} \frac{\omega L}{2} + \frac{1}{2}$	0	0	0	0	0	$\frac{1}{2} \frac{\omega L}{2} + \frac{1}{2}$
0	$-\cos \frac{\omega L}{2} \cdot F5$	$-\cos \frac{\omega L}{2} \cdot F6$	$\sin \frac{\omega L}{2} \cdot F5$	$-\sin \frac{\omega L}{2} \cdot F6$	0	0	$-\cos \frac{\omega L}{2} \cdot F7$	$\cos \frac{\omega L}{2} \cdot F6$	$-\sin \frac{\omega L}{2} \cdot F7$	$-\sin \frac{\omega L}{2} \cdot F6$	0
0	$\sin \frac{\omega L}{2} \cdot F5$	$\sin \frac{\omega L}{2} \cdot F6$	$\cos \frac{\omega L}{2} \cdot F5$	$-\cos \frac{\omega L}{2} \cdot F6$	0	0	$-\sin \frac{\omega L}{2} \cdot F7$	$\sin \frac{\omega L}{2} \cdot F6$	$\cos \frac{\omega L}{2} \cdot F7$	$\cos \frac{\omega L}{2} \cdot F6$	0
0	0	0	0	0	$-\frac{1}{2}$	0	0	0	0	0	$\frac{1}{2}$

# APPENDIX E

ORIGINAL PAGE IS  
OF POOR QUALITY

$$[A_i] = \begin{bmatrix} 1 & 0 & 0 & -y & 0 & 0 & 0 \\ 0 & 1 & 0 & x & 0 & 0 & 0 \\ 0 & 0 & 1 & 0 & 0 & 0 & 0 \\ -y & x & 0 & x^2+y^2 \\ & & & +d^2(x^2+y^2)^2 & 0 & 0 & 0 \\ 0 & 0 & 0 & 0 & 0 & 0 & 0 \\ 0 & 0 & 0 & 0 & 0 & 0 & 0 \\ 0 & 0 & 0 & 0 & 0 & 0 & 0 \end{bmatrix}$$

where  $x, y$  are the axes of the  
cross-sectional area

ORIGINAL PAGE IS  
OF POOR QUALITY

$R^2$	$-wR \cos \theta$	$-wR \sin \theta$	$-2xwR \cos \theta - ywR^2$ $+ ywR^2 \sin^2 \theta + yw\omega^2$ $-\frac{1}{2}R^2 \sin 2\theta (z+\rho)$ $-wR \sin \theta \alpha (x^2+y^2)$	0	0	0	
$-wR \cos \theta$	$R^2 \sin^2 \theta + w^2$	$-\frac{1}{2}R^2 \sin 2\theta$	$R^2 \sin^2 \theta + xw\omega^2$ $+ 2ywR \cos \theta - xR^2$ $-\frac{1}{2}R^2 \sin 2\theta \alpha (x^2+y^2)$ $+ wR \sin \theta (z+\rho)$	0	0	0	
$-wR \sin \theta$	$-\frac{1}{2}R^2 \sin 2\theta$	$R^2 \cos^2 \theta + w^2$	$wR \sin \theta y - \frac{1}{2}R^2 x \sin 2\theta$ $+ R^2 \cos^2 \theta \alpha (x^2+y^2)$ $+ w^2 \alpha (x^2+y^2)$	0	0	0	
$-2xwR \cos \theta - ywR^2$ $+ ywR^2 \sin^2 \theta + yw\omega^2$ $-\frac{1}{2}R^2 \sin 2\theta (z+\rho)$ $-wR \sin \theta \alpha (x^2+y^2)$	$R^2 \sin^2 \theta + xw\omega^2$ $+ 2ywR \cos \theta - xR^2$ $-\frac{1}{2}R^2 \sin 2\theta \alpha (x^2+y^2)$ $+ wR \sin \theta (z+\rho)$	$-\frac{1}{2}R^2 \sin 2\theta$	$wR \sin \theta y - \frac{1}{2}R^2 x \sin 2\theta$ $+ R^2 \cos^2 \theta \alpha (x^2+y^2)$ $+ w^2 \alpha (x^2+y^2)$	$R^2 x \sin^2 \theta + ywR^2 + x^2 w^2$ $+ 2xywR \cos \theta$ $+ R^2 \cos^2 \theta \alpha (x^2+y^2)^2$ $- R^2 \sin 2\theta \alpha \alpha (x^2+y^2)$ $+ \alpha (x^2+y^2)^2 w^2$ $+ 2wR \sin \theta y \alpha (x^2+y^2)$	0	0	0
$-wR \cos \theta$	$R^2 \sin^2 \theta + w^2$	$-\frac{1}{2}R^2 \sin 2\theta$	$R^2 \cos^2 \theta + w^2$	$-\frac{1}{2}R^2 \cos^2 \theta ((L+R)^2$ $-(z^2+\rho^2)) + R^2 \sin 2\theta$ $\cdot \frac{1}{2} y (L^2 - z^2) - \frac{1}{2} w^2$ $\cdot ((L^2 + R^2) - (z^2 + \rho^2))$ $+ wR \sin \theta (L^2 - z^2) x$	0	0	0
$-wR \sin \theta$	$-\frac{1}{2}R^2 \sin 2\theta$	$R^2 \cos^2 \theta + w^2$	$wR \sin \theta y - \frac{1}{2}R^2 x \sin 2\theta$ $+ R^2 \cos^2 \theta \alpha (x^2+y^2)$ $+ w^2 \alpha (x^2+y^2)$	$-\frac{1}{2}R^2 \cos^2 \theta ((L+R)^2$ $-(z^2+\rho^2)) + R^2 \sin 2\theta$ $\cdot \frac{1}{2} y (L^2 - z^2) - \frac{1}{2} w^2$ $\cdot ((L^2 + R^2) - (z^2 + \rho^2))$ $+ wR \sin \theta (L^2 - z^2) x$	0	0	0
$-2xwR \cos \theta - ywR^2$ $+ ywR^2 \sin^2 \theta + yw\omega^2$ $-\frac{1}{2}R^2 \sin 2\theta (z+\rho)$ $-wR \sin \theta \alpha (x^2+y^2)$	$R^2 \sin^2 \theta + xw\omega^2$ $+ 2ywR \cos \theta - xR^2$ $-\frac{1}{2}R^2 \sin 2\theta \alpha (x^2+y^2)$ $+ wR \sin \theta (z+\rho)$	$-\frac{1}{2}R^2 \sin 2\theta$	$wR \sin \theta y - \frac{1}{2}R^2 x \sin 2\theta$ $+ R^2 \cos^2 \theta \alpha (x^2+y^2)$ $+ w^2 \alpha (x^2+y^2)$	$-\frac{1}{2}R^2 \cos^2 \theta ((L+R)^2$ $-(z^2+\rho^2)) + R^2 \sin 2\theta$ $\cdot \frac{1}{2} y (L^2 - z^2) - \frac{1}{2} w^2$ $\cdot ((L^2 + R^2) - (z^2 + \rho^2))$ $+ wR \sin \theta (L^2 - z^2) x$	0	0	0
$-wR \cos \theta$	$R^2 \sin^2 \theta + w^2$	$-\frac{1}{2}R^2 \sin 2\theta$	$R^2 \cos^2 \theta + w^2$	$-\frac{1}{2}R^2 \cos^2 \theta ((L+R)^2$ $-(z^2+\rho^2)) + R^2 \sin 2\theta$ $\cdot \frac{1}{2} y (L^2 - z^2) - \frac{1}{2} w^2$ $\cdot ((L^2 + R^2) - (z^2 + \rho^2))$ $+ wR \sin \theta (L^2 - z^2) x$	0	0	0
$-wR \sin \theta$	$-\frac{1}{2}R^2 \sin 2\theta$	$R^2 \cos^2 \theta + w^2$	$wR \sin \theta y - \frac{1}{2}R^2 x \sin 2\theta$ $+ R^2 \cos^2 \theta \alpha (x^2+y^2)$ $+ w^2 \alpha (x^2+y^2)$	$-\frac{1}{2}R^2 \cos^2 \theta ((L+R)^2$ $-(z^2+\rho^2)) + R^2 \sin 2\theta$ $\cdot \frac{1}{2} y (L^2 - z^2) - \frac{1}{2} w^2$ $\cdot ((L^2 + R^2) - (z^2 + \rho^2))$ $+ wR \sin \theta (L^2 - z^2) x$	0	0	0

$-R^2 \cos^2 \theta (x^2+y^2)$   
 $-\frac{1}{2} [(L+R)^2 - (z^2+\rho^2)]$   
 $+ R^2 \sin 2\theta (x^2+y^2) y$   
 $\cdot \frac{1}{2} [L-z]$   
 $-wR \alpha (x^2+y^2)$   
 $-\frac{1}{2} [(L+R)^2 - (z^2+\rho^2)]$   
 $+ wR \sin \theta \alpha (x^2+y^2)$   
 $\cdot (L-z)$

ORIGINAL PAGE IS  
OF POOR QUALITY

0	$-2R \sin \theta$	$2R \cos \theta$	$2R \cos \theta (x^2 + y^2) \omega - (z+R) 2\bar{\omega}$	0	0	0
$2R \sin \theta$	0	$-2\bar{\omega}$	$-2\bar{\omega} \alpha (x^2 + y^2) - 2(z+R)R \cos \theta$	0	0	0
$-2R \cos \theta$	$2\bar{\omega}$	0	$2R \cos \theta y + 2\bar{\omega} x$	0	0	0
$4R \sin \theta x - 2R \cos \theta \cdot (x^2 + y^2) \omega - 2\bar{\omega}(z+R)$	$4R \sin \theta y + 2\bar{\omega}(x^2 + y^2) \alpha - 2R \cos \theta (z+R)$	$-2yR \cos \theta - 2\bar{\omega} x$	0	0	0	0
0	0	0	$-2y\omega (\bar{L}-z) + 2xR \cos \theta (\bar{L}-z)^*$	0	0	0
0	0	0	$(\bar{L}-z) (2xR \cos \theta - 2y\bar{\omega})$	0	0	0
0	0	0	$-2(x^2 + y^2)y\omega \cdot (\bar{L}-z)^* + 2xR \cos \theta (\bar{L}-z)$	0	0	0

$[A_3] =$

$$\{A_4\} = \begin{bmatrix} -2\Omega \sin\theta y + 2\Omega \cos\theta (z^* + R) \\ -2\omega(z^* + R) + 2x\Omega \sin\theta \\ 2y\omega - 2x\Omega \cos\theta \\ -2\Omega y(z^* + R) \cos\theta + 2\Omega y^2 \sin\theta \\ -2x\omega(z^* + R) + 2x^2\Omega \sin\theta \\ 0 \\ 0 \\ 0 \end{bmatrix}$$

ORIGINAL PAGE 19  
OF POOR QUALITY

$$\{A_5\} = \begin{bmatrix} 2x\Omega^2 - 2\omega\Omega(z^* + R) \sin\theta - 2y\omega\Omega \cos\theta \\ 2y\Omega^2 \sin^2\theta - \Omega^2 \sin 2\theta (z^* + R) + 2y\omega^2 - 2x\omega\Omega \cos\theta \\ 2\Omega^2 \cos^2\theta (R + z^*) - y\Omega^2 \sin 2\theta + 2\omega^2(z^* + R) \\ - 2x\omega\Omega \sin\theta \\ 2xy\Omega^2 \sin^2\theta - \Omega^2 \sin 2\theta (xz^* + xR) - 2xy\Omega^2 \\ + 2\omega\Omega y \sin\theta (z^* + R) + 2y\omega^2 x \\ - 2x^2\omega\Omega \cos\theta + 2y^2\omega\Omega \cos\theta \\ 0 \\ 0 \\ 0 \end{bmatrix}$$

where

$R$  = Hub radius       $L^*$  = blade length

$z^*$  = Length between the root of the blade to the middle of the  $i$ th element plus distance  $z$

$\theta = \omega t$

$\omega$  = Spin velocity

$\Omega$  = Precessional velocity